②

Annual Report

Interface Properties of Wide Bandgap Semiconductor Structures

Office of Naval Research
Supported under Grant #N00014-92-J-1477
Report for the period 2/19/92-12/31/92

Robert F. Davis, Salah Bedair*, Jerry Bernholc**,
Jeffrey T. Glass and R. J. Nemanich**
c/o Materials Science and Engineering Department
*Electrical and Computer Engineering Department
and **Department of Physics
North Carolina State University
Campus Box 7907
Raleigh, NC 27695-7907

December, 1992

103 pp

REPORT DOCUMENTATION PAGE

Form Approved
OMB No 0704-0188

1. AGENCY USE ONLY *(Leave blank)*

2. REPORT DATE
December 1992

3. REPORT TYPE AND DATES COVERED
Annual 2/19/92–12/31/92

4. TITLE AND SUBTITLE
Interface Properties of Wide Bandgap Semiconductor Structures

5. FUNDING NUMBERS
uri41114a-01
1114SS
N00179
N66005
4B855

6. AUTHOR(S)
Robert F. Davis

7. PERFORMING ORGANIZATION NAME(S) AND ADDRESS(ES)
North Carolina State University
Hillsborough Street
Raleigh,NC 27695

8. PERFORMING ORGANIZATION REPORT NUMBER
N00014-92-J-1477

9. SPONSORING/MONITORING AGENCY NAME(S) AND ADDRESS(ES)
Sponsoring: ONR, 800 N. Quincy, Arlington, VA 22217
Monitoring: Office of Naval Research Resider
The Ohio State University Research Center
1960 Kenny Road
Columbus, OH 43210-1063

10. SPONSORING/MONITORING AGENCY REPORT NUMBER

11. SUPPLEMENTARY NOTES

12a. DISTRIBUTION/AVAILABILITY STATEMENT
Approved for Public Release; Distribution Unlimited

12b. DISTRIBUTION CODE

13. ABSTRACT *(Maximum 200 words)*

Theoretical computations using the Car-Parrinello version of quantum molecular dynamics is being used to study the structure, bonding, and reactions of various C-, Cl- and H-containing species on the diamond surface, particularly as they pertain to the ALE of diamond. Related studies are also focused on the potential for particular elements to be donor and acceptor species in GaN and AlN. The interfacial aspects of diamond growth and the negative electron affinity on the (111) surface have been extensively investigated. Computer-controlled synthesis of diamond has been achieved using an oxy-C_2H_2 torch. Two-dimensional growth was achieved. Epitaxial films of cubic β(3C)-SiC(111) and AlN(0001) have been deposited on α(6H)-SiC(0001) substrates oriented 3-4° towards $[11\bar{2}0]$ at 1050°C via gas-source MBE using Si_2H_6, C_2H_4, thermal evaporation of Al and activated N species from an ECR plasma. HRTEM revealed that the nucleation and growth of the β(3C)-SiC regions occurred primarily on terraces between closely spaced steps. Pseudomorphic bilayer structures containing β(3C)-SiC and 2H-AlN have been grown under the same conditions for the first time. Epitaxial GaP and GaN films have also been achieved via GSMBE at 200°C and ALE at 635°C, respectively. Rectifying contacts of (1) SiGe alloys and (2) Ti, Pt, and Hf have been deposited and characterized on diamond(100) and α(6H)-SiC(0001), respectively.

14. SUBJECT TERMS
molecular dynamics, thin films, diamond surface, atomic layer epitaxy, AlN, GaN, SiC, oxy-acetylene torch, MBE, pseudomorphic heterostructures, Schottky contacts, SiGe alloys.

15. NUMBER OF PAGES
120

16. PRICE CODE

17. SECURITY CLASSIFICATION OF REPORT	18. SECURITY CLASSIFICATION OF THIS PAGE	19. SECURITY CLASSIFICATION OF ABSTRACT	20. LIMITATION OF ABSTRACT
UNCLAS	UNCLAS	UNCLAS	SAR

NSN 7540-01-280-5500

Standard Form 298 (Rev. 2-89)
Prescribed by ANSI Std. Z39-18
298-102

Table of Contents

I. Introduction 1

Theoretical Studies

II. Theoretical Studies of Wide Band-Gap Materials 4

Thin Film Growth and Characterization of Carbon-based Materials

III. Properties of Interfaces of Diamond 17
IV. Diamond Synthesis Using the Oxy-acetylene Torch Method 40
V. Gas-Source Molecular Beam Epitaxy of Monocrystalline Beta-SiC on Vicinal Alpha(6H)-SiC 47

Thin Film Growth and Characterization of Solid Solutions and Multi-layer Heterostructures from Silicon Carbide and III-V Nitrides

VI. Solid Solutions of AlN and SiC Grown by Plasma-Assisted, Gas-Source Molecular Beam Epitaxy 58
VII. Aluminum Nitride/Silicon Carbide Multilayer Heterostructure Produced by Plasma-Assisted Gas-Source Molecular Beam Epitaxy 64

Thin Film Growth and Characterization of III-V Materials

VIII. Epitaxial Growth of AlN by Plasma-Assisted Gas-Source Molecular Beam Epitaxy 75
IX. Low Temperature Growth of GaP by Gas-source Molecular Beam Epitaxy 86
X. Deposition of GaN by Atomic Layer Epitaxy—Davis Group 93
XI. Atomic Layer Epitaxy of GaN—Bedair Group 101
XII. Growth and Characterization of SiGe Contacts on Semiconducting Diamond Substrates 103

Metal Contacts

XIII. Chemical and Electrical Mechanisms in Titanium, Platinum, and Hafnium Contacts to Alpha (6H) Silicon Carbide 108

Atomic Layer Etching

XIV. Atomic Layer Etching 118

XV. Distribution List 120

I. Introduction

Heteroepitaxy is the growth of a crystal (or a film) on a foreign crystalline substrate that determines its orientation. Such oriented growth requires that lattice planes in both materials have similar structure. In general, an epitaxial relationship is probable whenever the orientation of the substrate and overgrowth produces an interface with a highly coincident atomic structure having low interfacial energy relative to a random arrangement.

During the past decade, nonequilibrium techniques have been developed for the growth of epitaxial semiconductors, superconductors, insulators and metals which have led to new classes of artificially structured materials. In many cases, the films were deposited on substrates having a different chemistry from that of the film, and heteroepitaxy was achieved. Moreover, layered structures with a periodicity of a few atomic layers have also been produced by the sequential heteroepitaxial deposition of a film of one type on another. Metastable structures can be generated which possess important properties not present in equilibrium systems. A consideration of the materials under consideration for next generation electronic and optoelectronic devices, e.g., the III-V nitrides show that only a few of them can currently be grown in bulk, single crystal form having a cross-sectional area of $>3\text{cm}^2$. Thus other, commercially available substrates must be used. This introduces a new set of challenges for the successful growth of device quality films which are not present in homoepitaxial growth and which must be surmounted if these materials are to be utilized in device structures.

In addition to providing structures which do not exist in nature, applications of advanced heteroepitaxial techniques permit the growth of extremely high quality heterostructures involving semiconductors, metals, and insulators. These heterostructures offer the opportunity to study relationships between the atomic structure and the electrical properties of both the film itself and the interface between the two dissimilar materials. They also allow the study of epitaxial growth between materials exhibiting very different types (ionic, covalent, or metallic) of bonding.

While the potential of heteroepitaxial deposition has been demonstrated, significant advances in theoretical understanding, experimental growth and control of this growth, and characterization are required to exploit the capabilities of this process route. It is particularly important to understand and control the principal processes which control heteroepitaxy at the atomic level. It is this type of research as well as the chemistry of dry etching via laser and plasma processing which forms the basis of the research in this grant.

The materials of concern in this grant are classified as wide bandgap semiconductors and include diamond, the III-V nitrides, SiC, GaP and AlP. The extremes in electronic and thermal properties of diamond and SiC allow the types and numbers of current and conceivable applications of these materials to be substantial. However a principal driving force for the interest in the III–V nitrides and GaP and AlP is their potential for solid-state optoelectronic devices for light emission and detection from the visible through the far ultraviolet range of the spectrum.

The principal objectives of the research program are the determination of (1) the fundamental physical and chemical processes ongoing at the substrate surface and substrate/film interface during the heteroepitaxial deposition of both monocrystalline films of the materials noted above as well as metal contacts on these materials, (2) the mode of nucleation and growth of the materials noted in (1) on selected substrates and on each other in the fabrication of multilayer heterostructures, (3) the resulting properties of the individual films and the layered structures and the effect of interfacial defects on these properties, (4) the development and use of theoretical concepts relevant to the research in objectives (1)-(3) to assist in the fabrication of improved films and structures and (5) the determination of process chemistry which leads to the laser assisted and plasma etching of these wide bandgap compound semiconductors.

The following sections introduce each topic, detail the experimental approaches, report the results to date and provide a discussion and conclusions for each subject. Each major section is self-contained with its own figures, tables and references.

THEORETICAL STUDIES

II. Theoretical Studies of Wide Band-Gap Materials

A. Introduction

Theoretical backgound for the experimental part of this Project includes the computation performed using the Car-Parrinello version of quantum molecular dynamics. The attention was focused on (i) the mechanisms of growth, particularly ALE growth; (ii) modeling of surface interactions during etching and cleaning processes. (iii) the effects of deviations of stoichiometry and thereby induced defects on the electronic properties.

The quantum molecular dynamics (Car-Parrinello) methodology is relatively new. We have recently made several technical improvements to this formalism which allow us to optimize routinely systems involving up to ~ 100 atoms [1], search for lowest energy configurations via a substantially improved simulated annealing algorithms, and investigate highly activated reactive processes via our adiabatic trajectory formalism [2].

One should also mention that the proposed methodology, although almost fully developed, is rather new and that a successful completion of the proposed work would pave the way for applications to other systems. It may thus have a broad impact on the field of theoretical materials science.

B. Brief Review of Local Density Theory and of Quantum Molecular Dynamics

The calculations have been carried out using local density theory and first principles angular-momentum-dependent pseudopotentials. Since this methodology is well known, only a short review is given here, highlighting the aspects important to the success of the proposed research.

In the local density method, the total energy of a system is a functional of the electron density, $E_{tot}=E_{tot}(\rho)$, where $\rho=\Sigma|\psi|^2$. In the usual approach, one solves an effective Schrödinger equation (in Rydbergs)

$$[-\nabla^2 + V_n(\mathbf{r}) + \int \frac{2\rho(\mathbf{r}')\,d\mathbf{r}}{|\mathbf{r}-\mathbf{r}'|} + \mu_{xc}(\mathbf{r})]\psi_i(\mathbf{r}) = \varepsilon_i\psi_i(\mathbf{r}), \quad i = 1,\ldots N \qquad (1)$$

for the N electrons in the system. The first term in (1) represents the kinetic energy, the second the electrostatic potential due to the nuclei, the third the classical electron-electron repulsion potential and the fourth is the so-called exchange and correlation potential, describing the average effects of exchange and correlation derived from the theory of electron gas.

The eigenvalues and wavefunctions are obtained by expanding the operators and wavefunctions in a set of basis functions (e.g. plane waves or gaussian orbitals, depending on the method) and subsequently diagonalizing the resulting secular equations.

Local density theory allows for the calculation of the total energy of the system. In the notation of eq. (1),

$$E_{tot} = \sum_{occ} \varepsilon_i - \frac{1}{2}\iint \frac{2\rho\rho' \, d\mathbf{r}d\mathbf{r}'}{|\mathbf{r} - \mathbf{r}'|} + \int(\varepsilon_{xc} - \mu_{xc})\rho(\mathbf{r}) \, d\mathbf{r} + \frac{1}{2}\sum_{i\neq j} \frac{2Z_iZ_j}{|\mathbf{R}_i - \mathbf{R}_j|} \qquad (2)$$

where the sum over the occupied eigenvalues is corrected by the double-counting term and by the contributions of the exchange and correlation interactions. The $\varepsilon_{xc}(\mathbf{r})$ is the exchange-correlation energy density within the local density approximation. The last term represents the classical electrostatic repulsion energy between nuclei of charges Z_i and Z_j at positions R_i and R_j.

The computational effort can be substantially reduced if the calculations are restricted to explicitly consider only the valence electrons. This is possible if the nuclear potentials entering eq. (1) are replaced by pseudopotentials which describe the core-valence interactions. Such pseudopotentials can be derived from first-principles all-electron calculations for the individual atoms. The atomic all-electron valence eigenvalues are reproduced exactly by the pseudopotential calculations.

For very large systems, it is advantageous to solve the local density equations (1) iteratively [3], rather than by setting up a large secular equation to be diagonalized by standard packages. Furthermore, in a search for an equilibrium geometry, it may be more efficient to minimize the total energy expression (2) simultaneously with respect to the electronic degrees of freedom as well as atomic coordinates [4] in particular if many iterations are needed to converge the electronic wavefunctions.

A particularly powerful approach for solving the Kohn-Sham equations has been formulated by Car and Parrinello [5] by combining local density theory with molecular dynamics. In their method one considers the wavefunctions, the atomic positions and any constraints to be time-dependent, which allows for accurate first-principles calculations of time-dependent properties of large supercells. The problem of minimization of the total energy (2) is cast in a molecular dynamics formalism by introducing the Lagrangian

$$L = \sum_i \frac{1}{2}\mu \int_\Omega d^3r \, |\dot{\psi}_i|^2 + \sum_I \frac{1}{2} M_I \dot{\mathbf{R}}_I^2 + \sum_v \frac{1}{2}\mu_v \dot{\alpha}_v^2 - E[\{\psi_i\},\{\mathbf{R}_I\},\{\alpha_v\}] \qquad (3)$$

where μ and μ_v are fictitious masses associated with the dynamics of the electronic wavefunctions ψ_i and the constraints α_v, respectively. The resulting equations of motion are:

$$\mu \ddot{\psi}_i(\mathbf{r},t) = -\delta E / \delta \psi_i^*(\mathbf{r},t) + \sum_k \Lambda_{ik} \psi_k(\mathbf{r},t) \tag{4a}$$

$$M_I \ddot{\mathbf{R}}_I = -\Delta_{\mathbf{R}_I} E \tag{4b}$$

$$\mu_\nu \ddot{\alpha}_\nu = -(\delta E / \delta \alpha_\nu) \tag{4c}$$

where Λ_{ik} are the Lagrange multipliers associated with the orthonormality constraints of the wavefunctions. After a suitable initialization, the molecular dynamics proceeds while the temperature of the system is slowly reduced to zero. At this point the time derivatives of the wavefunctions are all zero and the equations (4a) are identical within a unitary transformation to the Kohn-Sham equations derived variationally from the total energy expression (2).

The formulation (3)-(4) allows for time-dependent quantum molecular dynamics simulations as well as for calculations of temperature-dependent properties in a canonical ensemble [6] using methods developed for classical molecular dynamics [7]. The last property enables searches for a global minimum via the simulated annealing algorithm.

The Car-Parrinello method is quite general, but it is particularly efficient if a plane wave basis set is used, as we do it in our calculations.

C. Study of the Mechanisms of Diamond Growth

We are conducting a theoretical research on structure, bonding, and reactions of those species on the diamond surfaces, which are essential to the growth of single crystalline diamond films.

The majority of the recent experimental and theoretical work in this area is focused on the CVD growth of diamond and diamond films [8]. With CVD techniques, single crystal diamond grain of 10μm size and nearly perfect diamond films (homoepitaxial on (001) natural diamond substrates) up to 250μm thick can now be grown [9,10]. However, for the device-applications to be practical, more controllable processes for higher quality films are needed. While our calculations may in general provide answers to existing questions in diamond growth, the main effort is on the ALE (Atomic Layer Epitaxy) of diamond. A successful ALE process will relay on the self-limiting of surface reactions so that the growth is in a controllable "digital" fashion. The achievement of ALE would almost certainly lead to better quality diamond films. The diamond research is also supported by NSF.

We have examined the ALE cycle recently announced by a Russian group [11]. The process involved the successive deposition of CH_4 and CCl_4 onto the initially chlorinated diamond surface. Denoting carbon atoms in bulk diamond as C_b, the authors of Ref. 11 suggested the following reactions:

$$C_bCl + CH_4 \text{ --> } C_b\text{-}C_bH_3 + HCl \uparrow + 8.5 \text{ kcal.} \qquad (5)$$

$$C_bH_3 + CCl_4 \text{ --> } C_b\text{-}C_bCl + 3HCl \uparrow + 25.5 \text{ kcal.} \qquad (6)$$

These reactions result in a growth of a double layer per cycle and implicitly assume growth in the (111) direction, since in this direction the surface layers with one dangling bond per atom alternate with layers containing three dangling bonds per atom. No detailed experimental conditions and quality of the resulting material and/or reactions were given.

The reaction energetics in (5-8) were estimated by using the heat of formation data, and one may come to a conclusion that these reactions are energetically favorable. However, as we will show in the following, there are steric constraints on the surface that alter these results.

Further chlorination of the chlorinated surfaces is thermodynamically unfavorable, since

$$C_bCl + CCl_4 \text{ --> } C_b\text{-}C_bCl_3 + Cl_2 \uparrow - 16\text{kcal.} \qquad (7)$$

Similarly for the hydrogenation of already hydrogenated surfaces:

$$C_bH_3 + CH_4 \text{ --> } C_b\text{-}C_bH + 3H_2 \uparrow - 53.5 \text{ kcal.} \qquad (8)$$

The reactions (5) and (6) thus fulfill the self-limiting conditions of an ALE process, since only reactions in which HCl is produced are thermodynamically favorable. The gas in excess of one monolayer coverage would only physisorb and therefore evaporate if the substrate is kept at a sufficiently high temperature.

We have performed the *Ab initio* calculations for the energetics of above reactions. The surfaces were simulated by slabs of eight layers thick and separated by 8 Å distance within a supercell scheme. Quantum molecular dynamics of Car-Parrinello type was used to search for the ground geometry of the surfaces as well as to provide the heat of formatiom data for CH_4 and CCl_4 molecules. Figure 2 shows the optimized structure of the hydrogenated diamond surface (note this surface is terminated with CH_3 group, while the usual hydrogenated surface is terminated with single dangling bonds saturated by hydrogen.) Because of the steric repulsions the CH_3 groups rotates 60° from each other and one of the hydrogen atoms on CH_3 has moved outward by about 0.4 Å while the other two moved inward by 0.1 Å. A similar structure has been obtained by Mehandru and Anderson [8] using semi-empirical methods. This structure is in a local-minimum. If we allow for slight heating surface becomes very unstable. This is also the common view of many experimentalists and it leads one to question the feasibility of CH_3 full-coverage surface as a precursor for the ALE growth. However, the possibility of this type ALE mechanism at lower CH_3 coverage remains open.

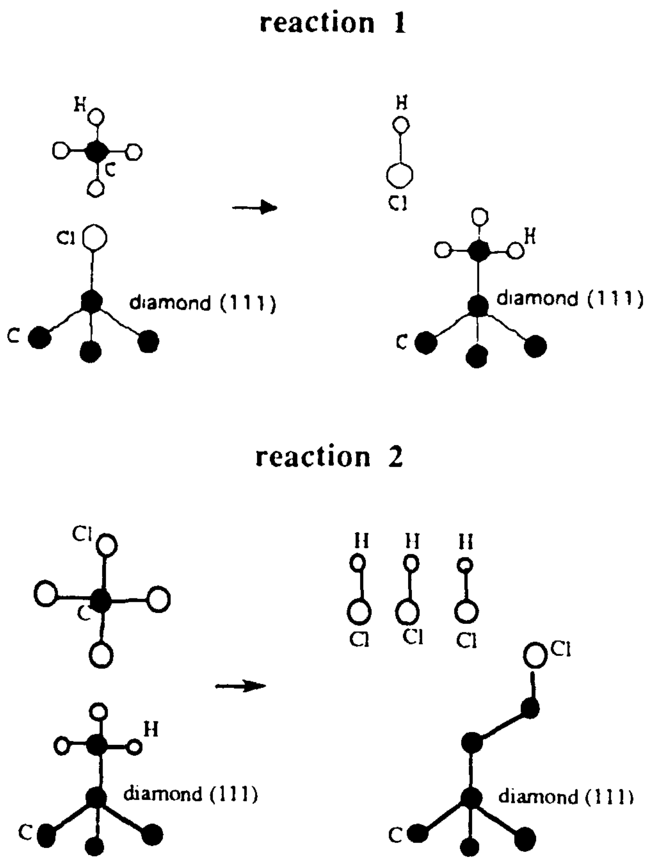

Figure 1. The proposed ALE cycle.

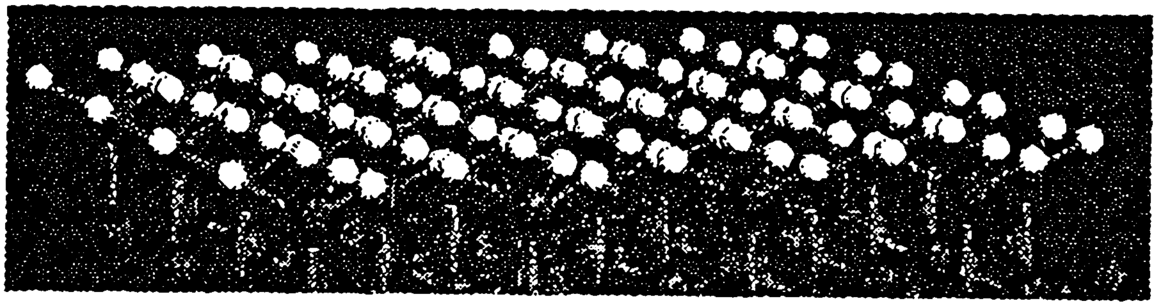

Figure 2. Hydrogenated diamond surface.

Figure 3 shows the fully relaxed chlorinated diamond surfaces. The C-Cl bond length is 1.82 Å , which is a few per cent longer than in the CCl_4 molecule. The chlorine atoms have moved outward from their initial position where the C-Cl bond was set to be same as in CCl_4 molecules (1.76 Å), while top layer carbon atoms moved inward. Due to the relatively large size of the chlorine atoms (covalent radius of 1.0 Å , while that of carbon is 0.75 Å), there are strong interactions between the chlorine atoms on the surface. The electronic energy levels are crossing because of the over crowding. This suggests that using the saturation coverage of Cl to saturate the single dangling bonds on the (111) surface is unrealistic.

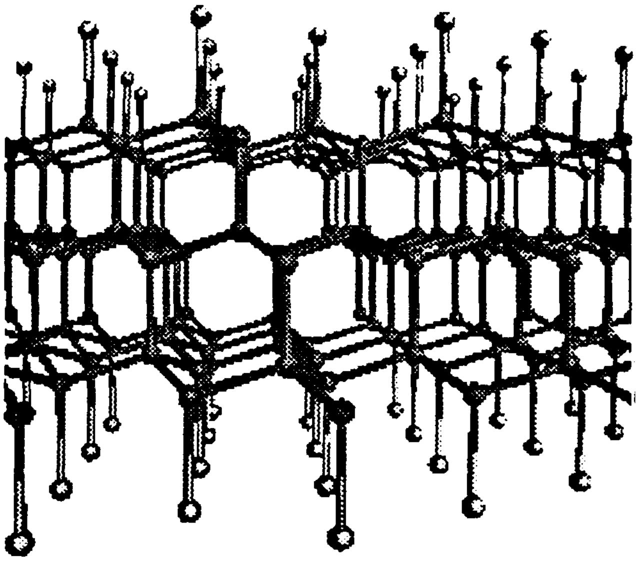

Figure 3. The chlorinated diamond surface.

To obtain the reaction energetics, we calculated the molecular structures for CH_4 and CCl_4 within the same method. The C-H single bonding energy in CH_4 is 4.4 eV compared the measured value [12] of 4.3 eV. The reaction energetics for the proposed ALE process was obtained as follows,

$$C_bCl + CH_4 \dashrightarrow C_b\text{-}C_bH_3 + HCl\uparrow + 5\ \text{kcal}$$

$$C_bH_3 + CCl_4 \dashrightarrow C_b\text{-}C_bCl + 3HCl\uparrow + 60\ \text{kcal.}$$

This shows that the ALE process of 5-6 are energetically favorable. The difference between the calculated energy gain and the bond energy estimate is mainly due to the fact that the steric repulsion between hydrogen atoms on the surface is much stronger than in the free molecules such as CH_4. This leads to a higher energy for the hydrogenated surface relative to the bond energy estimate and hence less energy gain in reaction (5) and more in reaction (6).

Although the processed ALE process is energetically favorable, we expect difficulties in achieving it. Because of the large size of the chlorine atoms relative to the diamond lattice and the steric repulsion between methyl units, high kinetic barriers are likely. However, similar ALE process may be possible at lower coverage of diamond surface and/or with fluorine-based cycles. The possibilities of ALE reactions on (100) and (110) surfaces are under investigation.

D. Hydrogenated diamond (100) surface

Introduction. The diamond (100) surface has been studied previously using semi-empirical and density functional methods. We believe that before further progress can be made towards ALE on this surface, a more accurate study must be made of its geometry. Presently, we have concentrated on the geometry and surface energies of the dihydride (1×1) and monohydride (2×1) reconstructions of this surface. These two configurations show potential for being conducive for a diamond ALE growth mechanism.

Theoretical Method. The diamond (100) symmetric dihydride and monohydride surfaces were modeled using the Car-Parrinello method which entails the selection of an appropriate unit cell that will effectively model the surface effects. For both surfaces, the total-energy was calculated with a plane wave basis with an energy cutoff of 35 Rydbergs. For the dihydride surface, the total number of carbon and hydrogen atoms were sixty three and thirty six respectively. The nine atoms per layer were oriented in a three by three square with a total of seven layers of carbon and nine layers of vacuum. Each of the eighteen surface carbons had their remaining bonds saturated with hydrogen.

For the monohydride surface, the total number of carbon and hydrogen atoms were forty eight and sixteen respectively. The unit cell had eight atoms per layer arranged in a two by four rectangle with six layers of carbon and ten layers of vacuum. Adjacent bonds between pairs of atoms in the longer direction were left unsaturated and the remaining bond for each surface carbon was saturated with hydrogen.

The calculations were run on a Cray Y-MP computer with the first step being to converge the electron density to the ground state configuration and the total energy of the unrelaxed geometry to a minimum. Then the atoms were allowed to move via the steepest descents method until the total energy was minimized, thus reaching the converged geometry. The time step used in moving the atoms was 10 a.u. and the total number of steps for relaxation was in excess of 1000. From the results of these calculations we were able to obtain the surface formation energies for the dihydride and monohydride diamond surfaces as a function of the H chemical potential. The surface formation energies were calculated by

$$\Omega = E_S + E_{ZPE} - n_C * \mu_C - n_H * \mu_H \qquad (9)$$

where E_S is the total energy of the surface, and n_C and n_H are the number of carbon and hydrogen atoms in the unit cell. The zero point energy E_{ZPE} was taken to be proportional to the number of H atoms and thus independent of the structure. This approximation is justified when comparing different hydrogenated diamond (100) surfaces. Note that μ_H is the hydrogen chemical potential and the carbon chemical potential μ_C has been taken to be the chemical potential of bulk diamond. In our calculations the origin of the μ_H scale has been taken to yield a zero formation energy for methane.

Results for the diamond (100) surface. For the diamond (100) symmetric dihydride surface we noted that the structure remained symmetric when the atoms were allowed to move. The dominant feature of the simulation was the closing of the angle of the dihydride pairs due to the steric repulsion of the hydrogen atoms of adjacent pairs. The angle between pairs started at the diamond bond angle of 109.47 degrees and closed to 84.73 degrees. The C-H bond length for the dihydride pairs was found to be 1.054Å. This puts the distance between the hydrogen atoms of a dihydride pair at 1.421Å and the distance between hydrogen atoms of adjacent pairs at 1.096Å. As expected, the interplanar distances of the surface planes were not the same as that of the bulk crystal. In the bulk at equilibrium, the interplanar distance is 0.889Å between all planes. The converged geometry yielded distances of d_{12} = 0.838Å, d_{23} = 0.904Å and d_{34} = 0.891Å. where d_{ij} denotes the distance between the ith and jth planes. The surface formation energy for the dihydride surface is shown in Figure 4 as a plot of energy versus the H chemical potential.

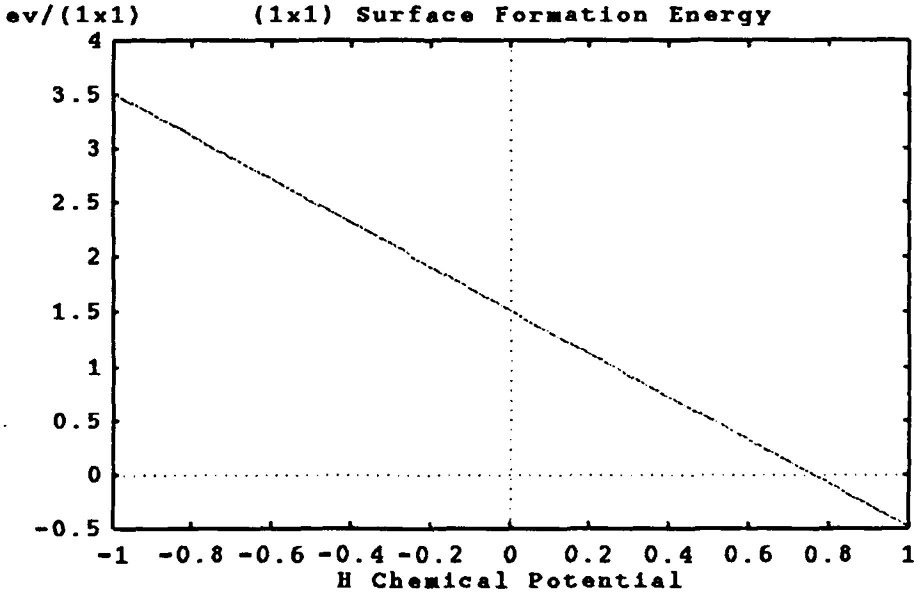

Figure 4. Plot of surface formation energy.

At the time of writing, results for the diamond (100) monohydride surface were still being calculated. The electron density has been converged for the starting geometry and the molecular dynamics runs have been started.

Discussion of the diamond (100) surface. The construction of the diamond (100) dihydride surface corresponds to experimental data found by LEED patterns [13]. No twisting or deformation of the basic (1×1) structure was found from starting the simulation in the equilibrium diamond geometry (see Figure 5). It is expected that interplanar distances are contracted for d_{12} and d_{34}, while the d_{23} distance is expanded. Our interplanar distances coincide with previous studies [8] for all but the d_{12} distance. Our result differed from the equilibrium geometry by -5.7% while they found a -16.9%(-21.4%) difference, where the number in parantheses denotes a spin-paired result. Their results were calculated using the semi-empirical atom superposition and electron delocalization (ASED-MO) technique. For a surface where all of the surface carbon bonds are hydrogenated, we would expect only a modest contraction. The difference predicted via the ASED-MO method is of the order of a bare surface contraction due to a Jahn-Teller distortion. Since all of the bonds are saturated, we believe that our modest displacement is a more accurate prediction of the hydrogenated (1×1) diamond surface in the ground state geometry.

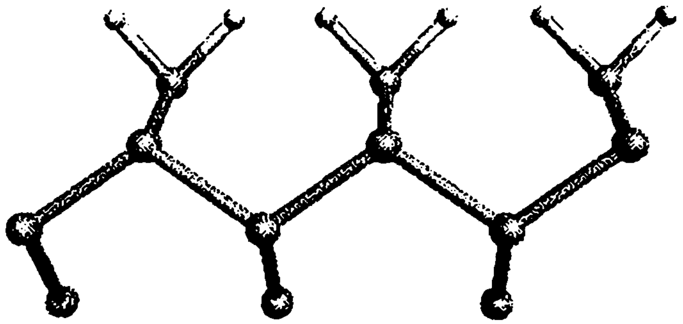

Figure 5. The converged dihydride pairs.

Future research plans/goals for the diamond (100) surface. The Car-Parrinello method requires many hours of Cray Y-MP time when doing large scale surface calculations. This constraint implies that we need to carefully select future work that will yield a possible ALE growth mechanism. The above results can be considered the foundation for further research, since the diamond (100) surface structures and formation energies are needed before research into diamond ALE mechanisms can begin. We will also attempt to characterize the adsorption and bonding of H, CH_3, CH_2 and C_2H_2 onto the diamond (100) (1×1) and (2×1) surfaces that we have converged above. This is the next logical step towards an ALE growth mechanism as adsorption of some or all of the hydrocarbons and hydrogen will be an essential part of any growth mechanism.

Also in our plans are additional studies of the diamond (100) surfaces with the Car-Parrinello method. The (3×1) reconstruction and the bare (100) surface will be studied when the new Cray Y-MP C90 computer becomes available this winter. We hope that from studying the (3×1) reconstruction we can determine whether it corresponds to the Si(100) (3×1) surface [14] as being the reconstruction with the lowest surface formation energy for the (100) plane. While experimental research has not found any evidence for reconstructions of higher order than (2×1) for diamond [13], we hope that further calculations will help to explain or refute these findings. The bare surface presents a challenge to study with density functional-based methods due to the number of unsaturated bonds. We would like to determine the geometry of the bare surface at the minimum of the total energy. This finding would be very useful in formulating an ALE growth mechanism that relies on temperature programmed desorption of the H atoms.

E. Impurities in GaN and AlN

Introduction and computational methodology. In our study of defects in GaN and AlN we focus our attention on two questions relevant for the experiment, namely the formation energies of substitutional impurities, and their electronic structure. The first impurity which is currently under study is substitutional C. The importance of this impurity stems from the fact that carbon atoms are always incorporated in nitrides during the process of growth because of the growth technique. Our calculations will provide formation energies of C, obtained as a function of the Fermi level position, i.e., as a function of type of dopants (donors or acceptors) and of their concentration. It is important to observe that C impurity may be the amphoteric, i.e., the dopant site will depend on the conditions of growth. In consequence, the C atom belonging to Group IV of the Periodic Table will act as a donor in the Ga sit, or as an acceptor on the N site.

As for surface problems, the computations are performed using the quantum molecular dynamics. We also use the large unit cell method. In this approach, the impurities are repeated periodically in the host crystal. At present, the considered unit cells contain 32 atoms. The energy cutoff for the plane wave basis is 30 Ry.

Preliminary results for GaN:C. The first stage of calculations consisted in finding the equilibrium lattice parameters for the hexagonal GaN crystal. The obtained lattice constant is smaller than the experimental one by about 2%, which is a typical error associated with the usage of the local density approximation.

The formation energy of a substitutional C impurity is given by

$$E_{form} = E[GaN{:}C_X] - E[GaN] + \mu(X) - \mu(C)\,, \qquad (10)$$

where E is the total energy, μ is the chemical potential, and X=Ga or N. Chemical potentials depend on the source of atoms involved in the process, and therefore on the actual experimental situation. The preliminary values are $E_{form}(C_{Ga})$=4.1 eV, and $E_{form}(C_N)$=4.3 eV. We have assumed that the chemical potentials are those of solid C, Ga, and N, and used the experimental values of the cohesive energies. Further, we have also assumed that C is in the neutral charge state (Eq. 10 holds for this case).

In the calculations all atoms around the impurity were allowed to relax. The inclusion of this effect is important for obtaining correct results. The atomic relaxation lowers the energy by 0.28 eV for C_{Ga}, and by 0.11 eV for C_N. Note that the former value is larger than the latter one due to a larger difference of atomic radii. The relaxation induces energy shifts of impurity states by about 0.3 eV.

The electronic structure of C is of obvious technological importance. It is well established that amphoteric Ge in GaAs acts as a shallow impurity, i.e., is a shallow donor or a shallow acceptor depending on its location. Based on this result one could expect that C be a shallow impurity as well. However, our preliminary results indicate that this is not the case. C_{Ga} introduces a deep level in the optical band gap, located about 1.0 eV below the bottom of the conduction band. On the other hand, C_N tintroduces an acceptor level at about 0.3 eV above the valence band top. This behavior is probably due to the very large electronegativities of N and C, which result in a tendency to form highly localized states.

Further research plans. Our current effort is focused on increasing the dimensions of the large unit cell. This will allow us to obtain both convergent values of formation energies, and more reliable positions of impurity-related states. Next, chemical potentials will be adjusted to meet the actual experimental conditions.

Further studies will be extended to other impurities which are potential donors in the investigated materials, such as Zn, Si, and Ge, and to AlN as a host crystal.

References

1. Q.-M. Zhang, J.-Y. Yi and J. Bernholc, Phys. Rev. Lett. **66**, 2633 (1991).
2. Q.-M. Zhang, C. Wang, and J. Bernholc, Bull. Amer. Phys. Soc. **36**, 836 (1991) and to be published.
3. P. Bendt and A. Zunger, Phys. Rev. B **26**, 3114 (1982); D. M. Wood and A. Zunger, J. Phys. A **18**, 1343 (1985).
4. P. Bendt and A. Zunger, Phys. Rev. Lett. **50**, 1684 (1983).
5. R. Car and M. Parinello, Phys. Rev. Lett. **55**, 2471 (1985).
6. F. Buda, R. Car, and M. Parinello, Phys. Rev. B **41**, 1680 (1990).
7. S. Nosé, Mol. Phys. **52**, 255 (1984).
8. S. P. Mehandru and A. B. Anderson, Surface Sci. **248**, 369 (1991).
9. A. R. Badzian, et al, *New Diamond Science and Technology*, p 549.
10. T. Tsuno, T. Imai, et al, Japanese Journal of Applied Physics, **30**, 1063 (1991).

11. V. B. Aleskovski and V. E. Drozd, *Proc. First Inter. Symp. on Atomic Layer Epitaxy*, edited by L. Niinisto, Acta Polytechnica Scandinavica, Chem. Techn. and Metallurgy Ser. **195**.p. 156 (1990).
12. *Advanced Organic Chemistry*, Mcgraw-Hill Series In Advanced Chemistry, by J. March
13. J. D. Kubiak, A. V. Hamza, R. H. Stulen, E. C. Sowa, K. W. Kolasinski and M. A. Van Howe, Proceedings of the Second International Conference on the New Diamond Science and Technology, Washington DC, September 1990. Published by Materials Research Society, Pittsburgh PA.
14. J. E. Northrup, Phys. Rev. B **44** 1419 (1991).

THIN FILM GROWTH AND CHARACTERIZATION OF CARBON-BASED MATERIALS

III. Properties of Interfaces of Diamond*

R.J. Nemanich, L. Bergman, K.F. Turner, J. van der Weide, and T.P. Humphreys
Department of Physics and Department of Materials Science and Engineering
North Carolina State University
Raleigh, NC 27695-8202

Results related to two different interface aspects involving diamond are described; (1) the initial stages of CVD diamond film growth, and (2) the negative electron affinity and formation of metal-diamond interfaces. The surface and interface properties are probed with STM, Raman scattering/photoluminescence and angle-resolved uv-photoemission spectroscopy (ARUPS). STM measurements of diamond nuclei on Si after various plasma growth processes show both flat and hillocked structures characteristic of 2-dimensional and 3-dimensional growth modes, respectively. STS measurements show distinct I-V characteristics of the nuclei and the substrate. The presence of optical defects and the diamond quality are studied with micro-Raman/photoluminescence measurements. The results indicate an increased density of impurity related defects during the initial stages of growth. The interface properties of Ti on natural crystal (111) and (100) surfaces are studied with ARUPS using 21.2eV HeI emission. Prior to deposition the diamond (111) is chemically cleaned, and a sharp (0.5eV FWHM) peak is observed at the position of the conduction band minimum, indicating a negative electron affinity surface. After a subsequent argon plasma clean this peak disappears, while the spectrum shows a shift of 0.5 eV towards higher energies. Upon sub-monolayer titanium deposition on (111) diamond, the negative electron affinity peak reappears. Further titanium depositions causes this titanium induced negative electron affinity peak to be attenuated, indicating that the emission originates from the interface. A similar experiment, done on the diamond (100) surface, however, does not result in a negative electron affinity. By determining the relative positions of the diamond valence band edge and the titanium Fermi level, the Schottky barrier height of titanium on diamond is measured. A model, based on the Schottky barrier height of titanium on diamond, and the work function of titanium, is proposed, for the observed titanium induced negative electron affinity.

---

*To appear in the Proceedings of the 7th Trieste Semiconductor Symposium on Wide-Band-Gap Semiconductors, edited by C. G. Van de Walle.

I Introduction

Continuing advances in the CVD growth of doped diamond thin films offer the possibility of diamond semiconductor devices.[1] Because large diamond substrates are, at this time, prohibitively expensive, most potential electronic applications have focussed on heteroepitaxial structures. The nucleation of diamond on non-diamond substrates has, however, proved difficult. Because of the potential for electronic applications, much effort has been focussed on the nucleation and growth of diamond on Si. While small regions of heteroepitaxial growth have recently been reported on SiC and BN substrates,[2,3] only polycrystalline growth has been achieved on Si and other commonly used substrates. In fact, without special processing of the substrate, the initial nucleation rate is so low, that no diamond growth is achieved within an exposure to the growth conditions for over 60 min. In this study, the initial growth nucleation and growth modes of diamond on Si are studied by STM and Raman photoluminescence measurements.

To achieve diamond devices, metal contacts and Schottky barriers will be critical. One of the most important advances with regards to device applications is the growth of p-type diamond with boron incorporation. This is achieved either by implantation or by incorporation during the growth. Device structures have been demonstrated with the p-type material, and it is apparent that understanding contacts and Schottky barrier properties will be critical. Because of the large band-gap, diamond has the potential of high temperature operation, thus it is critical to obtain contacts and Schottky barrier structures that are both chemically and electrically stable at high temperature operation.

A particularly interesting property of diamond is that under some surface preparation conditions, a negative electron affinity can be achieved. The term negative electron affinity means that the conduction band of the semiconductor at or near the surface is above the vacuum level (i.e.. the zero kinetic energy of an electron in free space.) In this condition electrons in the conduction band will not be bound in the sample and electron emission can occur. In this study we demonstrate that the electron affinity is dependent on the sample surface preparation. Both surface termination and overlayer coverage can substantially affect the electron affinity.

II. Experimental

The diamond films were prepared by microwave plasma CVD on 1 inch diameter n-type Si(111) or Si(100) substrates. The substrates were polished with 0.25 μm diamond powder, followed by an ultrasonic clean in TCE, acetone, methanol, a rinse with de-ionized water and then a drying with nitrogen. A 30 minute hydrogen plasma etch was performed before growth. The growth occurred at a pressure of 25 Torr, a methane to hydrogen ration of 1% with a total flow rate of 1000 sccm and a substrate temperature of ~750°C. No intentional dopant was used in the growth process. SEM micrographs were obtained of the surfaces to show the surface topography on a large scale and to provide an estimate of the nucleation density and the evolution of growth on the surface. Raman spectroscopy and photoluminescence analysis were also performed. The subsequent growth was observed by stopping the growth process after 1.5, 3, 5, 7, 10, 17 and 40 hours of deposition.

The STM analysis of the diamond was done over a wide range of parameters. All of the analysis was performed using an Park Scientific Instruments SU-200 scanning tunneling microscope operated in the ambient atmosphere. The surfaces were scanned over several scan ranges (20Å - 5μm), tunneling currents (0.5 nA - 4.0 nA), and at both positive and negative bias voltages. With the STM used, a positive bias voltage corresponds to a voltage applied to the tip that is positive relative to the sample.

Current-voltage measurements were also performed using the STM, in a process that is called tunneling spectroscopy. In these measurements, the bias voltage is ramped from positive to negative values, and the current monitored. All current-voltage measurements presented are averaged over many voltage cycles and were representative of the I-V characteristics of the entire surface. Measurements also allowed for measurement of the surface density of states, which is proportional to the ratio of the differential conductance to the conductance.

The photoemission data presented in this paper, were obtained from natural single crystal diamond. The diamond substrates used in this study were 3 x 3 x 0.5 mm^3, type IIb wafers, with a (111) or a (100) surface orientation. These wafers are p-type semiconducting, with typical resistivities ranging from 1.3 kΩ-cm to 16 kΩ-cm. The substrates were polished with 0.25 μm diamond grit and cleaned in a boiling chromic acid solution before loading. Once in vacuum the diamond (111) was further cleaned in a plasma cleaning chamber by exposing it to a remote, RF induced, argon plasma. During the exposure the diamond was heated to 350°C. The diamond (100) was cleaned by heating it in UHV to about 600°C for 10 min. Titanium was evaporated by resistively heating a titanium filament, and spectra were taken at increasing thicknesses. The thickness of the deposited films was monitored with a crystal rate monitor. The plasma cleaning chamber is connected to the ARUPS chamber through an UHV transfer system. The photoemission was excited with 21.21 eV HeI radiation, and the data presented here was obtained with an angle resolved ultraviolet photoemission spectroscopy (ARUPS) system, which included a 50 mm radius hemispherical analyzer with an angular resolution of 2°. A bias voltage of ~1 V or less, was applied to the sample during the measurements to overcome the work function of the analyzer. The bias voltage allowed the collection of the low energy electrons, which show the negative electron affinity effect .

III. Results and Discussion

A. Nucleation and Initial Growth

The results of the investigation of the initial stages of diamond growth can be broken down into different properties: changes in the surface which occur during growth, observation and analysis of the nuclei formed during growth, and the electronic properties of the nuclei and the substrate surface. STM analysis of diamond and diamond-like materials has been described in several recent studies. Previous works using STM by the authors have examined topography of CVD doped diamond films and undoped nuclei, changes in the growth surface and nuclei during growth, and examination of Ni contacts to single crystal diamond. [4-7] T. Tsuno and others have examined homoepitaxial CVD diamond films grown on the diamond (001) surface and observed surface reconstructions. [7] M. P. Everson et al have investigated the structure of doped nuclei grown on silicon. [8] The only group to report successful STM examination of thick undoped diamond films has come from H. G. Busmann et.al. [9] Several other groups have examined amorphic diamond and diamond-like carbon. [10-14] Discusions of the theory and practice of imaging diamond can be found in these references.

The changes in the surface which occur during growth can be examined before the first observation of nucleation. Figure 1 shows the surface structure of one of the samples as viewed by STM. Comparisons of the 30 minute and the 60 minute growth samples showed that the surface of the 60 minute sample appeared to be rougher than the 30 minute sample. Neither sample showed diamond nucleation. The surface, however, showed an increased roughness for the longer growth. This indicates the formation of a surface layer, presumably SiC or disordered carbon.

During the initial phase of the growth process examined here, a majority of nuclei exhibit a 3-dimensional structure. A minority of the nuclei do exhibit a more 2-dimensional structure, which indicates a 2-dimensional growth mode. Figure 2 shows both flat and hillocked structures characteristic of 2-dimensional and 3-dimensional growth modes, respectively. The top of the flat nucleus shown is smooth to within ~20Å and has a "height" to "width" ratio of 1:4. The surface of the nucleus is parallel to the substrate and indicates that the interactions with the substrate contribute to the growth and morphology. This is an important aspect because it is likely that the initial diamond has formed in the scratched regions. We would suggest that it is possible that the initial diamond formation in the scratches is highly disordered, thus allowing the substrate interactions to contribute to determination of the growth morphology. The second image shows several nuclei, one of which appears to be twinned, which have "height" to "width" ratios of ~1:2. The fact that both types of nuclei were observed after the same exposure to growth, supports the fact that two distinct modes exist and that the 2-D mode is not merely an early manifestation of a 3-D growth mode. Evidence of this 2-dimensional mode is interesting because it may be an indication that conformal growth is possible and if it could be enhanced, creating planer diamond films with fewer polycrystaline domains might be possible.

Tunneling spectroscopy measurements show distinct I-V characteristics of the nuclei and the substrate. Examples of I-V curves obtained from different points are shown in Figure 3. The ability to distinquish between the types of materials on the surface is an important one. The curve obtained by tunneling to the diamond nucleus is smoothly varying and shows little response at positive bias voltages. The substrate I-V curve shows much more structure including a large change in the current starting at +2.5 volts. The "peaks" in the I-V curve taken over the substrate are indicative of the electronic structure of the carbonic layer that has formed on the substrate during growth. These "peaks" may be a result of absorbates, bonded to the silicon, which are weakly connected to bulk states.

The ability to carry out tunneling experiments from undoped diamond regions is in itself unique since diamond has such a high electrical resistivity. To probe the defect and impurity properties of the initial stages of growth, micro-photoluminescence measurements were carried out as a function of growth time. In this experiment, the same sample was measured after various growth times. A relatively strong feature was observed in the micro-photoluminescence at an emission energy of 1.68eV, which is shown in Figure 4. There has been considerable discussion about the origin of this feature. It occurs at an energy near to that of the GR1 peak in single crystal diamond. This feature has been assigned to a neutral vacancy. Since vacancies are mobile in diamond at temperatures ~800°C, it is unlikely that the 1.68eV feature in the CVD films (growth temperature ~800°C) is due to a vacancy. It has also been suggested that the feature is due to a complex involving Si and/or N.[15,16]

The results of the experiment are shown in Figure 5. The relative intensity of the 1.68eV feature to the Raman diamond feature reaches a maximum after ~7hr and then is reduced with increased growth time. The absolute intensity of the 1.68eV feature actually increases at least up to a growth time of 15 hrs (at this time the substrate is nearly completely covered). Thus we can conclude that there is initially a higher rate of impurity incorporation in the film. From the data, it can also be concluded that a higher concentration of defect centers exists near the interface between the diamond and the silicon, with a lower concentration found in the bulk. It is now well established that Si is etched in the presence of atomic H, with SiH_4 being released. We suggest that the observed photoluminescence trend is due to the incorporation of Si which has been etched from the substrate. The rate of incorporation decreases when the Si substrate is covered by diamond after subsequent growth.

B. Schottky Barrier Height Measurement

Diamond-metal interfaces and their properties as electrical contacts have received recent attention, and both ohmic and rectifying contacts to both natural diamond and CVD grown diamond have been reported [6,17-21]. To fully understand the rectifying contact it is necessary to determine the Schottky barrier characteristics. Current-voltage measurements of the rectifying contacts typically show a high ideality factor and cannot be used for an accurate Schottky barrier determination [22]. Photoemission, however, has been successfully used to measure the Schottky barrier height of Al and Au on diamond [23] .

Previous current-voltage measurements have demonstrated that titanium, deposited at room temperatures, forms a rectifying contact to p-type diamond. Upon annealing to >400°C the current-voltage characteristics become ohmic.[21]. It has been suggested that this transformation is due to the formation of a titanium carbide [17]. In a previous study we have shown that titanium carbide formation does indeed occur in the same temperature range in which titanium contacts are found to change from rectifying to ohmic [24]. In this paper we report a UV photoemission study of thin titanium layers deposited on a diamond (111) surface. From the measurements the Schottky barrier height of titanium on p-type diamond (111) is determined.

The Schottky barrier height of a metal on a p-type semiconductor is defined as the difference between the valence band edge of the semiconductor and the Fermi level of the metal at the interface. The determination of the Schottky barrier height from UV photoemission, relies on the fact that features of both the metal and the underlying semiconductor are visible in one spectrum. Experiments are therefore limited to thin metal films with a thickness on the order of the mean free path of the electrons (~5Å). Even at metal coverages less than the mean free path, it is not always possible to determine the position of the valence band edge accurately from the spectra, since emission from the metal d-band obscures the relatively weak semiconductor valence band emission. In those cases, a more accurate determination can be made, by relating the valence band edge to a feature in the diamond spectra that does remain visible at higher metal coverages. In this analysis it is assumed that shifts in the diamond features are uniform so that relative positions are maintained. In the experiments on the (111) surface, the valence band edge was determined from the spectrum of the argon plasma cleaned diamond and related to a stronger emission feature at lower energies, labeled B, in Figure 6. Although this diamond feature was attenuated upon metal coverage, it remained much more visible than the valence band edge. In order to determine the valence band edge from the position of peak B, their relative positions should not change upon titanium deposition. Since the relative positions of feature B and the valence band edge did not change after the first metal depositions in which both were visible, we do not expect this to occur at the higher metal thicknesses.

The location of the valence band edge was determined by extrapolating the spectrum to zero, as illustrated in Figure 7. The valence band edge was found to be 8.2 eV above feature B. After the first titanium deposition the diamond spectrum shifted 0.5 eV towards lower energies, indicating a change in the pinning position of the Fermi level in the gap. No Fermi level emission due to the titanium could be discerned, however, at this coverage. Upon further titanium deposition, emission from the d-bands of titanium became pronounced, and the Fermi level could be clearly discerned. The position of the valence band edge, however, became more difficult to locate. Based on the position of feature B, no further shifts in the diamond spectrum were observed. This indicates that the Fermi level was pinned, and the Schottky barrier height established, after the first titanium deposition. The Fermi level was found to be 9.2 eV above feature B. Since the valence band edge was 8.2 eV above B this results in a Schottky barrier height for titanium on p-type diamond (111) of 1.0±0.2 eV.

Similar measurements were performed for titanium on the diamond (100) surface, as shown in Figure 8. The position of the valence band edge, relative to peak B, was determined again from the clean diamond (100) surface, and was found to be 8.0 eV, in agreement with the value found from the (111) surface. No shifts were observed before cleaning, and no significant shifts occurred upon titanium deposition. The position of the Fermi level was determined, and found to be 9.4 eV above feature B. The Schottky barrier height of titanium on the diamond (100) surface was therefore found to be 1.5±0.2 eV. Reported values for the Schottky barrier height of titanium on CVD grown diamond films range from 0.9(+0.5/-0.2)eV [24] to 1.3 eV [25].

C. Negative Electron Affinity

The relation between the bands of a semiconductor and the vacuum level can be described by the electron affinity. This quantity which is the energy difference between the conduction band minimum and the vacuum level, is an important parameter in the Schottky-Mott model for Schottky barrier heights. The electron affinity is however dependent on the surface structure of the crystal. A dipole layer on the surface will shift the potential of the material with respect to the vacuum, thus changing the electron affinity. The dipole layer can result from surface structures such as reconstruction or molecular absorption or interface structures such as Schottky barriers or heterojunctions.

Photoemission spectra of negative electron affinity surfaces generally show a sharp peak at the low kinetic energy end of the spectrum. This peak is attributed to emission of electrons that are quasi-thermalized to the bottom of the conduction band of the semiconductor. For materials with a positive electron affinity, the conduction band minimum is below the vacuum level, and the quasi-thermalized electrons are trapped in the sample. In the experiments described here, the presence of a sharp peak at the onset of the photoemission will be considered as an indication of a negative electron affinity surface.

Hydrogen Terminated Surfaces.

We initiated the study of the negative electron affinity of diamond by verifying the experiment of Pate [26] in which the relation between the negative electron affinity effect and the presence of hydrogen on the surface is established. The H-terminated surfaces were obtained by polishing and etching a diamond (111) wafer. Followed by a low temperature anneal (350°C) to desorb contaminants. Photoemission spectra from the diamond before and after thermal desorption of the hydrogen are shown in Figure 9. The negative electron affinity of the surface, which results in the sharp peak at the low energy end of the spectrum, has clearly been removed from the surface. Since the annealing temperature used to obtain the effect is the same as the reported temperature for the desorption of hydrogen, this suggest that hydrogen on the surface plays a role in the negative electron affinity effect. The spectra of the diamond before and after annealing, are followed by spectra from the diamond after exposure to molecular and mono-atomic hydrogen. As is shown in Figure 9, the molecular hydrogen has no effect on the electron affinity of the surface. The mono-atomic hydrogen, however, returned the surface to a negative electron affinity state. The fact that exposure to mono-atomic hydrogen causes the surface to exhibit a negative electron affinity confirms that the hydrogen is associated with the negative electron affinity. The difference between the results after exposure to molecular and mono-atomic hydrogen suggest that the hydrogen has to be chemically bonded to the surface. The series is concluded by a spectrum of the diamond after another high temperature anneal, which shows that the cycle is repeatable.

In a second series of experiments, described in Figure 10, the diamond (111) was exposed to a hydrogen plasma after loading, and the spectrum shows the presence of a negative electron affinity. After a subsequent exposure to an argon plasma, however, the sharp peak that is associated with a negative electron affinity, was absent. Since the negative electron affinity is associated with the presence of hydrogen on the surface we conclude that the argon plasma removed the hydrogen from the surface. Exposure to another hydrogen plasma causes the negative electron affinity effect to reappear. This is to be expected in light of the first experiment where exposure to mono-atomic hydrogen also caused the negative electron affinity to reappear.

Metal Induced Negative Electron Affinity.

The potential of metals inducing a negative electron affinity were explored. In this case the initial starting surface was a diamond (111) surface treated with a remotely excited Ar plasma to induce a surface with a slightly positive electron affinity. After the first titanium dose a sharp peak, similar to the one found on the hydrogen passivated diamond (111) surface, develops at the low energy end of the spectrum. In the same spectrum a 0.5 eV shift towards lower energies is observed. For increasing titanium coverages the peak is attenuated, and no further shifts in the diamond features are observed. We attribute this peak to a titanium induced negative electron affinity. This would be due to a lowering of the work function by the titanium, as illustrated in Figure 11. Before the titanium deposition the Fermi level at the surface is 0.5 eV above the valence band edge. The vacuum level was determined from the low energy cutoff point of the emission, and is found to be about 5.5 eV above the valence band edge. Using a value of 5.45 eV for the bandgap of diamond we find therefore the vacuum level to be ~0.05 eV above the conduction band edge; electrons that are quasi-thermalized to the bottom of the conduction band are therefore unable to escape the surface. After the first sub-monolayer of titanium is deposited, the Fermi level is pinned at 1.0 eV above the valence band edge, which is the Schottky barrier height described in the previous section. The effective work function of the surface is now determined by the work function of the titanium. Using the value of 4.33 eV for the work function of bulk titanium [27] we find that the vacuum level of the surface is now located 0.2 eV below the conduction band edge and quasi-thermalized electrons can escape, causing the sharp peak in the spectrum. The fact that this peak is due to the interface of the diamond and the titanium, can be deduced from the attenuation of the peak as a function of coverage. Note that in this model the Schottky barrier height plays an important role in determining the position of the vacuum energy level. In Figure 10.b. the titanium-diamond(100) interface is described. Here the Schottky barrier height is 1.5 eV and the vacuum level lies now above the conduction band edge. Based on this model we do not expect a negative electron affinity surface. This is supported by the data, as can be seen in Figure 8. No low energy peak appears upon titanium coverage. It should be noted, that the model presented here, is the reverse from the Schottky-Mott model. There the Schottky barrier height is determined by aligning the vacuum levels of the metal and the semiconductor.

IV Conclusions

The initial stages of diamond growth show both substrate interactions which lead to non-diamond structures and diamond nuclei which form at scratches on the surface. Even though the initial diamond formation occurs in the scratches, the nuclei growth morphology is related to the substrate. We propose that the initial diamond formation is highly disordered and that as the growth proceeds beyond the scratches, the substrate interactions contribute to the growth morphology. Because of the high resistivity of undoped diamond, tunneling to these structures was not anticipated. Defect structures were observed in the microphotoluminescence measurements. These defects were apparently associated with Si impurities which were due to etching of the exposed substrate.

From the UV photoemission spectroscopy measurements presented here, a Schottky barrier height of 1.0±0.2 eV was found for the titanium-diamond (111) interface, and 1.5±0.2 eV for the titanium-diamond (100) interface It was found that the Schottky barrier heights were established for sub-monolayer titanium coverages. Upon titanium deposition on the diamond (111) surface, a sharp (0.5 eV FWHM) peak developed at the position of the conduction band edge. This is indicative of a negative electron affinity surface. Negative electron affinity surfaces are commonly obtained on III-V semiconductors by depositing a thin layer of a low work function material such as cesium or cesium-oxide. This study shows that it is possible to obtain a negative electron affinity on diamond (111) by depositing a sub-monolayer of a titanium, and suggests the possibility of inducing a negative electron affinity on diamond using other transition metals. A model for the observed negative electron affinity was presented, based on the Schottky barrier height of the diamond-metal interface, and the work function of the metal.

Acknowledgments: We thank B. Stoner and J.T. Glass for providing the initial diamond growth films, K. Das of Kobe Research for his help in establishing the diamond cleaning procedure, T. P. Schneider for the plasma cleaning work, and R. Rudder and R. Markunas of RTI for helpful discussions. This work is supported in part by the ONR through grants, N00014-92-J-1477, N00014-90-J-1604, N00014-90-J-1707, the NSF through grant DMR 9204285, and the MITI of Japan through the NEDO program.

References

1. R.J. Nemanich, Annu. Rev. Mater. Sci. **21**, 535 (1991).
2. B.R. Stoner and J.T. Glass, Appl. Phys. Lett. **60**, 698 (1992).
3. S. Koizumi, T. Murakami, T. Inuzuka, and K. Suzuki, Appl. Phys. Lett. **57**, 563 (1990).
4. K. F. Turner, B. R. Stoner, L. Bergman, J. T. Glass, and R. J. Nemanich, J. Appl. Phys. **69**, 6400 (1991).
5. K. F. Turner, Y. M. LeGrice, B. R. Stoner, J. T. Glass, and R. J. Nemanich, J. Vac. Sci. Technol. B. **9**, 914 (1991).
6. T. P. Humphreys, J. V. LaBrasca, R. J. Nemanich, K. Das, and J. B. Posthill, Jpn. J. Appl. Phys., Pt. 2 **30**, 1409 (1991).
7. T. Tsuno, T. Imai, Y. Nishibayashi, N. Fujimori, and K. Hamada, Jpn. J. Appl. Phys., Pt. 1, **30**, 1063 (1991).
8. M. P. Everson, and M. A. Tamor, J. Vac. Sci. Technol., B. **9**, 1570 (1991).
9. H. G. Busmann, and H. Sprang, I. V. Hertel, W. Zimmermann-Edling, H. J. Guentherodt, Appl. Phys. Lett. **59**, 295 (1991).
10. J. A. Martin, L. Vazquez, P. Bernard, F. Comin, and S. Ferrer, Appl. Phys. Lett **57**, 1742 (1990).
11. C. B. Collins,F. Devanloo, D.R. Jander, T.J. Lee, H. Park, and J.H. You, J. Appl. Phys. **69**, 7862 (1991).
12. S. Ferrer, F. Comin, J. A. Martin, L. Vazquez, and P. Bernard, Surf. Sci. **251/252**, 960 (1991).
13. C. B. Collins, F. Davanloo, E. M. Juengerman, D. R. Jander, and T. J. Lee, Surf. Coat. Technol. **47**, 754 (1991).
14. N. H. Cho, D. K.Veirs, J. W. Ager III, M. D. Rubin, C. B. Hopper, and D. B. Bogy, J. Appl. Phys **71**, 2243 (1992).
15. A.T. Collins, M. Kamo, and Y. Sato, J. Mater. Res. **5**, 2507 (1990).
16. J. A. Freitas, Jr., J. E. Butler, and U. Strom, J. Mater. Res. **5**, 2503 (1990).
17. G. S. Gildenblat, S. A. Grot, C. W. Hatfield, A. R. Badzian, and T. Badzian, IEEE Elect. Dev. Lett. **11**, 371 (1990).
18. K. L. Moazed, R. Nguyen, and J. R. Zeidler, IEEE Elect. Dev. Lett. **9**, 350 (1988).
19. H. Shiomi, H. Nakahata, T. Imai, Y. Nishibayashi, and N. Fujimori, Appl. Phys. (part I) **28**, 758 (1989).
20. J. W. Glesener, and A. A. Morrish, K. A. Snail, J. Appl. Phys. **70**, 5144 (1991).
21. K. L. Moazed, J. R. Zeidler, and M. J. Taylor, J. Appl. Phys. **68**, 2246 (1990).
22. M. C. Hicks, et al., J. Appl. Phys. **65**, 2139 (1989).
23. F. J. Himpsel, P. Heimann, D. E. Eastman, Solid State Comm. **36**, 631 (1980).

24. J. van der Weide and R. J. Nemanich, *Proceedings of the First International Conference on the Applications of Diamond Films and Related Materials*, edited by Y. Tzeng, M. Yoshikawa, M. Murakawa and A. Feldman. (Elsevier, New York, 1991), p.359.
25. T. Tachibana, B.E. Williams, and J.T. Glass, Phys. Rev. B, (in press).
26. B.B. Pate, M.H. Hecht, C. Binns, I Lindau, and W.E. Spicer, J. Vac. Sci. Technol. **21**, 364 (1982).
27. E.H. Rhoderick, and R.H. Williams, Metal-Semiconductor Contacts, (Clarendon press, Oxford, 1988).

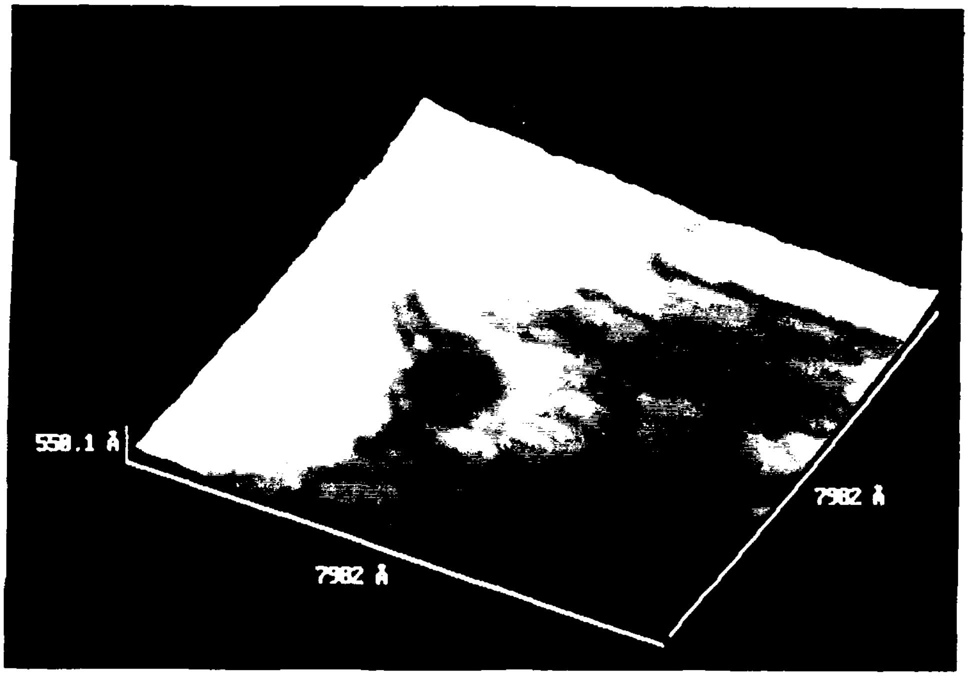

Figure 1 STM micrograph of the scratched Si surface after 60 minute exposure to plasma growth conditions. Scratches can be seen on the substrate which have been used to increase the nucleation density. The roughness of this sample provides evidence of plasma induced surface modification preceeding diamond nucleation.

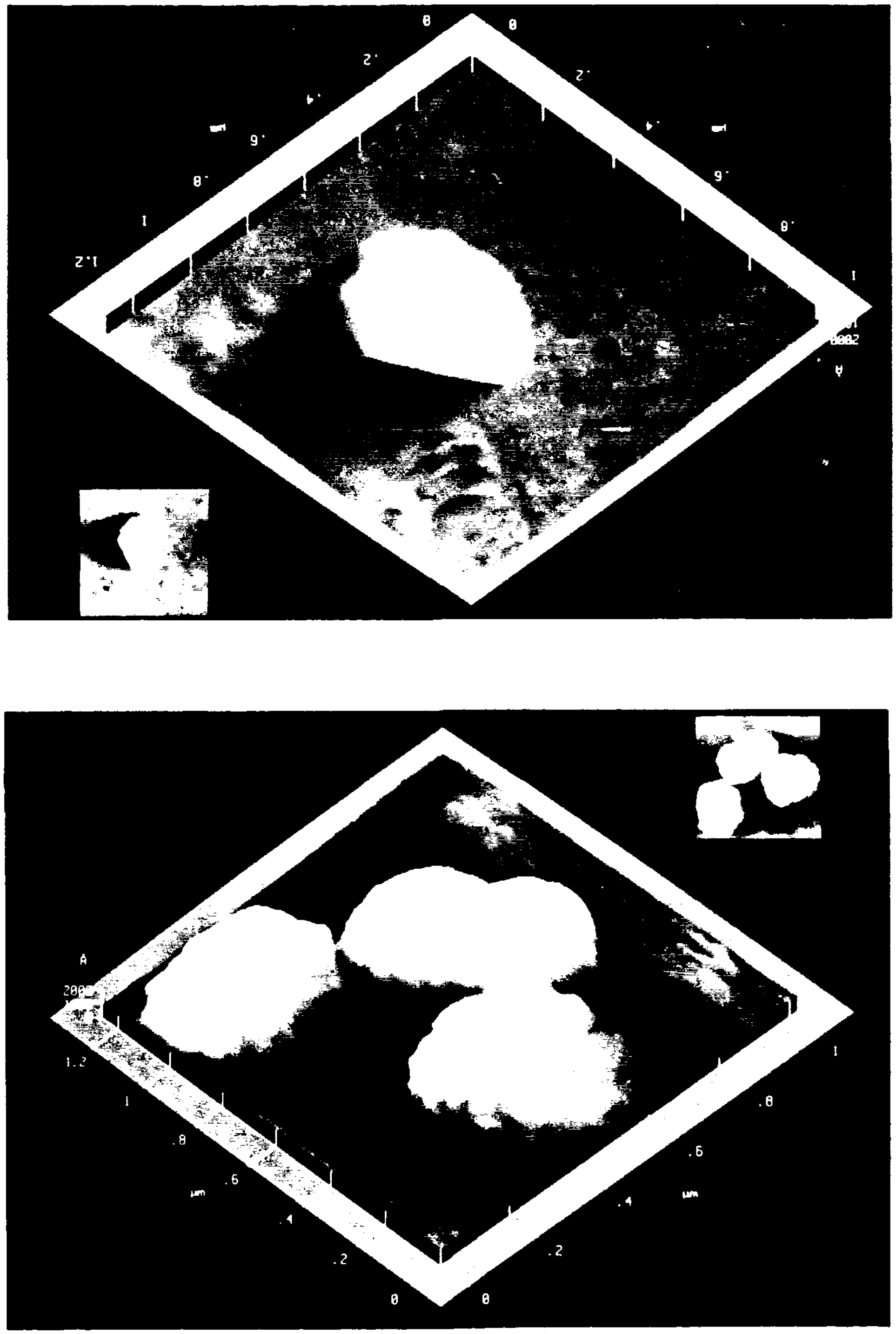

Figure 2 STM images of diamond nuclei on Si. The upper STM micrograph shows a nucleus of diamond grown on silicon that is exhibiting a flat surface nearly parallel to the substrate. The lower micrograph shows several nuclei that are growing 3-dimensionally. Both types of nuclei were found on the same silicon substrate after 1 hour of deposition.

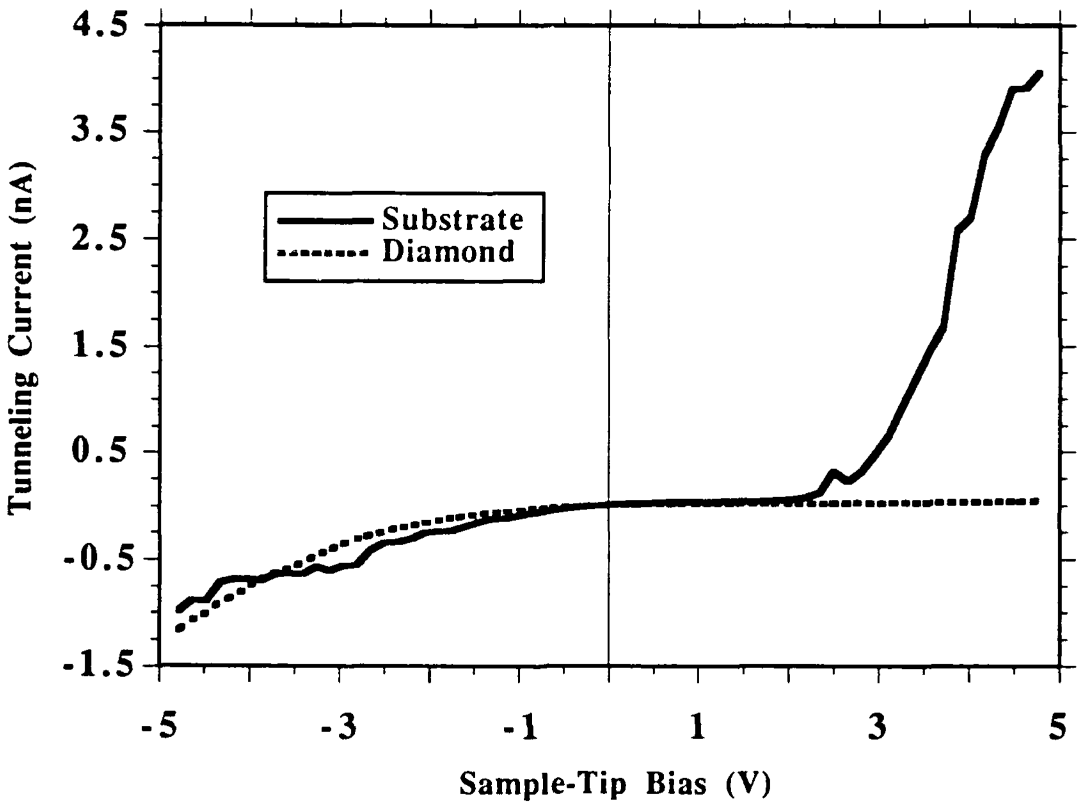

Figure 3 A comparison of the scanning tunneling spectroscopy current-voltage characteristics of a diamond nucleus and areas of the substrate near the nucleus.

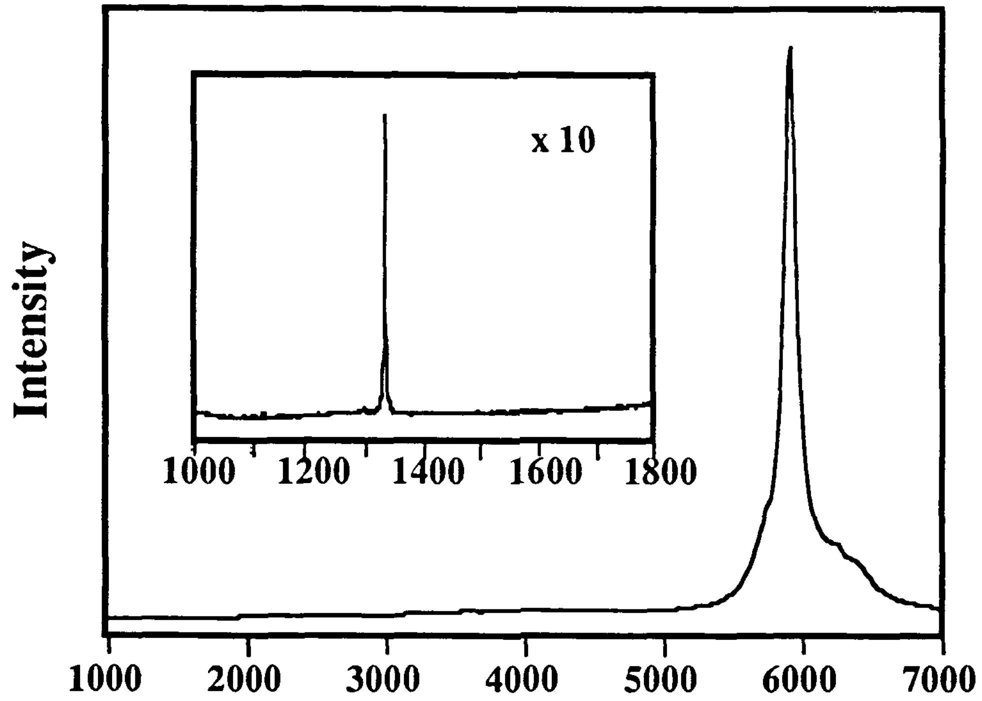

Figure 4 The Raman/photoluminescence spectrum of CVD diamond after 7 hours of growth. The spectrum was excited with 514.5 nm Ar ion laser light. The spectrum is domainated by the 1.68 eV photoluminescence center for a CVD diamond, and the inset shows an expanded higher resolution scan over the region of the diamond-sp2 Raman peaks. At this growth time, the emission from the 1.68 eV PL center showed a maximum relative to the intensity of the diamond Raman.

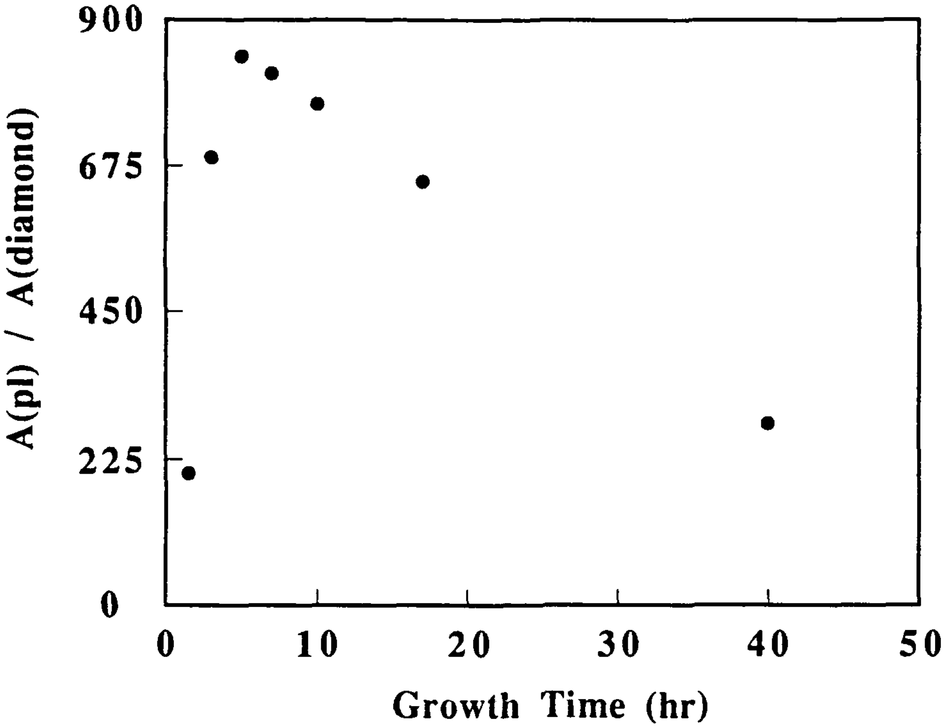

Figure 5 The integrated intensity of the 1.68 eV PL center relative to the diamond Raman peak as a function of deposition time. A maximum is observed after ~7 hours of growth.

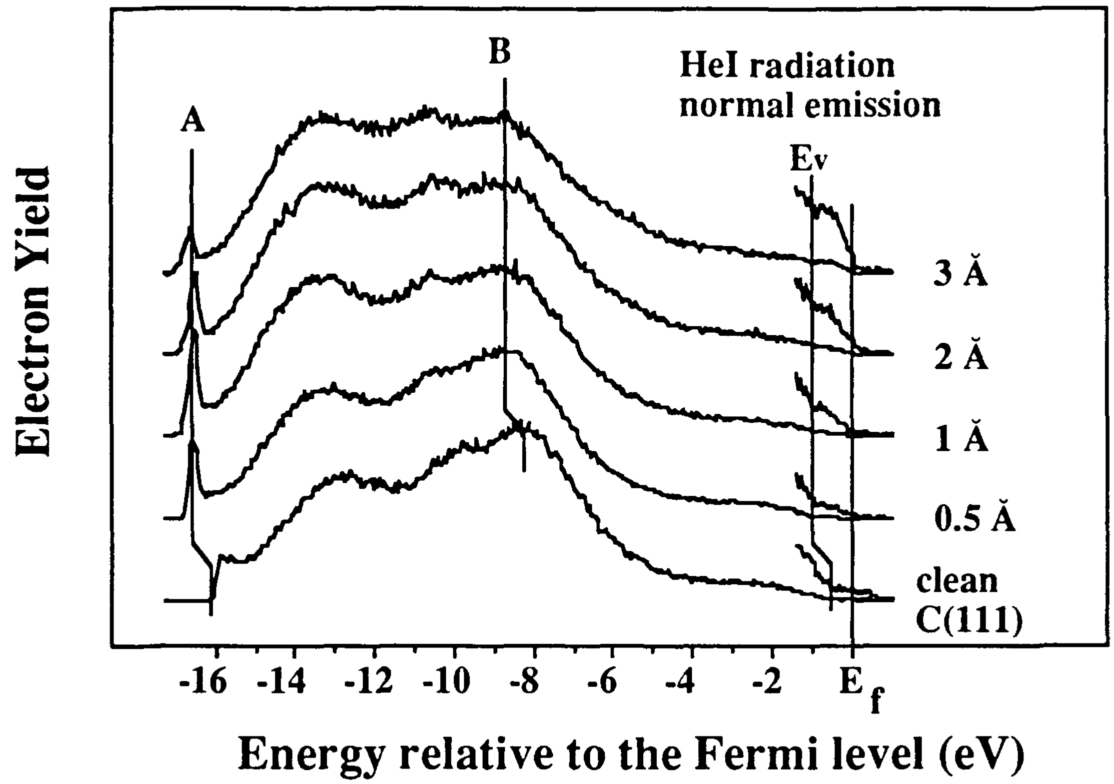

Figure 6. ARUPS spectra of titanium on diamond (111) for increasing titanium thicknesses. After the first deposition the spectrum shifts 0.5 eV toward lower energies and a sharp peak (A), indicative of a negative electron affinity, develops at the low energy cutoff. For increasing titanium thicknesses a Fermi level edge (Ef) develops, while at the same time the position of the valence band edge (Ev) becomes harder to locate. The Schottky barrier height is the energy difference between Ev and Ef

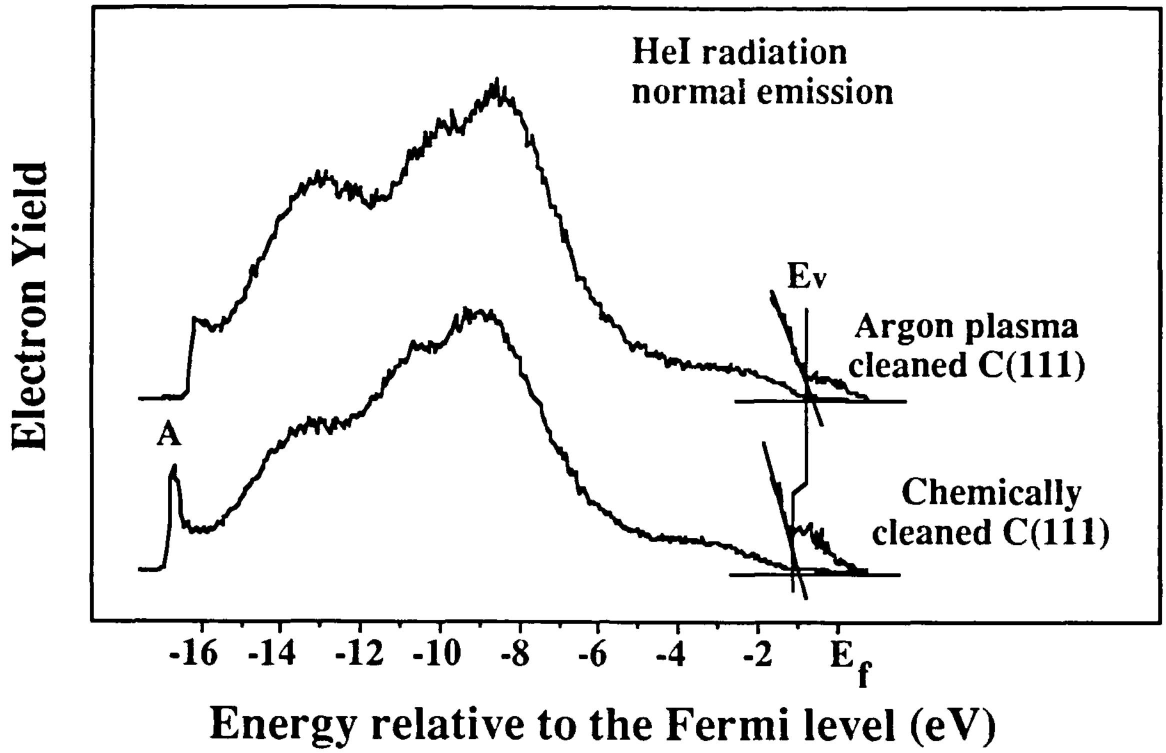

Figure 7. ARUPS spectra of diamond (111) before and after argon plasma cleaning. The spectrum shifts by 0.5 eV towards higher energies while the negative electron affinity peak (A) is significantly reduced after the argon plasma cleaning. The latter effect is attributed to the removal of hydrogen from the surface. The valence band edge is determined by linearly extrapolating the onset of emission down to zero.

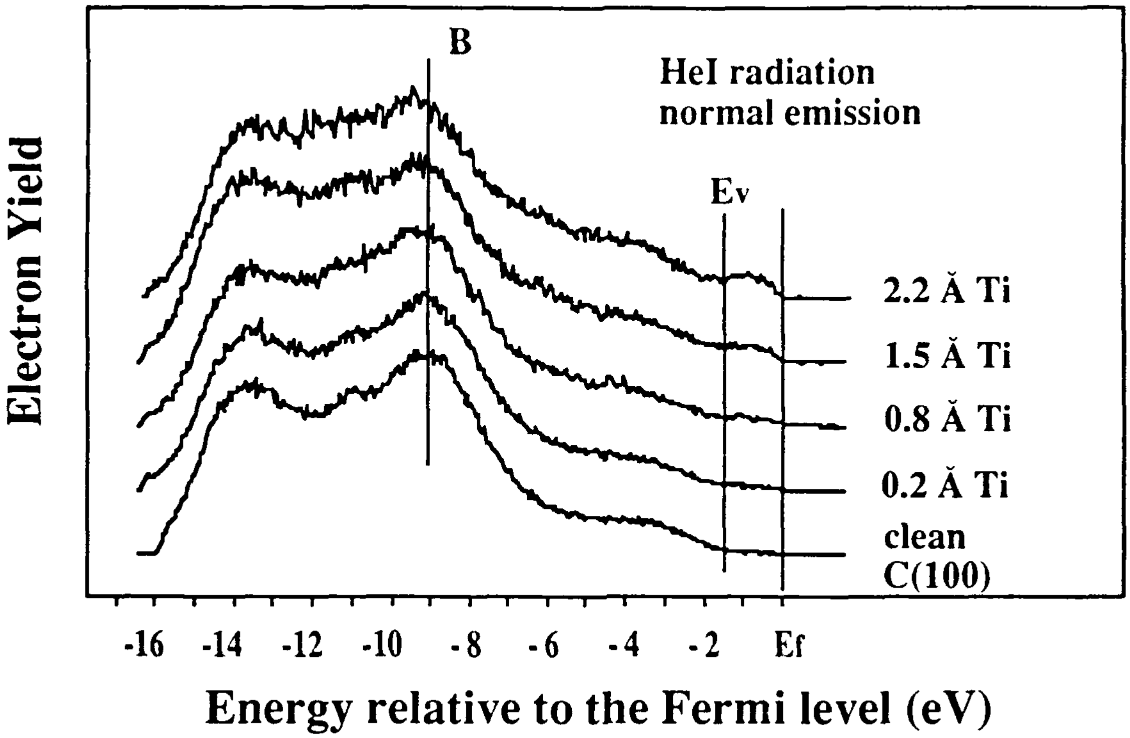

Figure 8. ARUPS spectra of titanium on diamond (100) for increasing titanium thicknesses. The position of Ev relative to peak B is determined from the clean surface and is found to be 8.0 eV. The Fermi level is found from the metal covered diamond (100) and lies 9.4eV above peak B, resulting in a Schottky barrier height of 1.5±0.2 eV.

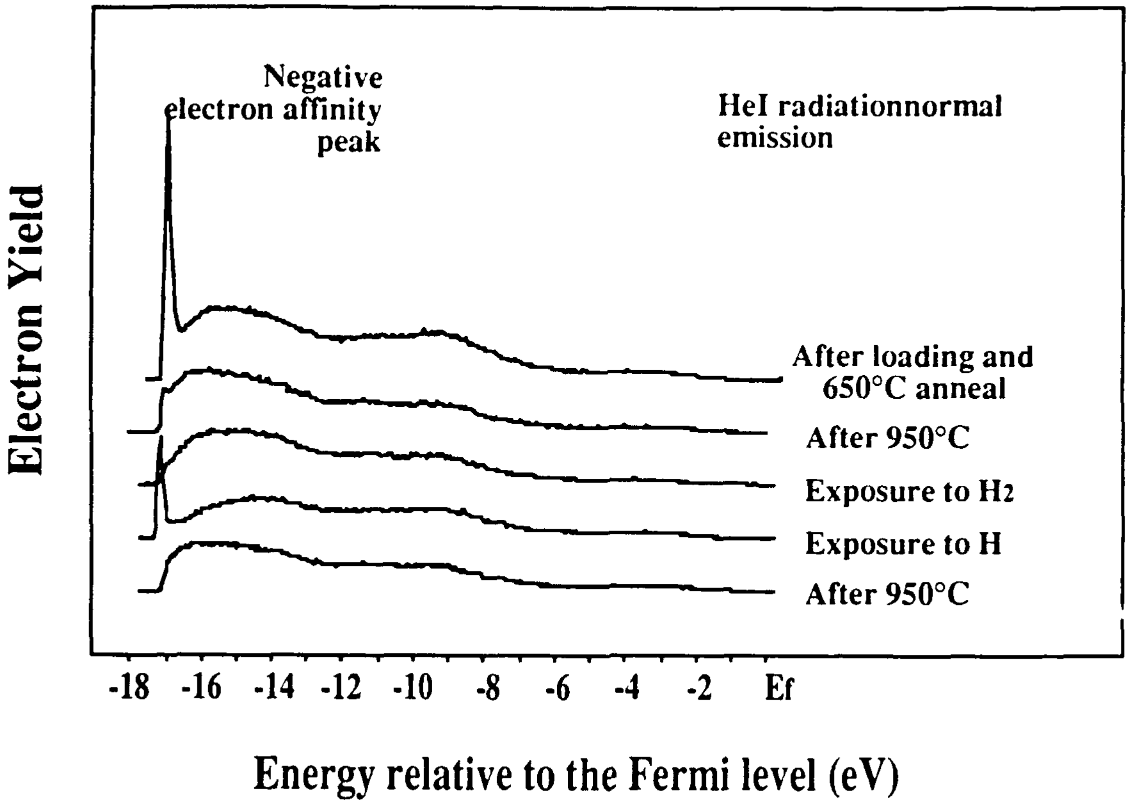

Figure 9 ARUPS spectra of diamond (111). The as loaded spectrum (top) shows the presence of a sharp peak at the lowest energy indicating a negative electron affinity. After a 950°C anneal the peak is gone, indicating the absence of a negative electron affinity. No significant changes occur after exposure to molecular hydrogen for 5 minutes at 10^{-6} Torr. After exposure to mono-atomic hydrogen however the negative electron affinity returns. The bottom spectrum, after another 950°C anneal, shows that the cycle can be repeated.

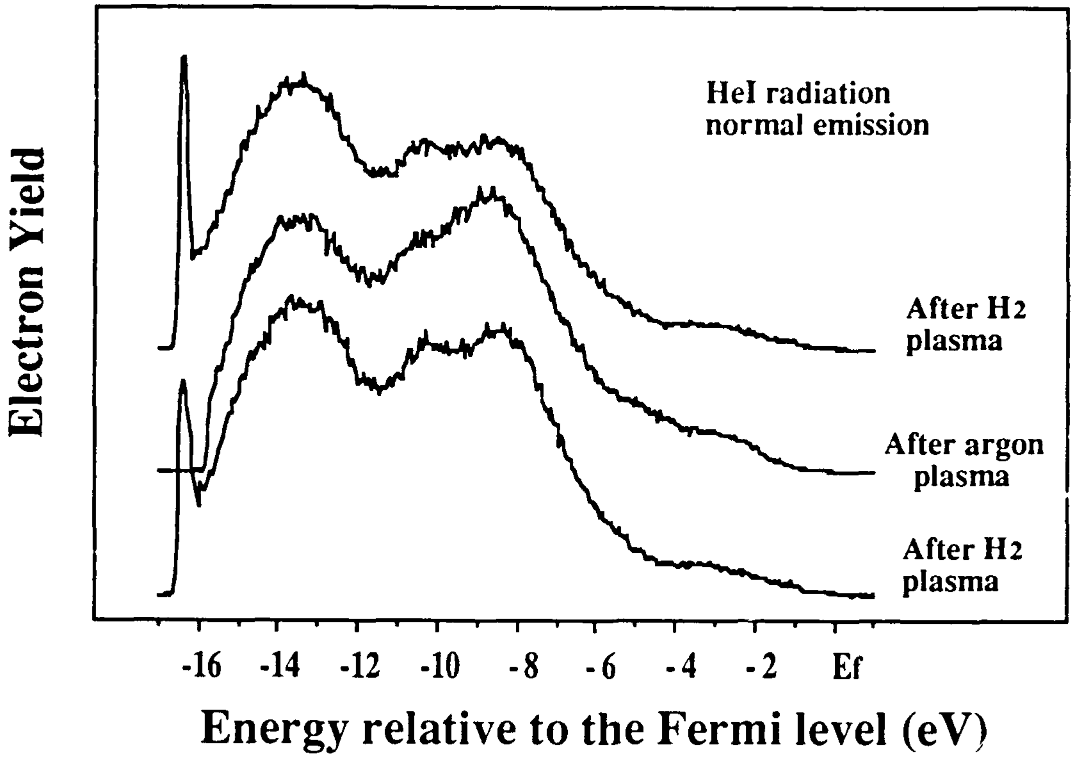

Figure 10. ARUPS spectra of diamond (111) after exposure to: from bottom to top, an hydrogen plasma, an argon plasma and a hydrogen plasma. The diamond was heated to approximately 350°C during each exposure. The spectrum after the first hydrogen plasma shows a sharp peak, due to the negative electron affinity of the surface. In the second spectrum, after argon plasma exposure, the peak is absent, indicating a positive or zero electron affinity. In the third spectrum the negative electron affinity is seen to reappear, after exposure to another hydrogen plasma.

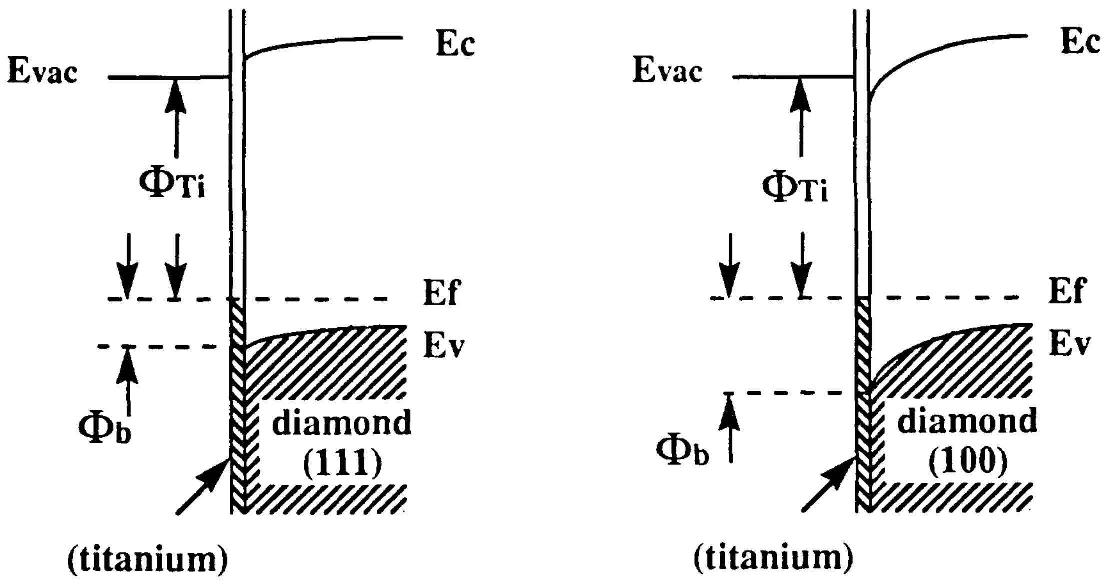

(a) (b)

Figure 11. Model for the titanium induced negative electron affinity on diamond (111). In (a) the sum of the work function of the titanium (Φ_{Ti}) and the Schottky barrier height of titanium on the diamond (111) surface (Φ_{Ti}) is less then the bandgap of the diamond. This lowers the effective work function of the surface such that the conduction band minimum is above the vacuum level, thus resulting in a negative electron affinity. For the diamond (100) surface (b), however, the Schottky barrier height with the titanium is larger than the Schottky barrier height on the diamond (111) surface, and the sum of the Schottky barrier height and the work function of titanium is more than the bandgap of the diamond, resulting in a positive electron affinity.

IV. Diamond Synthesis Using the Oxy-acetylene Torch Method

I. Introduction

The exceptional properties of semiconducting diamond make it an ideal candidate for electronic devices to be used in extreme environments. These properties include a large band gap (5.48 eV) and an exceptional electrical properties at high temperatures [1]. Recently, several working diamond devices have been fabricated [2, 3], however, more efficient growth techniques of synthetic diamond must be investigated so that diamond becomes a realistic alternative to conventional semiconducting materials. Ideally, to achieve that goal, two-dimensional growth of smooth diamond films must be obtained with properties better than that of natural semiconducting diamond. Several methods are currently used to grow diamond thin films, the oxy-acetylene torch being the most recent discovery as a deposition technique [4]. Its fast growth rate and low set up cost make it an attractive alternative to many conventional CVD systems.

II. Experimental Procedure

The basic combustion flame system consists of a standard welding torch with a #2 tip. The gas flow of both the oxygen and the acetylene is controlled through a MKS 4-channel mass flow controller (MFC). A two-color optical pyrometer (Williamson 8220), with a range from 500°C to 1100°C, monitors the temperature of the substrate. The system has been additionally modified to improve the control of both the gas ratios and the temperature. To do this both the MFC and the pyrometer were interfaced to a personal computer via a Keithley / Metrabyte DASCON1 DAC / ADC board. The substrate temperature was regulated by a Eurotherm PID controller which monitored the water flow through the copper stage, a signal from the pyrometer is utilized as feedback to the PID controller. Finally, to minimize the deviation from the temperature setpoint, integral heaters were added allowing an accuracy with a variation of plus or minus ten degrees. A schematic of the system is given in Figure 1. A QuickBasic program was written so that gas flow and temperature are monitored continuously. Additionally, this program allows complex gas flow profiles to be programmed so that the flame chemistry can be continuously modified throughout the nucleation and growth of the diamond film. This process is termed here as gas ratio cycling. Three types of substrates were utilized for the experiments: pristine silicon (scratched with 1μm diamond paste immediately prior to growth to enhance nucleation), silicon that had been seeded with diamond particles (termed as a mosaic substrate) [5] and a substrate with CVD grown oriented diamond on top [6].

The diamond films were characterized by Raman spectroscopy and scanning electron microscopy (SEM) and electrical resistivity measurements were performed on selected samples to compare with natural type IIa diamond.

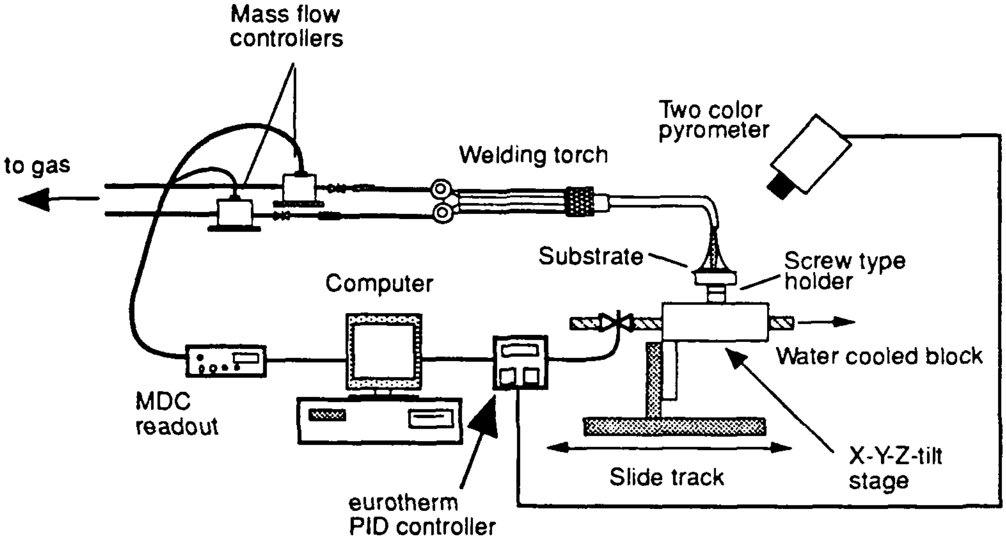

Figure 1. Schematic of the combustion system used in these experiments.

III. Results

To test the feasibility of the system, several experiments were designed involving both temperature variations and gas ratio changes. The first experiment tested the accuracy of the PID controller by growing at several temperatures for 10 minutes. A plot of this temperature ramp is shown in Figure 2. The deviation from the set point was minimal and transition from one temperature to the next was smooth.

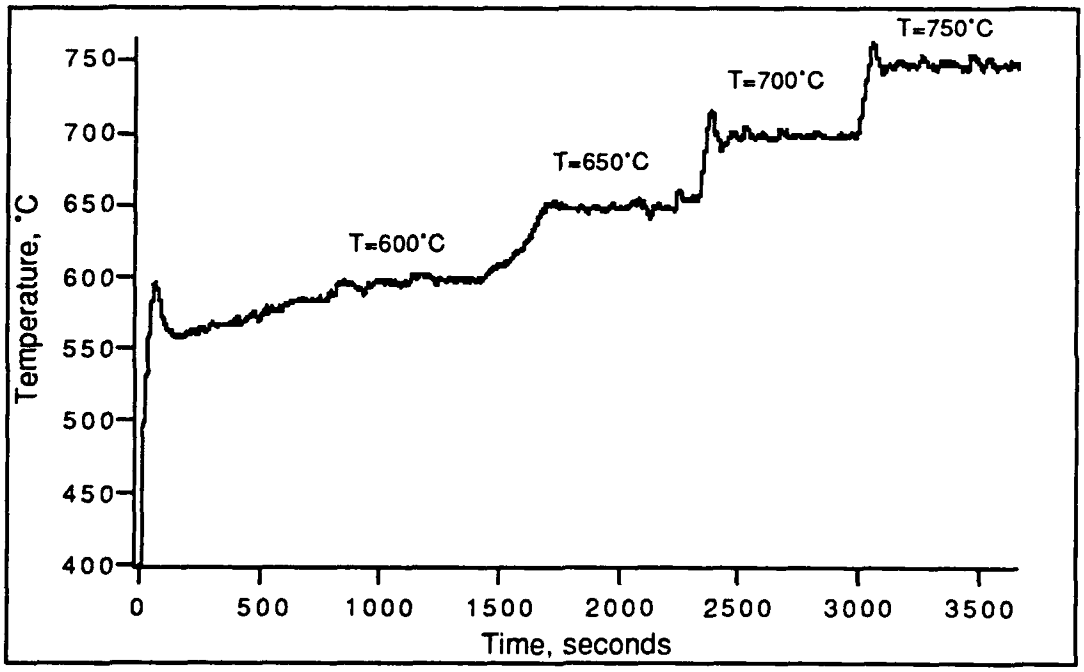

Figure 2. Temperature ramp from 600°C to 750°C.

The second experiment involved a combination of gas ratio cycling and temperature ramping. In other words, the gas ratio was varied and the temperature was simultaneously maintained constant. Several functions such as a step and sinusoidal are available on the software but personalized modification to programs can also be inputted manually before the onset of the growth. The sawtooth function which involved periodically ramping the R_f from 0.97 to 1.01, then repeating over a one minute interval proved effective for these experiments.

Growth of these films occurred in a three step process. A 2 minute pretreatment consisting of a deposition at an oxygen to acetylene ratio of 0.93 and a substrate to flame core distance of approximately 1.5 cm [7] followed by a 10 minute growth at $R_f = 0.97$ and a substrate to flame core distance of 2 mm was effective in forming a stable diamond layer for cycling. Without these initial two steps little or non-uniform growth of diamond occurred with gas ratio cycling. A typical growth and temperature profile is shown in Figure 3. As indicated by the figure, both accurate control of the temperature and the gas ratios was achieved. Comparing the Raman results from a cycled sample to a non-cycled sample (constant ratio growth continuing after the pretreatment), a reduction in the non-diamond component was seen. These spectra were taken from the same part of the sample, between the center and the edge of the circular deposition region. High temperature resistivity results from the same two samples showed a strong similarity to natural type IIa diamond but little difference was seen between the cycled and non-cycled sample, Figure 4. Comparison of these combustion samples to a typical microwave plasma grown sample showed a better quality and the combustion samples did not the high conductivity before heating that microwave samples have.

These results were then applied to the growth on the mosaic and CVD grown oriented diamond on silicon. A pretreatment, consisting of 15 seconds in an oxygen rich flame, $R_f = 1.05$, proved to be effective in oxidizing the visible silicon and cleaning the diamond by employing a short oxygen etch. Following this step the gas ratio cycling was started as described above. After 4-6 hours of growth large (100) facets were observed on the substrates, in several spots the facets had grown together indicating that 2 dimensional growth of diamond was occurring, Figures 5 and 6.

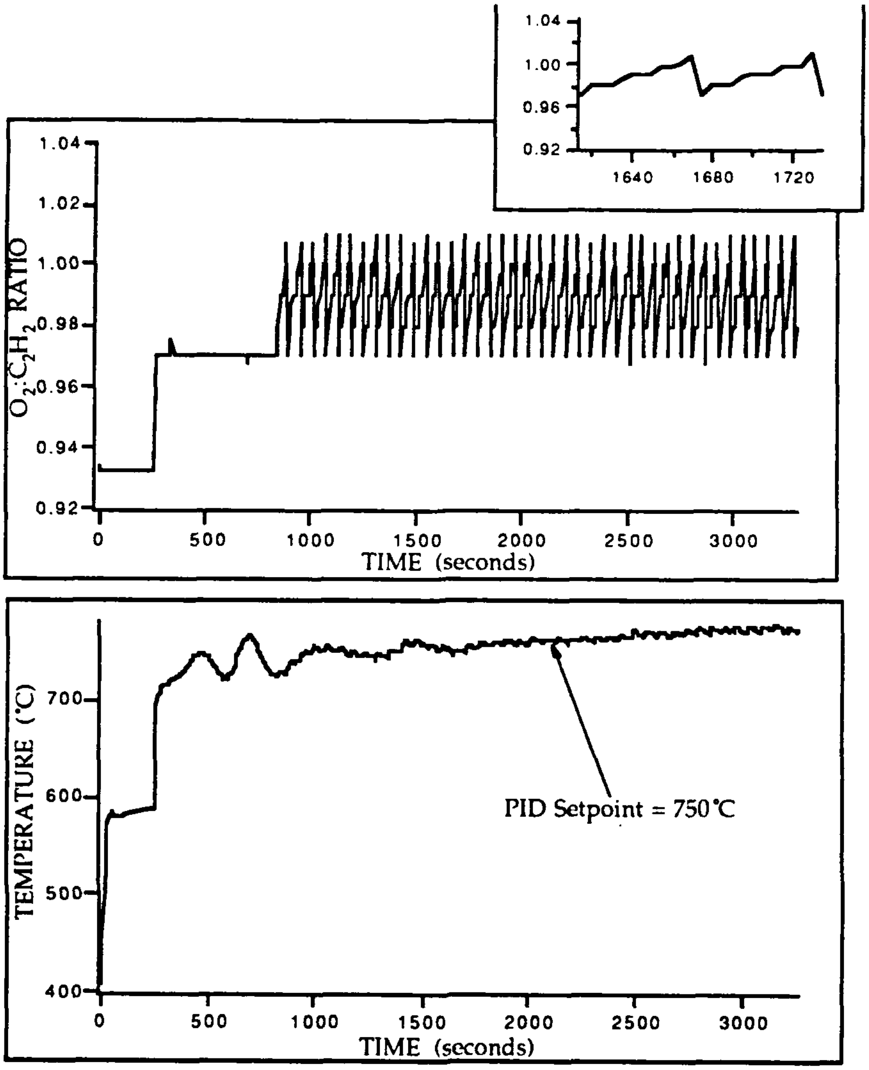

Figure 3. Typical growth and temperature profile from a gas ratio cycled sample.

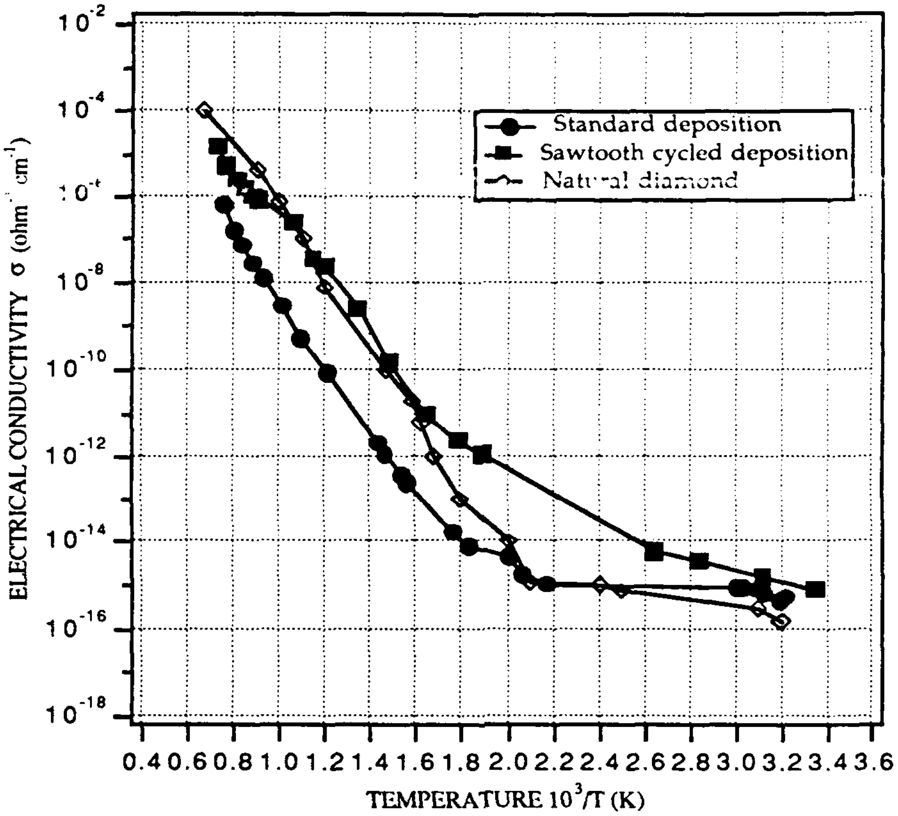

Figure 4. Resistivity results from a cycled and constant ratio grown diamond, compared with natural diamond.

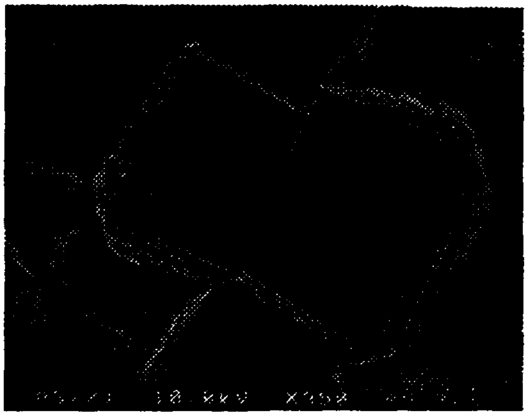

Figure 5. Diamond grown on a mosaic substrate.

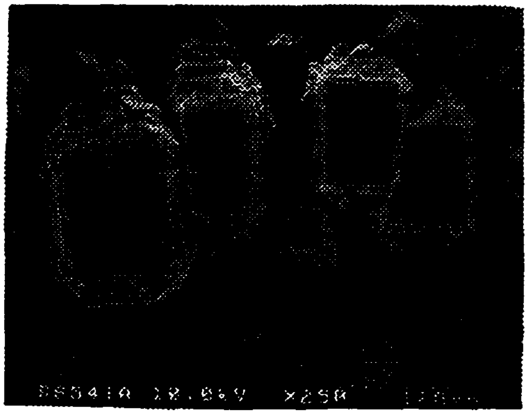

Figure 6. Diamond grown on CVD diamond oriented substrate.

IV. Discussion

As shown above the Raman results indicated that there was a reduction in the non-diamond component by the reduction in the broad peak at about 1510 cm^{-1}. This can be attributed to a process of growth and etching that appears to be occurring during the gas ratio cycling. At lower ratios growth of diamond dominates, while simultaneously a non-diamond component is also deposited. However, as the oxygen content increases in the flame an etching of the unfavorable component occurs creating higher quality diamond.

Resistivity results showed that as grown combustion diamond as grown is comparable to natural type IIa diamond. These results can be attributed to the absence of a significant nondiamond component and the natural inclusion of nitrogen from the atmosphere into the diamond [8], making its qualities similar to that of the natural diamond [9, 10] which also contains diamond impurities. This would explain the strong similarity that both the cycled and non-cycled sample had to natural diamond.

V. Conclusions

Using a modified oxy-acetylene torch system growth of high quality diamond has been achieved. A personal computer interfaced with the MFCs and PID controller has allowed accurate control of both the substrate temperature and the gas ratios. Additionally, periodic variations are easily programmed allowing precise control of gas ratio cycling. Two-dimensional homoepitaxial growth on seeded and oriented substrates has also been achieved using the system described above, thus allowing a benchmark of the potential conditions for two-dimensional growth.

VI. Future Research Plans/Goals

With these initial results, several immediate steps will be pursued. Additional modifications to the system are planned such as an improved stage design and narrowing the temperature deviation from the setpoint. Proper cycling conditions will be investigated in order to improve the quality of the diamond more and also to achieve a better understanding of the mechanisms occurring during gas ratio cycling. A combination of both temperature and gas ratio cycling will be investigated to improve the homoepitaxial two-dimensional growth that earlier results have shown are possible. Finally, experiments to improve the two-dimensionality on nondiamond substrates will be investigated.

VII. Acknowledgements

The author would like to thank the following people and organizations. J. Vandersande and D. Zolten for the electrical measurements, Kobe Steel U.S.A. for the use of the SEM, R. Nemanich, and especially A. Somashekar, S. Trent, and J. von Windheim for their help in compiling this report.

VIII. References

1. J. E. Field, *The Properties of Diamond* (Academic Press Limited, San Diego, 1976)
2. M. W. Geiss, D. D. Rathman, J. J. Zayhowski, D. Smyth, D. K. Smith and G. A. Ditmer, *3rd ONR Diamond Technology Initiative Symp Abs.*, Crystal City, VA 115-118 (1988)
3. G. Gildenblat, S. A. Grot C. R. Wronski, A. R. Badzian T. Badzian and T. Messier, Appl. Phys Lett. **53**, 586-588 (1988).
4. Y. Hirose and N. Kondo, *Proceedings fo the 1988 Spring Meeting of Japan Applied Physics Society*, Japan Applied Physics Society, Tokyo, Japan, 1988, 434.
5. M. W.Geiss, et al., Appl. Phy. Lett. **58**(22), 2485-2487 (1991)
6. B. R. Stoner and J. T. Glass, Appl. Phys. Lett. **60** (6), 698-700 (1992).
7. M. T. McClure, J. A. von Windheim, J. T. Glass and J. T. Prater in *Novel Forms of Carbon*, edited by C. L. Renschler, J. J. Pouch and D. M. Cox (Mater. Res. Soc. Proc. 270, Pittsburg, PA 1992) pp.323-328
8. Y. Matsui, A. Yuki, M. Sahara, Y. Hirose, Jpn. J. Appl. Phy., **28** (9), 1718-1724 (1989)
9. J. E. Field, *The Properties of Diamond_* (Academic Press Limited, San Diego, 1976)
10. A. T. Collins, Semicond. Sci. Technol. **4**, 605-611 (1989)

V. Gas-Source Molecular Beam Epitaxy of Monocrystalline Beta-SiC on Vicinal Alpha(6H)-SiC

A Communication
Submitted for Consideration for Publication
to
The Journal of Materials Research

By

L. B. Rowland*, S. Tanaka, R. S. Kern and Robert F. Davis
Department of Materials Science and Engineering
North Carolina State University
Box 7907
Raleigh, North Carolina 27695-7907

November, 1992

ABSTRACT

Single-crystal epitaxial films of cubic β(3C)-SiC(111) have been deposited on hexagonal α(6H)-SiC(0001) substrates oriented 3-4° towards $[11\bar{2}0]$ at 1050-1250°C via gas-source molecular beam epitaxy using disilane (Si_2H_6) and ethylene (C_2H_4). High resolution transmission electron microscopy revealed that the nucleation and growth of the β(3C)-SiC regions occurred primarily on terraces between closely spaced steps because of reduced rates of surface migration at the low growth temperatures. Double positioning boundaries were observed at the intersections of these regions.

---

*Present Address
Naval Research Laboratory, Code 6861
4555 Overlook Av., SW
Washington, DC 20375-5320

Polytypes are special one-dimensional polymorphs which differ only in the stacking sequence along the closest-packed direction. Silicon carbide occurs in one cubic (zincblende) polytype referred to as 3C- or β-SiC, where the 3 refers to the number of planes in the periodic sequence. The hexagonal (wurtzite) polytype also exists in this material. Both polytypes occur in more complex, intermixed forms yielding a wider range of ordered, larger period, hexagonal or rhombohedral structures of which 6H is the most common. All of these noncubic polytypes are known collectively as α-SiC.

The growth of 3C- and 6H-SiC thin films has been achieved primarily via chemical vapor deposition (CVD) (see Ref. #1 for a review of this research). Monocrystalline Si(100) wafers have been the principal substrate of choice for the deposition of 3C. It is now a common first step to transform the surface region of these wafers to β-SiC by reaction with a C-containing gas to reduce the effects of the large mismatches in lattice parameters ($\approx$20%) and coefficients of thermal expansion ($\approx$10%). The epitaxial growth of SiC films on α(6H)-SiC(0001) substrates via CVD has been reported for three decades[1]. Single phase β-SiC films result[2,3] when the [0001] direction of the 6H wafer is oriented off-axis $\leq 1°$. The primary defects in these films are double positioning boundaries (DPB)[4]. The use of vicinal 6H-SiC(0001) substrates cut 3-4° towards $[11\bar{2}0]$ have resulted in high-quality monocrystalline 6H-SiC layers with low defect densities[5,6], including the absence of DPBs.

Solid- and gas-source (GS) molecular beam epitaxy (MBE) techniques have also been employed for deposition of SiC films[7,8]. Kaneda et al.[7] used on-axis α(6H)-SiC{0001} substrates and electron-beam evaporated Si and C sources. Epitaxial 3C-SiC(111) films were obtained at particular Si-to-C flux ratios in the temperature range of 1150-1400°C, as determined by reflection high-energy electron diffraction (RHEED). No information was given by these authors regarding either the microstructure or the type of defects present in these films. By contrast, Yoshinobu et al.[8] employed the periodic introduction of Si_2H_6 and C_2H_2 to achieve 3C-SiC growth on vicinal 6H-SiC$(000\bar{1})$ and 6H-SiC$(01\bar{1}4)$ substrates at 850-1160°C. Films grown on vicinal 6H-SiC $(000\bar{1})$ contained DPBs while those grown on 6H-SiC $(01\bar{1}4)$ were free of these defects. Smooth films were obtained at the lowest growth rates used in the study (< 0.01 μm/hr).

In the present research, the 3C-SiC films were grown via GSMBE between 1050 and 1250°C on α(6H)-SiC(0001) wafers oriented 3-4° off [0001] towards $[11\bar{2}0]$ and produced by Cree Research, Inc.using a seeded Lely sublimation method. The MBE growth system has been described previously[9]. Each wafer was sequentially cleaned prior to growth using a 10% HF etch at room temperature for 5 min, rinsed in DI water for 2 min and heated in the MBE chamber for 5 min at the growth temperature to achieve the desorption and decomposition of any remaining hydrocarbon species and native oxide, respectively. The source gases of Si_2H_6

and C_2H_4 were used to deposit the SiC. The base and operating pressures were 10^{-9} torr and 3×10^{-5}-3×10^{-6} torr, respectively.

The surface morphology was determined using field-emission scanning electron microscopy (SEM) at an operating voltage of 2.0 kV. Reflection high-energy electron diffraction (RHEED) at 10 kV and high-resolution transmission electron microscopy (HRTEM) were used for structure and microstructure analyses. Samples were prepared for HRTEM using standard techniques[10]. An Akashi EM 002B high-resolution transmission electron microscope was used at 200 kV for the HRTEM analysis.

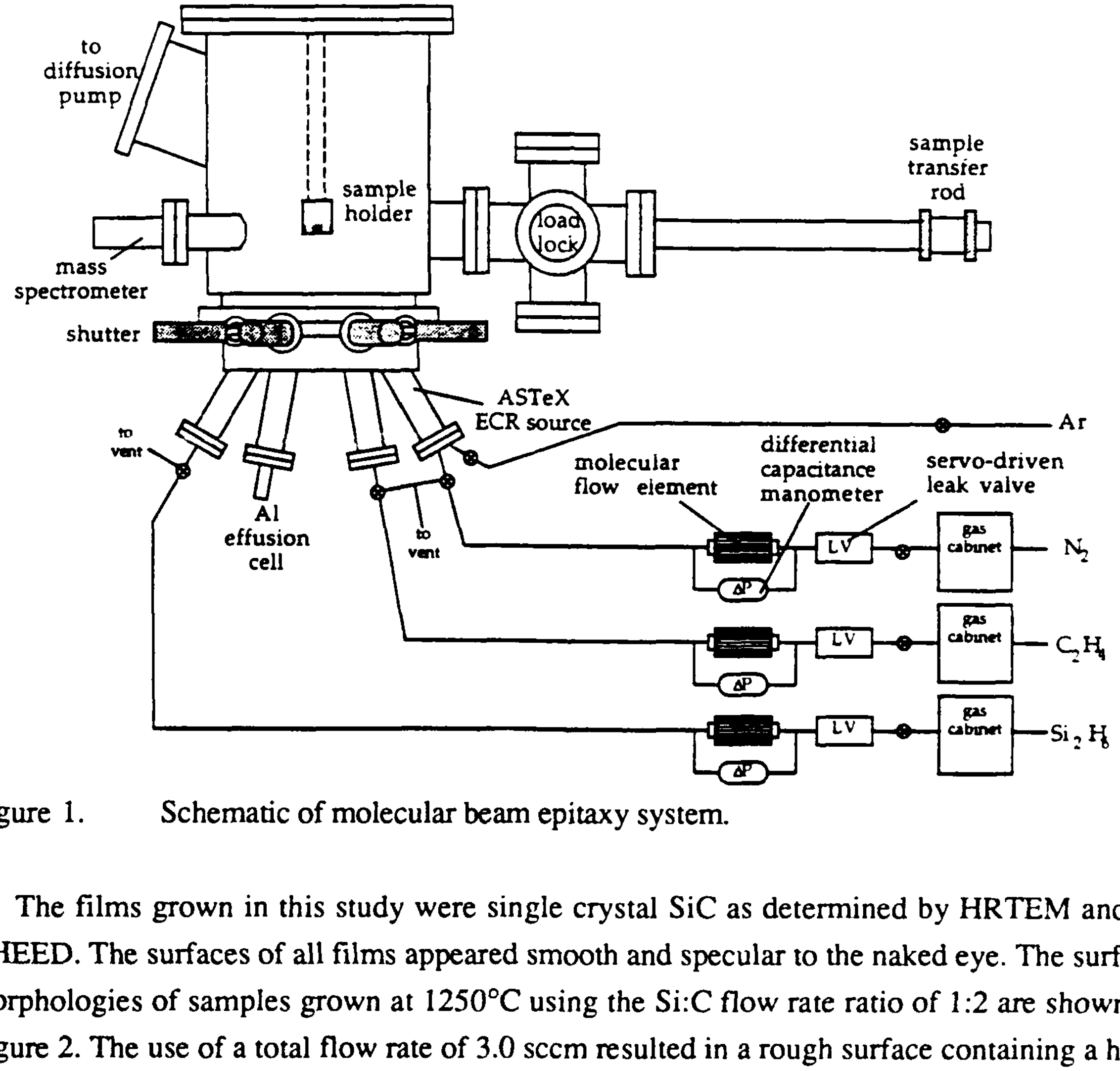

Figure 1. Schematic of molecular beam epitaxy system.

The films grown in this study were single crystal SiC as determined by HRTEM and/or RHEED. The surfaces of all films appeared smooth and specular to the naked eye. The surface morphologies of samples grown at 1250°C using the Si:C flow rate ratio of 1:2 are shown in Figure 2. The use of a total flow rate of 3.0 sccm resulted in a rough surface containing a high density of small (0.1-0.2 µm) triangular regions of different heights, as shown in Figure 2(a). Reducing the total flow rate to 1.5 sccm produced a smoother top surface with regions of uniform height, as shown in Fig. 2(b). Further reduction to 0.30 sccm resulted in a significantly smoother surface with fewer, smaller regions (Figure 2(c)). The use of 0.06 sccm did not result in growth, as determined by HRTEM analysis.

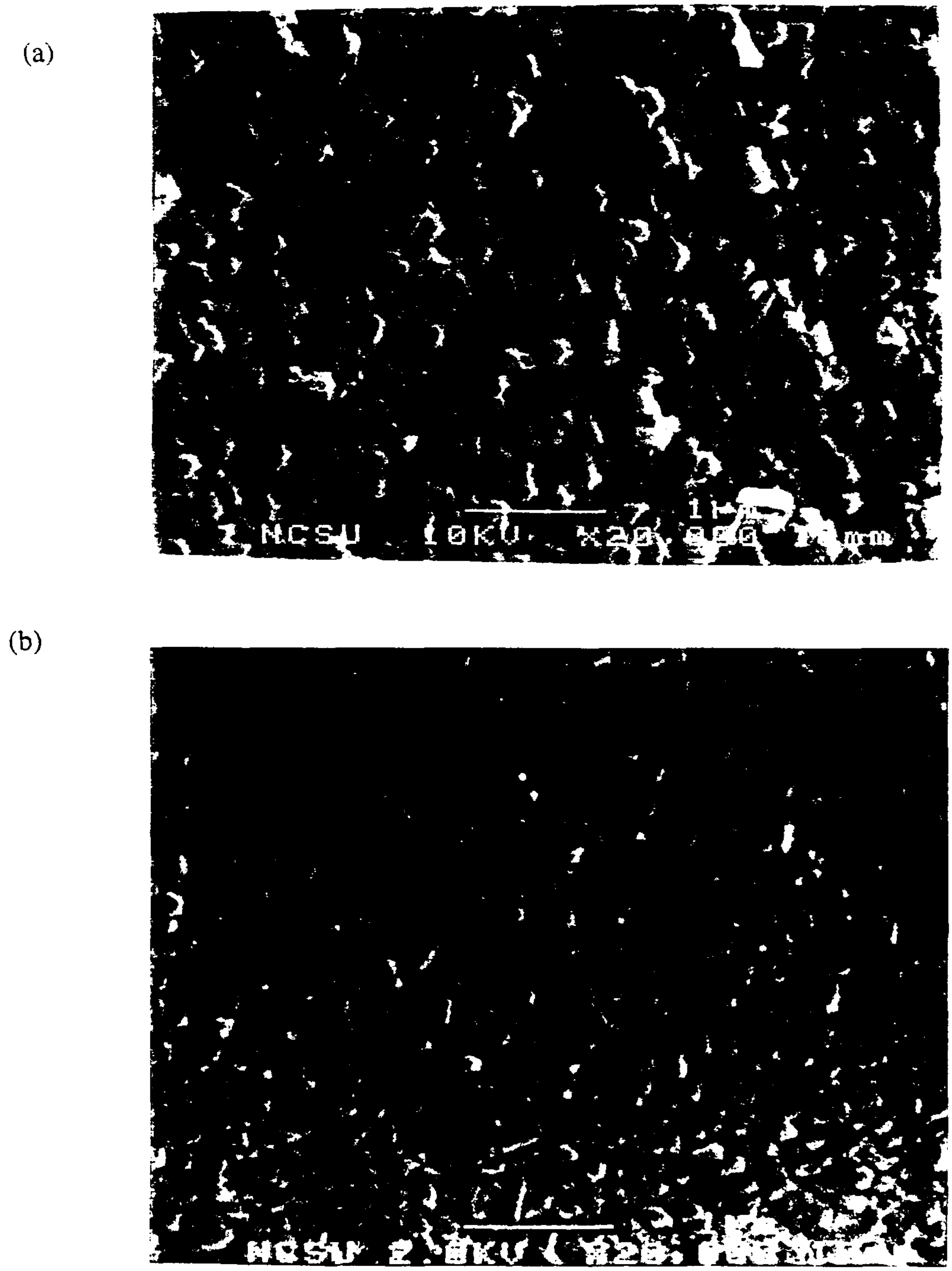

Figure 2. Scanning electron micrograph of the surface of 3C-SiC films grown on 3-4° off-axis 6H-SiC substrates at 1250°C using (a) 2.0 sccm C_2H_4 and 1.0 sccm Si_2H_6, (b) 1.0 sccm C_2H_4 and 0.5 sccm Si_2H_6.

Figure 2(c). 0.2 sccm C_2H_4 and 0.1 sccm Si_2H_6.

Figure 3 is a cross-sectional HRTEM micrograph of the SiC film grown at 1250°C using a total flow rate of 1.5 sccm. The substrate is oriented so that the $[11\bar{2}0]$ direction is perpendicular to the plane of the image. The lattice images of the film reveal it to be the β(3C) polytype in the (111) orientation. The micrograph and the corresponding selected-area diffraction pattern also show the epitaxial relationship between the substrate and the film. Stacking faults parallel to the interface can also be observed. Plan-view TEM on this sample (Figure 4) shown that DPBs and stacking faults (denoted SF) are present in this sample. The same results were obtained at all growth temperatures using the C:Si flow rate ratio of 2:1.

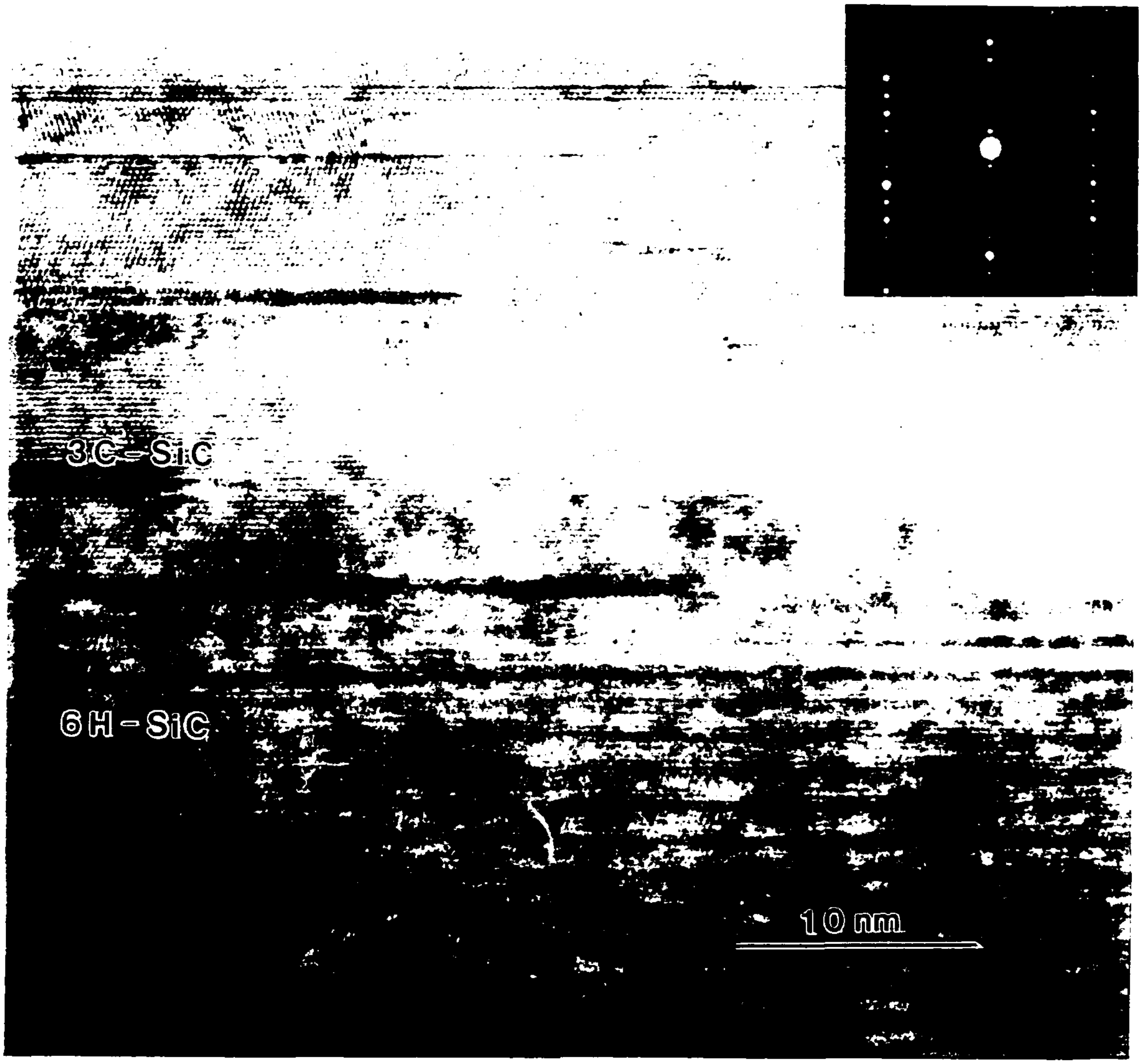

Figure 3. Cross-sectional HRTEM micrograph of 3C-SiC (111) film on vicinal 6H-SiC (0001) substrate with inset of selected area diffraction pattern ([110] zone axis). Sample was grown at 1250°C using 1.0 sccm C_2H_4 and 0.5 sccm Si_2H_6.

Figure 4. Plan-view transmission electron micrograph of 3C-SiC film and 6H-SiC substrate shown in Figure 3. Both stacking faults (denoted SF) and double positioning boundaries (denoted DPB) are visible.

The occurrence of 3C-SiC on vicinal α(6H)-SiC substrates is in contrast to the 6H films obtained by CVD, where step separation clearly defines the stacking sequence of the resulting films[5,6]. It was initially believed that a decrease in total flow rate at the same growth temperature would allow the 6H polytype to form, as the Si and C species would have more time to reach energetically favorable sites associated with steps. However, the 3C polytype formed regardless of the total flow rate. Growth at 1200 and 1050°C under similar conditions also resulted in 3C-SiC.

Films were also grown at 1050°C using the flow rates of 2.0 sccm C_2H_4 and 0.50 sccm Si_2H_6. The decrease in temperature and the high flow rate were used to lower the reactivity and surface mobility and to increase the supply of precursor species, respectively, to enhance the nucleation density. An SEM micrograph of the surface of this film is shown in Figure 5. The film appears much smoother than films grown at higher temperature and/or at lower flow rates. However, individual regions are also observed with diameters of substantially less than 100 nm. The HRTEM microstructure of this film shown in Figure 6 reveals a high density of steps (denoted by arrows) on the substrate surface and regions of 3C-SiC(111) which are entered on the terraces between the steps. Each terrace appears to have one individual region. In most

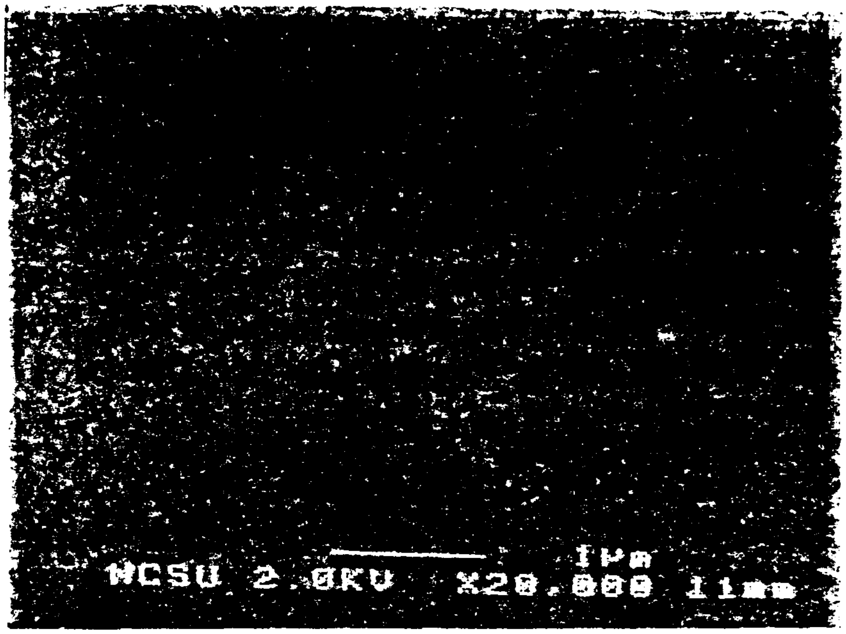

Figure 5. Scanning electron micrograph of surface of 3C-SiC film grown on vicinal 6H-SiC at 1050°C using 2.0 sccm C_2H_4 and 0.5 sccm Si_2H_6.

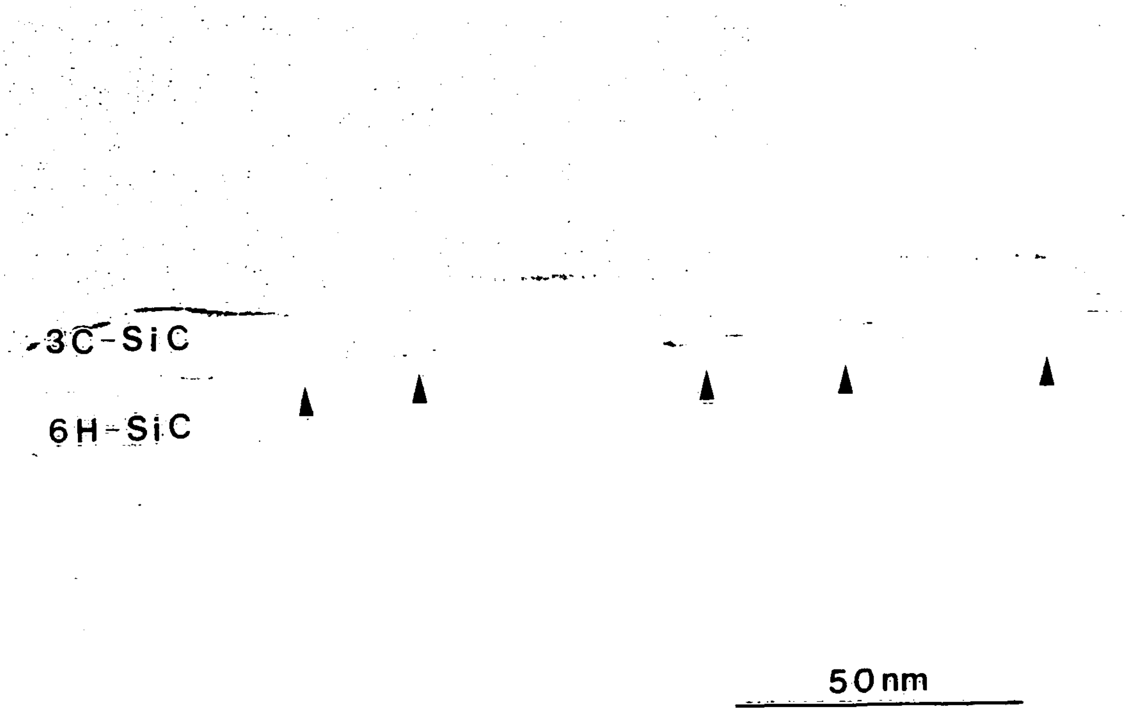

Figure 6. High-resolution TEM micrograph of 3C-SiC regions and vicinal 6H-SiC (0001) substrate. Sample was grown at 1050°C using 2.0 sccm C_2H_4 and 0.5 sccm Si_2H_6. Steps on the 6H-SiC substrate surface are denoted by arrows.

areas, adjacent regions coalesce above the steps. The areas of coalescence were much more defective than the remainder of the film.

The evidence presented in Figure 6 indicates that within the ranges of conditions employed in this study, nucleation on vicinal 6H-SiC substrates occurs on terraces between steps resulting in 3C-SiC(111). In the accepted model, independently proposed by Kong et al.[5] and Kuroda et al.[6], the density and orientation of the surface steps determine the resultant SiC polytype. If few steps are present, as in the case of nominally on-axis SiC, growth conditions determine the resultant polytype and 3C-SiC is usually formed. If there exists a high density of $[11\bar{2}0]$ surface steps, then these steps serve as a template for SiC growth and the stacking sequence of the 6H polytype is preserved. However, in our studies, the kinetics of surface migration are sufficiently decreased as a result of the reduced substrate temperature that β-SiC nucleates on the terraces rather than at the surface steps.

The surface treatment prior to growth also differed between our MBE and the previous CVD studies. These differences may have affected the resultant SiC polytype and the density of defects such as DPBs. Two groups of researchers have observed that variation in surface treatment prior to growth can reduce or virtually eliminate DPBs formed on the resultant film[11,12]. This difference in surface treatment may also cause the resultant polytype to be 3C rather than 6H. Studies concerned with this topic are ongoing in the authors' laboratory.

In summary, monocrystalline films of β(3C)-SiC(111) were grown on 3-4° off-axis α(6H)-SiC(0001) substrates at 1050-1250°C by GSMBE using C_2H_4 and Si_2H_6 at a flow rate ratio of 2:1. High-resolution TEM showed that nucleation and growth occurred on the terraces between closely-spaced substrate steps as a result of the reduction in the kinetics of surface migration of the reactive species relative to that found in CVD processes where α(6H)-SiC is normally deposited.

ACKNOWLEDGEMENTS

The authors acknowledge the support of this research by the Office of Naval Research under Grant #N00014-88-K-0341. We also express our appreciation to Applied Science and Technology, Inc., Woburn, MA for the ECR source, and to Cree Research, Inc., Durham, NC for the vicinal 6H-SiC substrates.

REFERENCES

1. R. F. Davis, J. W. Palmour, and J. A. Edmond, Diamond and Related Materials **1**, 109 (1992).
2. H. S. Kong, J. T. Glass, and R. F. Davis, Appl. Phys. Lett. **49**, 1074 (1986).
3. K. Shibahara, N. Kuroda, S. Nishino, and H. Matsunami, Jpn. J. Appl. Phys. **26**, L1815 (1987).

4. H. S. Kong, B. L. Jiang, J. T. Glass, G. A. Rozgonyi, and K. L. More, J. Appl. Phys. **63**, 2645 (1988).
5. H. S. Kong, J. T. Glass, and R. F. Davis, J. Appl. Phys. **64**, 2672 (1988).
6. N. Kuroda, K. Shibahara, W. Yoo, S. Nishino, and H. Matsunami, in *Extended Abstracts of the 19th Conf. on Solid State Devices and Materials*, (Business Center for Academic Societies, Tokyo, 1987) p. 227.
7. S. Kaneda, Y. Sakamoto, T. Mihara, and T. Tanaka, J. Cryst. Growth **81**, 536 (1987).
8. T. Yoshinobu, H. Mitsui, I. Izumikawa, T. Fuyuki, and H. Matsunami, Appl. Phys. Lett. **60**, 824 (1992).
9. L. B. Rowland, R. S. Kern, S. Tanaka, and R. F. Davis, in *Proceedings of 4th International Conference on Amorphous and Crystalline Silicon Carbide and Related Materials*, (Springer-Verlag, Berlin, 1992) (in press).
10. J. C. Bravman and R. Sinclair, J. Electron Microsc. Tech. **1**, 53 (1987).
11. J. A. Powell, D. J. Larkin, L. G. Matus, W. J. Choyke, J. L. Bradshaw, L. Henderson, M. Yoganathan, J. Yang, and P. Pirouz, Appl. Phys. Lett. **56**, 1353 (1990).
12. Y. C. Wang, M. S. Thesis, North Carolina State University, 1991.

THIN FILM GROWTH AND CHARACTERIZATION OF SOLID SOLUTIONS AND MULTI-LAYER HETEROSTRUCTURES FROM SILICON CARBIDE AND III-V NITRIDES

VI. Solid Solutions of AlN and SiC Grown by Plasma-Assisted, Gas-Source Molecular Beam Epitaxy

A Communication Submitted for Consideration for Publication
to
The Journal of Materials Research

by

R. S. Kern, L. B. Rowland*, S. Tanaka, and R. F. Davis
North Carolina State University
Department of Materials Science and Engineering
Box 7907
Raleigh, NC 27695-7907

November 1992

ABSTRACT

Solid solutions of aluminum nitride (AlN) and silicon carbide (SiC), the only intermediate phases in their respective binary systems, have been grown at 1050°C on α(6H)-SiC (0001) substrates cut 3-4° off-axis toward $[11\bar{2}0]$ using plasma-assisted, gas-source molecular beam epitaxy. A film having the approximate composition of $(AlN)_{0.3}(SiC)_{0.7}$, as determined by Auger spectrometry, was selected for additional study and is the focus of this note. High resolution transmission electron microscopy (HRTEM) revealed that the film was monocrystalline with the wurtzite (2H) crystal structure.

---

* Present address: Naval Research Laboratory, Code 6861, 4555 Overlook Ave. SW, Washington, D. C. 20375-5000.

Silicon carbide is a wide bandgap material that exhibits polytypism, a one-dimensional polymorphism arising from the various possible stacking sequences of, e. g., the silicon and carbon layers along the directions of closest packing. The single cubic polytype, β-SiC, crystallizes in the zincblende structure, has a room temperature bandgap of 2.3 eV, and is commonly referred to as 3C-SiC. The three (3) refers to the number of Si and C bilayers necessary to produce a unit cell and the C indicates its cubic symmetry. There are approximately 250 other rhombohedral and hexagonal polytypes[1] that are classed under the heading of α-SiC. The most common of these latter polytypes is 6H-SiC with a room temperature bandgap of ≈ 3.0 eV.

Aluminum nitride normally occurs in the wurtzite (2H) structure; however, the cubic, zincblende phase has been produced[2,3]. The 2H polytype possesses a direct bandgap[4] and a thermal conductivity[5] of 6.28 eV and 3.2 W/cm°K, respectively. As such, this material is of particular interest for high power and optoelectronic devices, the latter of which would emit and absorb ultraviolet radiation.

Solid solutions of AlN and SiC have been achieved by two primary routes: reactive sintering of mixtures of powders of a variety of sources and thin film deposition from the vapor phase. Matignon[6] first reported the synthesis of a $(AlN)_x(SiC)_{1-x}$ material in 1924 formed by heating Al_2O_3, SiO_2, and coke in the presence of flowing N_2 at an unspecified temperature. Related hot pressing and annealing research coupled with X-ray diffraction and optical and electron microscopy by Rafaniello et al.[7,8] reportedly resulted in single phase, 2H material at all compositions hot pressed at 2300°C but only within the ranges of 0-15 and 75-100 wt% AlN for samples prepared at 2100°C and below. This latter result indicated a miscibility gap, the existence of which was subsequently confirmed by Zangvil and Ruh[9-12], Kuo and Virkar[13], and Czeka et al.[14] using a variety of heat treatment schedules. The tentative phase diagram proposed by Zangvil and Ruh[11] shows a flat miscibilty gap at 1900°C between ≈ 8 and 95 wt% AlN. Above this temperature a 2H solid solution was reported from ≈ 20-100 wt% AlN. From 0-20 wt% AlN, solutions and two phase mixtures of 6H, 4H, and 2H were observed.

Thin film solid solutions have been produced in the Soviet Union[15] via sublimation of a sintered SiC/AlN compact at ≥ 2100°C and in the United States[16] using low pressure (10-76 Torr) metalorganic chemical vapor deposition (MOCVD) and the sources of SiH_4, C_3H_8, NH_3, and $Al(CH_3)_3$ carried in H_2. The former research also showed that at $T \geq 2100$°C, solid solutions having the 2H structure could be produced at compositions of AlN ≥ 20 wt%. By contrast, Jenkins et al.[16], have reported the MOCVD growth of solid solutions over the entire pseudobinary phase diagram. The composition of these films, grown from 1200-1250°C, was strongly dependent on the system pressure, which varied from 10-76 Torr. Electron channeling patterns on selected films indicated that the films were monocrystalline.

Films having cubic symmetry were obtained on Si (100) substrates; hexagonal films were deposited on α(6H)-SiC (0001) wafers.

In the present research, a specially designed and previously described[17] plasma-assisted, gas source molecular beam epitaxy system was employed to deposit $(AlN)_x(SiC)_{1-x}$ thin film solid solutions on α(6H)-SiC (0001) substrates obtained from Cree Research, Inc. and oriented 3.5 ± 0.5° off (0001) toward $[11\bar{2}0]$. The substrates were chemically cleaned before growth in a 10% HF solution for 5 minutes, followed by a DI water rinse for 2 minutes, and loaded immediately into the growth chamber. Sources of Si and C were disilane, Si_2H_6, and ethylene, C_2H_4, respectively. Aluminum (99.999% purity) was evaporated from a standard MBE effusion cell. A compact electron cyclotron resonance (ECR) plasma source supplied by ASTeX, Inc., was used to decompose N_2 (99.9995% purity) diluted with ultra-high purity Ar to obtain sufficient electron-atom collisions to sustain a plasma. The growth conditions for the composition chosen for additional study are listed in Table I.

Table I. Growth Conditions for $(AlN)_{0.3}(SiC)_{0.7}$ Thin Films

Chamber Base Pressure	10^{-9} Torr.
Deposition Pressure	10^{-4} Torr.
Deposition Temperature	1050°C
Flow Rate (Si_2H_6)	0.75 sccm
Flow Rate (C_2H_4)	3.75 sccm
Ar:N_2 Ratio	20:1
ECR Power	100 W
Aluminum Cell Temperature	1260°C
Deposition Time	2 hours

Reflection high-energy electron diffraction (RHEED) was used to determine the crystalline quality of the surface of the resulting films. The chemical composition as a function of film thickness was determined using a scanning Auger microprobe with Zalar rotation capability[18]. High-resolution transmission electron microscopy (HRTEM) was employed to observe the microstructure of the film as well as the film/substrate interfacial region.

Figure 1 shows an Auger depth profile of a selected solid solution film. Use of pure AlN and SiC standards and appropriate Auger sensitivity factors for each element showed the composition to be approximately $(AlN)_{0.3}(SiC)_{0.7}$.

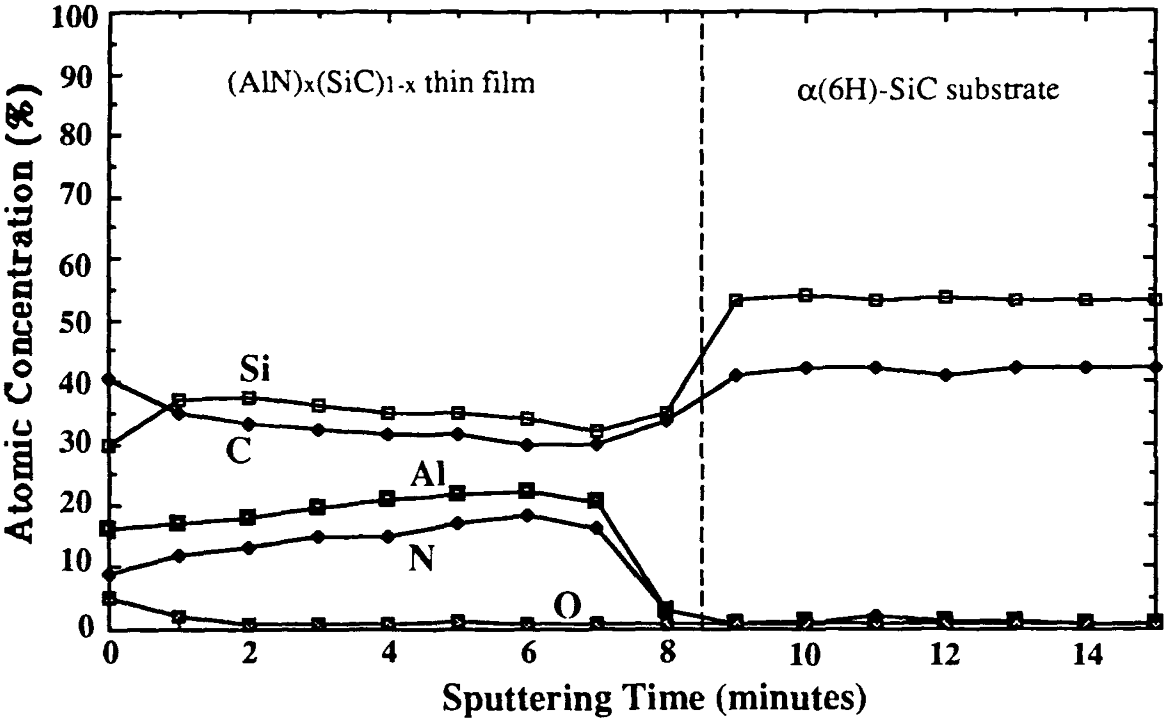

Figure 1. Auger depth profile of a $(AlN)_x(SiC)_{1-x}$ thin film ($x \approx 0.3$) showing relative atomic concentration versus sputtering time for each of the components.

The RHEED pattern indicated that the film was monocrystalline. This was confirmed using HRTEM. An image of the film and substrate used to obtain the Auger profiles is shown in Figure 2. The ...ABABAB... stacking sequence in the solid solution region shows that it possesses the wurtzite (2H) crystal structure. The fast Fourier transform pattern shown in the inset is that of the $[11\bar{2}0]$ azimuth for this structure. The random distribution of contrast is due to the elastic strain and slight buckling in the film. No second phase was observed within the film.

The resulting $(AlN)_x(SiC)_{1-x}$ thin films are, to the authors' knowledge, the first MBE grown alloys containing these components. The temperature of growth is also the lowest reported for these materials. This method of bandgap engineering is particularly interesting from the standpoint of the materials involved. AlN is a direct transition material, while SiC is an indirect one. Solid solutions of the wurtzite crystal structure (2H) should have E_g from 3.33 eV to 6.28 eV. Experimental optical characterization by Nurmagomedov et al.[14] has indicated that the bandgap is direct from 70-100 wt% AlN. The bandgap of cubic AlN has been theoretically estimated to be ≈ 5.11 eV at absolute zero and is believed to be indirect[15]. Therefore, cubic solid solutions should have E_g from 2.28 eV to roughly 5.11 eV and would probably be indirect at all compositions.

Epitaxial $(AlN)_x(SiC)_{1-x}$ alloys have been grown on α(6H)-SiC (0001) substrates by plasma-assisted gas-source molecular beam epitaxy at 1050°C. The $(AlN)_{0.3}(SiC)_{0.7}$ composition was selected for additional study. Analyses by RHEED and HRTEM showed this film to be monocrystalline and to exhibit the wurtzite (2H) crystal structure. This is the first known report of a single crystal $(AlN)_x(SiC)_{1-x}$ alloy grown by MBE.

The authors acknowledge The Office of Naval Research for the sponsorship of this research under Contract Number N00014-88-K-0341, Cree Research, Inc. for the vicinal 6H-SiC substrates, Applied Science and Technology, Inc. for the ECR plasma source, R. L. Moore at Evans East for the AES analysis, and J. Bentley of Oak Ridge National Laboratories for helpful discussions. This research was also partially sponsored by the Division of Materials Sciences, United States Department of Energy, under contract DE-AC05-840R21400 with Martin Marietta Energy Systems, Inc., and through the SHaRE Program under contract DE-AC05-760R00033 with Oak Ridge Associated Universities.

REFERENCES

1. G. R. Fisher and P. Barnes, Philos. Mag. B **61**, 217 (1990).
2. Z. Sitar, M. J. Paisley, and R. F. Davis, Annual Progress Report, ONR Contract N00014-86-K-0686, June 1, 1989.
3. S. Strite and H. Makoç, private communication.
4. G. A. Slack, J. Phys. Chem. Solids **34**, 321 (1973).
5. W. M. Yim, E. J. Stofko, P. J. Zanzucci, J. I. Pankove, M. Ettenberg, and S. L. Gilbert, J. Appl. Phys. **44**, 292 (1973).
6. C. Matignon, Compt. Rend. hu. L'Acad. Sci. **178**, 1615 (1924).
7. W. Rafaniello, K. Cho, and A. V. Vikar, J. Mat. Sc. **16**, 3479 (1981).
8. W. Rafaniello, M. R. Plinchta, and A. V. Vikar, J. Am. Ceram. Soc. **66**, 272 (1983).
9. R. Ruh and A. Zangvil, J. Am. Ceram. Soc. **65**, 260 (1982).
10. A. Zangvil and R. Ruh, Mat. Sc. Eng. **71**, 159 (1985).
11. A. Zangvil and R. Ruh, J. Am. Ceram. Soc. **71**, 884 (1988).
12. A. Zangvil and R. Ruh in *Silicon Carbide* '87, American Ceramic Society, Westerville, OH, 1989, pp. 63-82.
13. S. Kuo and A. V. Vikar, J. Am. Ceram. Soc. **73**, 2460 (1990).
14. C. L. Czkaj, M. L. J. Hackney, W. J. Hurley, Jr., L. V. Interrante, G. A. Sigel, P. J. Schields, and G. A. Slack, J. Am. Ceram. Soc. **73**, 352 (1990).
15. Sh. A. Nurmagomedov, A. N. Pitkin, V. N. Razbegaev, G. K. Safaraliev, Yu. M. Tairov, and V. F. Tsvetkov, Sov. Phys. Semicond. **23**, 100 (1989).
16. I. Jenkins, K. G. Irvine, M. G. Spencer, V. Dmitriev, and N. Chen, in press.
17. L. B. Rowland, S. Tanaka, R. S. Kern, and R. F. Davis, in *Proceedings of the Fourth International Conference on Amorphous and Crystalline Silicon Carbide* (Springer-Verlag, Berlin, 1992), in press.
18. A. Zalar, Thin Solid Films **124**, 223 (1985).

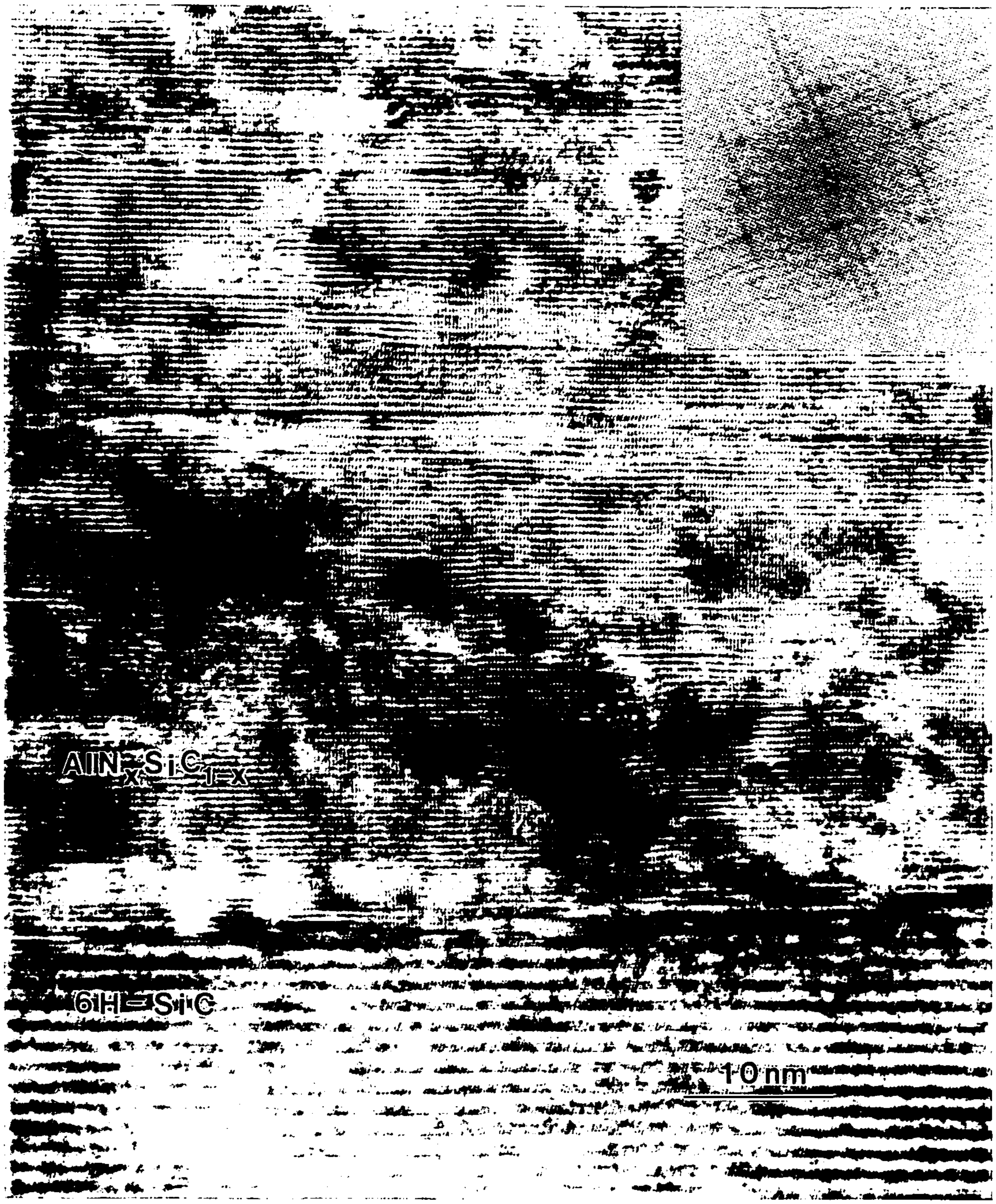

Figure 2. High-resolution transmission electron micrograph of the 2H $(AlN)_x(SiC)_{1-x}$ thin film grown on an α(6H)-SiC (0001) substrate and used to obtain the Auger depth profile in Figure 1.

VII. Aluminum Nitride/Silicon Carbide Multilayer Heterostructure Produced by Plasma-Assisted Gas-Source Molecular Beam Epitaxy

Submitted for Consideration for Publication
to
Applied Physics Letters

L. B. Rowland*
R. S. Kern
S. Tanaka
Robert F. Davis

North Carolina State University
Department of Materials Science and Engineering
Box 7907
Raleigh, North Carolina 27695-7907

November, 1992

ABSTRACT

Pseudomorphic bilayer structures containing β(3C)-SiC and 2H-AlN have been grown on vicinal α(6H)-SiC(0001) homoepitaxial layers at 1050°C by plasma-assisted, gas source molecular beam epitaxy. High energy electron diffraction and cross-sectional high-resolution transmission electron microscopy showed all layers to be monocrystalline. The AlN layers were uniform in thickness. Defects in these layers were initiated at steps on the 6H-SiC film. The 3C-SiC layers contained a high density of stacking faults and microtwins caused primarily by the interfacial stresses generated by the mismatch in lattice parameters between AlN and β-SiC coupled with the very low stacking fault energy of SiC. This is the first report of the deposition of single crystal SiC/AlN/SiC thin film heterostructures on any substrate as well as the first report of the epitaxial growth of single crystal layers of binary materials with three different crystal structures.

---

*Present Address
Naval Research Laboratory, Code 6861
4555 Overlook Av., SW
Washington, DC 20375-5320

Interest in wide bandgap semiconductors for high-temperature and high-power electronic and short-wavelength optoelectronic applications has increased markedly within the past several years. Two materials which have generated much interest in this regard are SiC and AlN. The former occurs in over 250 polytypes which differ only in their stacking sequence along the closest-packed direction. The most common of these are the cubic 3C and the hexagonal 6H, where the number refers to the number of Si and C bilayers necessary to produce a unit cell in the direction of closest packing. The 3C polytype is also referred to as β-SiC. All other forms are known collectively as α-SiC. The bandgap (3.0 eV for 6H and 2.28 eV for 3C at room temperature) is indirect in all polytypes; thus, they cannot be used alone for laser applications.

Aluminum nitride has considerable potential for electronic and ultraviolet optoelectronic applications, particularly in severe environments, due to its large and direct bandgap (6.28 eV at 300°C), high melting point (in excess of 2000°C), high thermal conductivity (3.2 W/cm·K), and low dielectric constant ($\varepsilon=9.0$). It typically forms in the wurtzite (2H) structure; however, the cubic, zincblende (3C) phase has recently been produced via molecular beam epitaxy (MBE) techniques [1, 2]. Additional characteristics of the 2H polytype include a high resistivity and ease of oxygen incorporation during growth.

Epitaxial wurtzitic AlN has been deposited previously on SiC substrates [3–5]. Chu et al. [3] obtained monocrystalline AlN layers of up to 25 μm thickness on hexagonal SiC{0001} substrates by chemical vapor deposition (CVD) from 1200-1250°C. Sitar et al. [4] used an electron cyclotron resonance (ECR) plasma for decomposition of N_2 and Al and Ga effusion cells for growth of AlN/GaN superlattices by plasma-assisted, gas source MBE on α(6H)-SiC(0001) and $Al_2O_3(0001)$ at 600°C. The thickness range of the AlN layers was 0.5–20nm. However, the properties of the individual AlN layers were not examined. Yoshida et al. [5] also employed gas–source MBE and the sources of solid Al and NH_3 to deposit single crystal AlN films on Si(111) and $Al_2O_3(0001)$ and $(01\bar{1}2)$ at 1000-1200°C. They noted their films were much smoother than CVD-grown material and rivaled bulk single crystal AlN. Conversely, Rutz and Cuomo [6] reported the deposition of monocrystalline SiC on a single crystal AlN film by pyrolysis of a SiC target at 1860°C. The AlN substrate was previously formed at 1000°C by reactive rf sputtering on a W(111) single crystal. However, thin-film growth of AlN/SiC/AlN or SiC/AlN/SiC heterostructures has not been reported to date.

Stable pseudomorphic heterostructures of AlN and SiC are feasible because of their similarity in crystal structure, lattice parameter and thermal expansion behavior. Theory regarding the electronic structure and bonding at SiC/AlN interfaces has been developed [7]. Critical layer thicknesses prior to misfit dislocation formation at pseudomorphic interfaces of cubic AlN and cubic SiC have been calculated [8]. Superlattices of these materials would have a different band structure than either constituent element because the Brillouin zone is reduced in size in the direction normal to the interfaces, and certain superlattice states occur at different points in *k* space than the corresponding bulk material [9]. This may allow the resultant superlattice to have a direct band transition.

In the present research multiple layers of AlN and SiC were grown using a specially designed plasma-assisted gas-source molecular beam epitaxy (PAGSMBE) system. A schematic of this equipment is shown in Figure 1. This system is similar to that described previously for SiC MBE growth [10]. The precursors used for Si and C were Si_2H_6 and C_2H_4 (both 99.99% pure), respectively. Solid Al (99.999% pure) was evaporated from a standard effusion cell. Nitrogen was obtained by electron cyclotron resonance (ECR) plasma decomposition of N_2 (99.9995% pure). The system base and working pressures were 10^{-9} and 3×10^{-5} torr, respectively. Vicinal 6H-SiC(0001) wafers oriented 3-4° towards [11$\bar{2}$0] and containing a thermally oxidized(50nm) 0.8 μm epitaxial 6H-SiC layer deposited via CVD were obtained from Cree Research, Inc. and used as substrates in this research These substrates were chemically cleaned prior to growth in a 10% HF solution for five min. to remove the oxide, rinsed in DI H_2O for two min, immediately loaded into the growth system and heated for five min at the growth temperature of 1050°C. Additional growth conditions are listed in Table I.

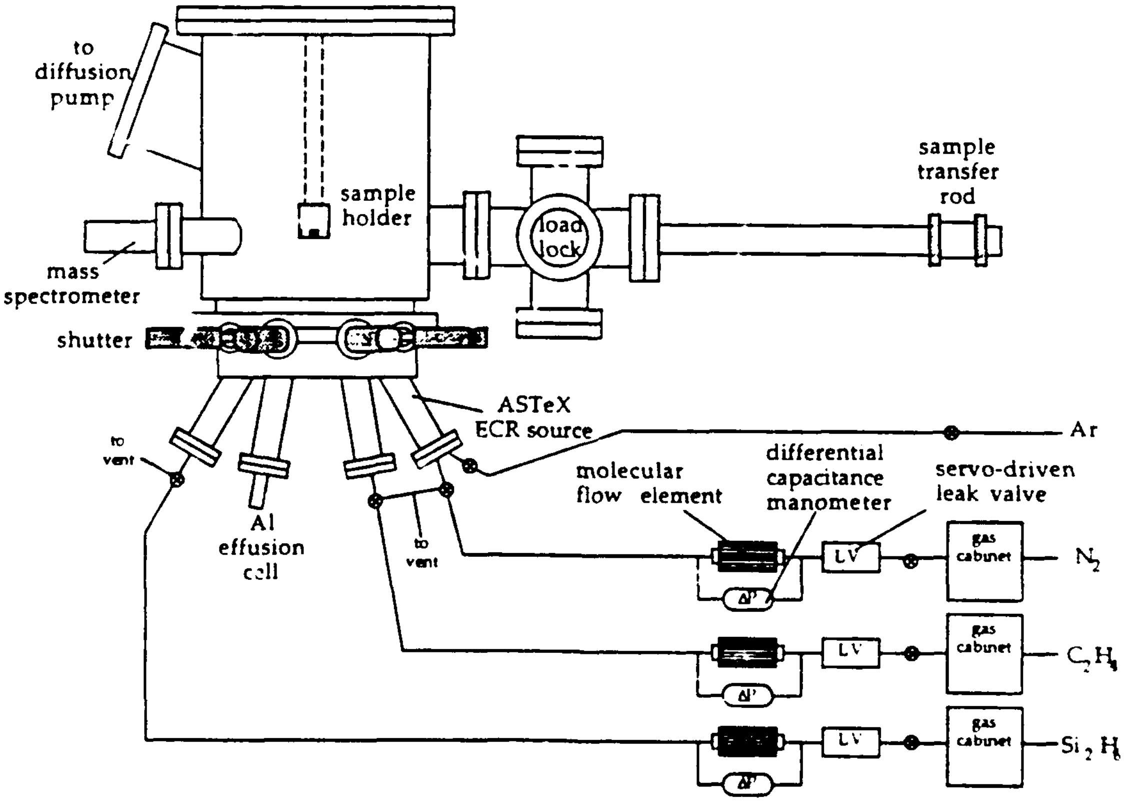

Figure 1. Schematic of gas-source molecular beam epitaxy system use to deposit the SiC and AlN films in this research.

Table I. Growth Conditions for the AlN and SiC Layers

AlN	
Growth temperature	1050°C
Nitrogen pressure	1.5×10^{-4} torr
Nitrogen flow rate	8 sccm
Microwave power	100 W
Growth rate	26 nm/hr
SiC	
Growth temperature	1050°C
Disilane flow rate	0.10 sccm
Ethylene flow rate	0.20 sccm
Growth rate	6.2 nm/hr

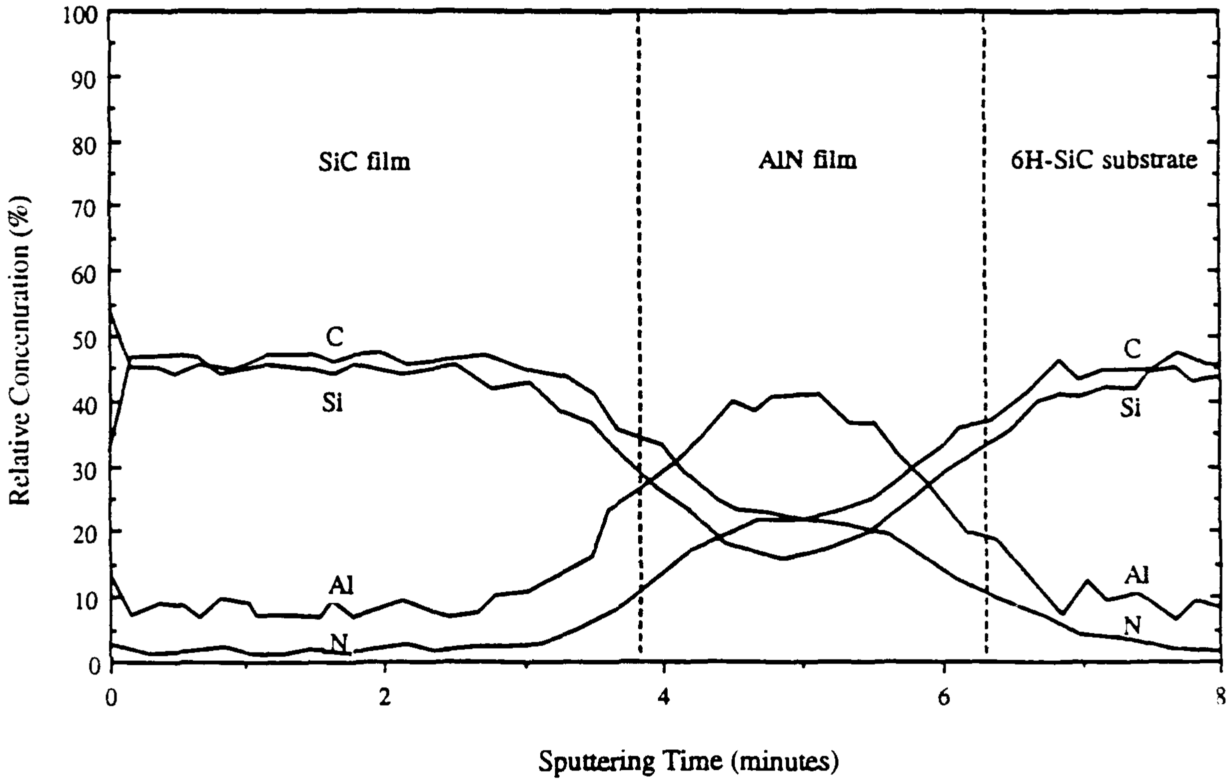

Figure 2. Auger depth profile of representative SiC/AlN/SiC multilayer heterostructure.

Reflection high-energy electron diffraction (RHEED) was used as an indicator of the quality and crystal structure of the resultant films. Figure 3 shows representative RHEED patterns for (a) the final growth surfaces of the films of AlN ([10$\bar{1}$0] azimuth) and (b) SiC ([110] aximuth). These patterns also show that both films were monocrystalline with the AlN having the 2H structure and the SiC the 3C modification, as indicated by the azimuthal assignments. The RHEED pattern of the top SiC layer also contains additional spots, as denoted by arrows in Figure 3(b). This pattern is fully indexed in Figure 4. It is probable that these extra spots arise from double positioning boundaries (DPBs). These incoherent twin boundaries occur when 3C-SiC (111) is grown on Si (111) [11] or on-axis 6H-SiC [12] because two different orientations, rotated 60° from each other, are present which have close-packed directions aligned in the interface. These different orientations differ in the cubic stacking sequence, as one orientation has an ...ABCABC... stacking sequence and the other has an ...ACBACB...stacking sequence. Extra reflections in the [110] RHEED pattern due to double positioning twins would either coincide with those of the film or be displaced by 1/3[111]. The extra spots present in the figure occur at 1/3 of the distance between adjacent spots in the [111] and [111] directions.

An equivalent interpretation of the RHEED pattern shown in Figure 3(b) is of two interpenetrating [110] RHEED patterns with a misorientation of 180°. This misorientation is caused by reflections from regions with both ...ABCABC... and ...ACBACB... sequences. The effect of each individual stacking sequence as well as the resultant RHEED pattern due to contributions of the two equivalent stacking sequences are shown in Figure 5.

Figure 6 shows a representative HRTEM image of the off-axis 6H-SiC (0001) substrate, the 2H-AlN layer, and the 3C-SiC layer. The interface between the SiC substrate and the AlN is abrupt with little change in contrast across it. The surface of the AlN film is smooth and uniform. The 2H-AlN and 6H-SiC films are in the same orientation in all directions, and the alignment of the atom columns is continuous across the interface. Thus, the AlN film is both epitaxial and pseudomorphic with respect to the substrate. Strain contrast, as evidenced by distortion in the lattice fringes, can be seen near steps in the SiC substrate surface, as denoted by arrows in Figure 6. Dislocations running parallel to the surface which arise from this strain can also be observed at or near each step.

The interface between the AlN and the top 3C-SiC layer is also abrupt, though some regions exist for which the transition between AlN and SiC becomes indiscernible. The lattice structural images show that the SiC layer is indeed cubic as well as epitaxial and pseudomorphic with the AlN. Several <111> stacking faults can be seen in the cubic SiC layer.

Previous PAGSMBE growth in this research of SiC on similar substrates at 1000–1050°C also resulted in 3C-SiC(111). This result, combined with those noted above, suggest that the cubic polytype forms preferentially at these temperatures under the conditions of low growth

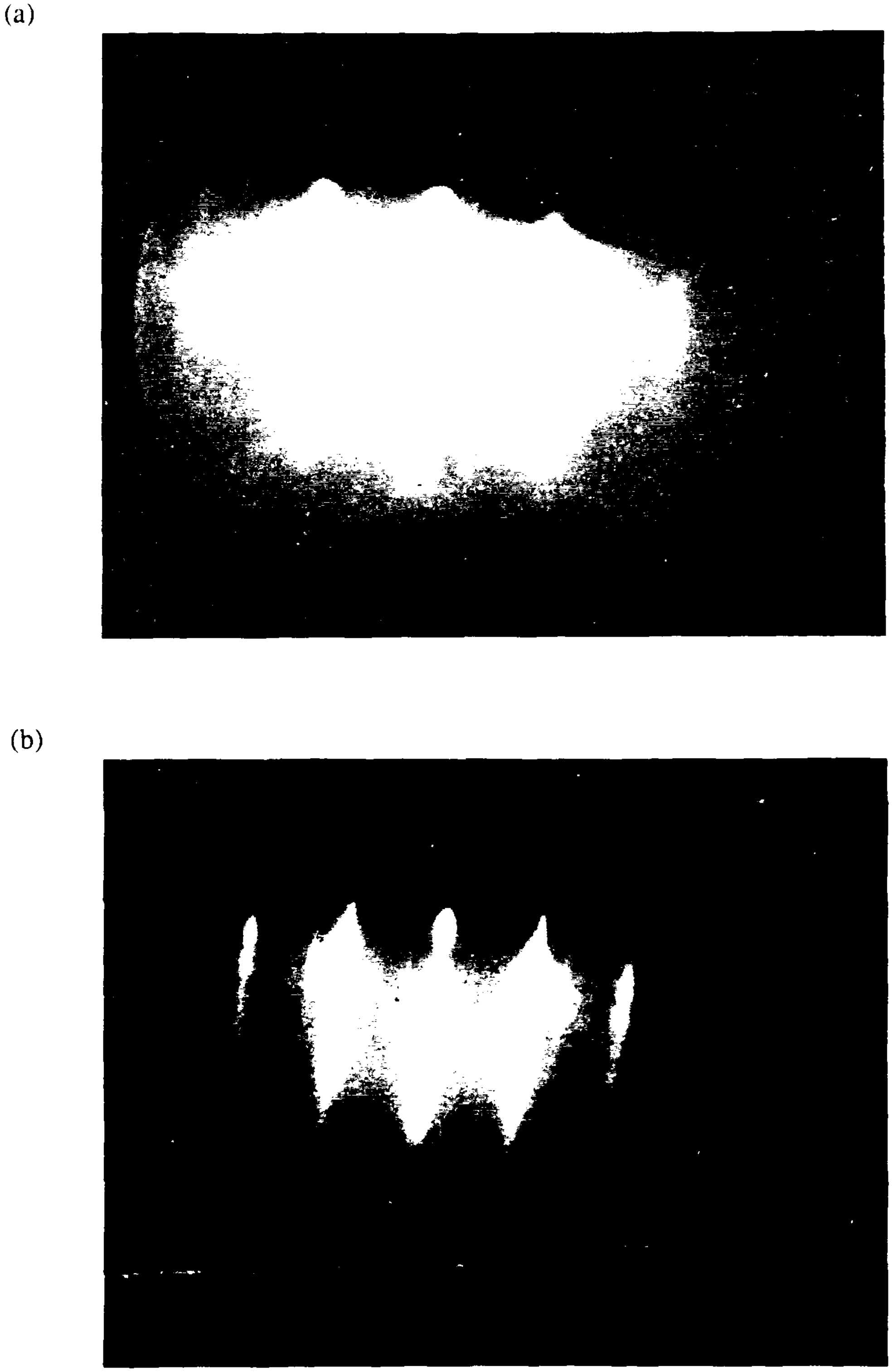

Figure 3. (a) RHEED pattern ([10$\bar{1}$0] azimuth) of the final surface of a monocrystalline 2H-AlN layer grown on α(6H)-SiC epitaxial layer.

(b) RHEED pattern ([110] azimuth) of the final surface of a monocrystalline 3C-SiC layer grown on 2H-AlN film. Arrows denote additional spots in the 3C-SiC layer (see Figures 4 and 5 for indexing).

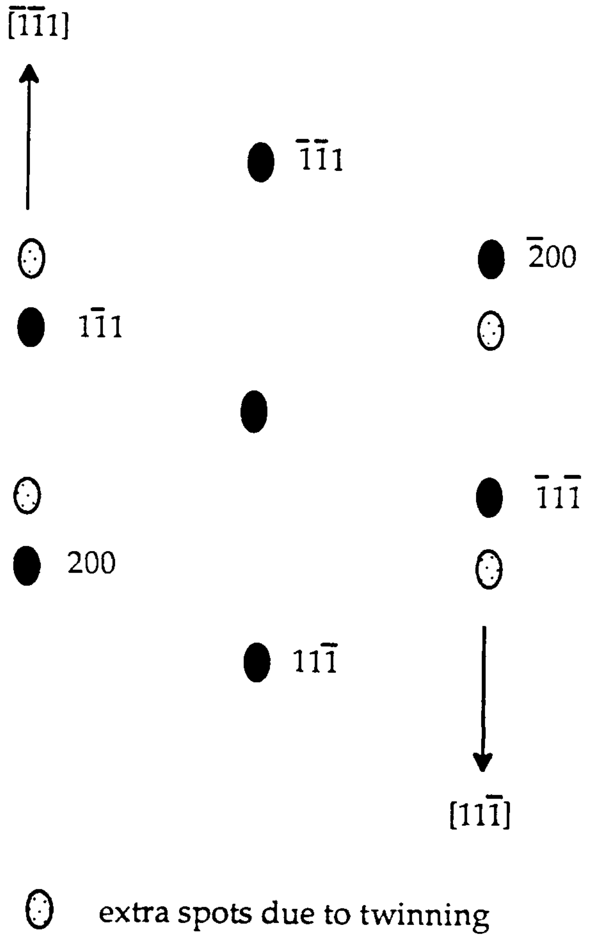

Figure 4. Indexed RHEED pattern ([110] azimuth) of 3C-SiC layer. Lighter spots are twin spots caused by double positioning boundaries.

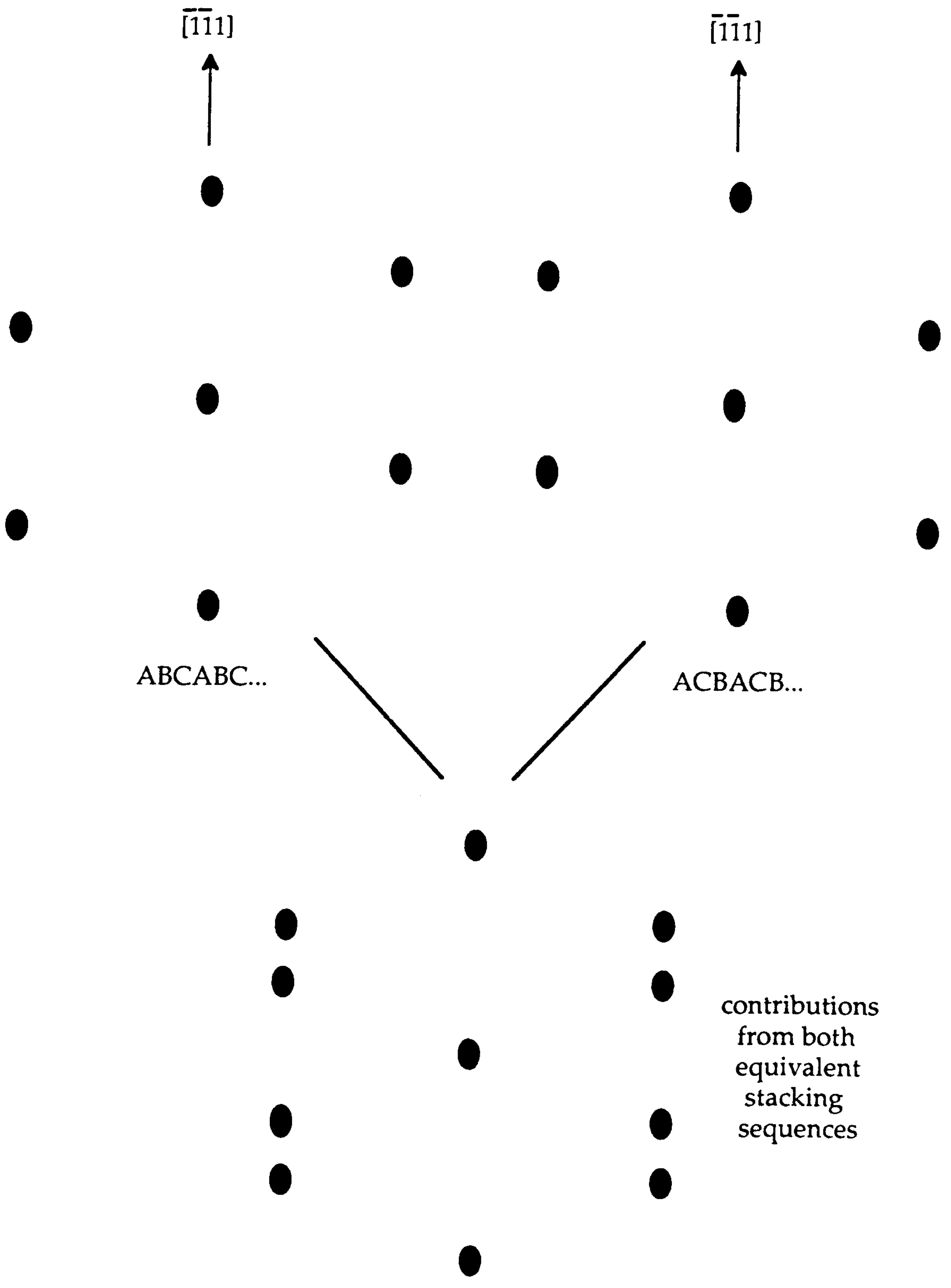

Figure 5. Effect of two equivalent stacking sequences of 3C-SiC (111) on [110] azimuth RHEED pattern.

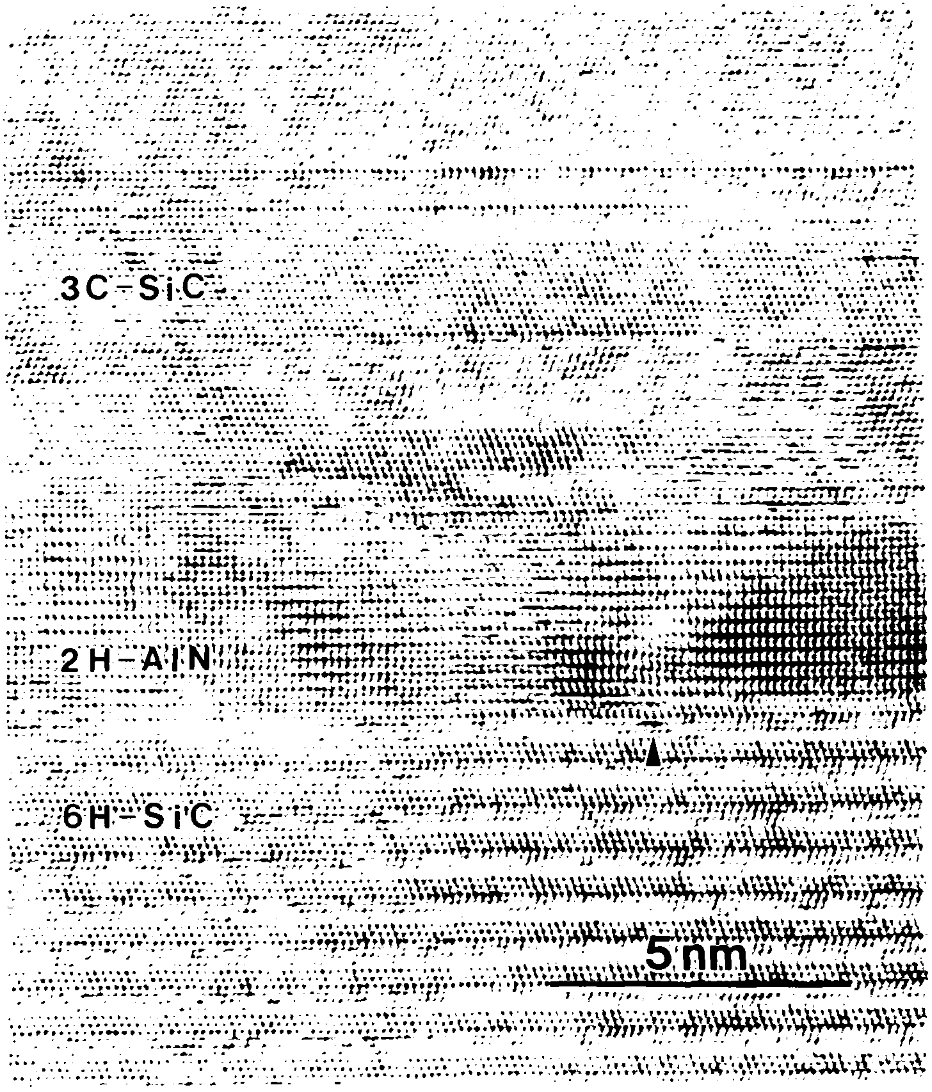

Figure 6. High-resolution transmission electron micrograph of epitaxial, pseudomorphic SiC/AlN/SiC multilayer heterostructure. Arrow shows a position of lattice distortion in the AlN associated with steps contained in and dislocations running parallel to the SiC surface.

rate and high supersaturation used in MBE. However, growth of SiC/AlN heterostructures at higher temperatures may result in hexagonal SiC layers, as atomic mobility on the AlN surface increases and the steps rather than the terraces become the templates for layer-by-layer growth. This trend towards the deposition of hexagonal SiC films at higher temperatures has been reported by several investigators[12-14]. It is also under study in the authors' laboratory and will be reported in the near future.

In summary, thin-film heterostructures composed of 3C-SiC, 2H-AlN and 6H-SiC have been achieved. The 3C-SiC and the AlN layers were grown at 1050°C using PAGSMBE. The diagnostic tools of RHEED and cross-sectional HRTEM showed both of these layers to exist in an epitaxial and pseudomorphic relationship with each other and with the 6H–SiC homoepitaxial layer deposited by CVD. To the authors' knowledge, this is the first report and direct observation of a single crystal SiC/AlN/SiC heterostructure on any substrate. It is also the first known report of the single-crystal growth of layers of binary materials in three different crystal structures (the 6H-SiC epilayer on the SiC wafer is counted in this case). These unique structures, composed of direct (AlN) and indirect (SiC) wide bandgap semiconductor materials undoubtedly possess important electronic, mechanical and thermal properties which are under investigation by the authors at this time.

The authors express their appreciation to the Office of Naval Research for support of this research under Grant #N00014-90-J-1427, to Cree Research, Inc. for the vicinal 6H-SiC wafers and epilayers and to Applied Science and Technology, Inc. for supplying the ECR plasma source. Appreciation is also expressed to S. Rogers for the Auger microprobe analysis.

REFERENCES

1. Z. Sitar, Ph. D. dissertation, North Carolina State University, 1990.
2. S. Strite and H. Morkoç, private communication.
3. T. L. Chu, D. W. Ing, and A. J. Norieka, Solid-State Electron. **10**, 1023 (1967).
4. Z. Sitar, M. J. Paisley, B. Yan, R. F. Davis, J. Ruan, and J. W. Choyke, Thin Solid Films **200**, 311 (1991).
5. S. Yoshida, S. Mizawa, Y. Fujii, S. Takada, H. Hayakawa, S. Gonda, and A. Itoh, J. Vac. Sci. Technol. **16**, 990 (1979).
6. R. F. Rutz and J. J. Cuomo, *Silicon Carbide-1973*, (U. of S.C., Columbia, 1974), p. 72.
7. W. R. L. Lambrecht and B. Segall, Phys. Rev. B **43**, 7070 (1991).
8. M. E. Sherwin and T. J. Drummond, J. Appl. Phys. **69**, 8423 (1991).
9. G. C. Osbourn, J. Vac. Sci. Technol. B **1**, 379 (1983).
10. L. B. Rowland, R. S. Kern, S. Tanaka, and R. F. Davis, in *Proceedings of the Fourth International Conference on Amorphous and Crystalline Silicon Carbide* (Springer-Verlag, Berlin), in press.
11. I. H. Khan and R. N. Summergrad, Appl. Phys. Lett. **11**, 12 (1967).
12. H. S. Kong, B. L. Jiang, J. T. Glass, G. A. Rozgonyi, and K. L. More, J. Appl. Phys. **63**, 2645 (1988).
13. R. B. Campbell and T. L. Chu, J. Electrochem. Soc. **113**, 825 (1966).
14. V. J. Jennings, A. Sommer, and H. C. Chang, J. Electrochem. Soc. **113**, 728 (1966).

THIN FILM GROWTH AND CHARACTERIZATION OF III-V MATERIALS

VIII. Epitaxial Growth of AlN by Plasma-Assisted Gas-Source Molecular Beam Epitaxy

A Communication
Submitted for Consideration for Publication
to
The Journal of Materials Research

L. B. Rowland*, S. Tanaka, R. S. Kern and Robert F. Davis
Department of Materials Science and Engineering
North Carolina State University
Box 7907
Raleigh, North Carolina 27695-7907

November, 1992

ABSTRACT

Monocrystalline AlN(0001) films with few defects were deposited on vicinal α(6H)-SiC(0001) wafers via plasma-assisted gas-source molecular beam epitaxy within the temperature range of 1050–1200°C. The Al was thermally evaporated from an effusion cell. An electron cyclotron resonance plasma source was used to produce activated nitrogen species. Growth on vicinal Si(100) at 900–1050°C resulted in smooth, highly oriented AlN(0001) films.

---

*Present Address
Naval Research Laboratory, Code 6861
4555 Overlook Av., SW
Washington, DC 20375-5320

Aluminum nitride possesses a direct bandgap of 6.28 eV at 300 K [1], a melting point in excess of 2275 K [2] and a thermal conductivity of 3.2 W/cm·K [3]. As such, it is a candidate material for high-power and high-temperature microelectronic and optoelectronic applications with the latter employment being particularly important in the ultraviolet region of the spectrum [1]. This material also has the highest reported surface acoustic wave velocity (Raleigh V_R=6–6.2 km/s, V_L=11-12 km/s [4]-[6]) for any material and a substantial electromechanical coupling coefficient (to 1% [7]). These properties strongly indicate that superior surface acoustic wave devices, operational in aggressive media and under extreme conditions both as sensors for high temperatures and pressures and as acousto-optic devices can be developed [8-10]. However, progress regarding these (and other) applications is hampered by the lack of good single crystal material. The primary objective of the research reported below has been to address this issue via the fabrication of thin films of this material via molecular beam epitaxy (MBE) techniques.

In previous studies, mono- and polycrystalline films of AlN have been grown by chemical vapor deposition (CVD) using NH_3 and $Al(CH_3)_3$ or $AlCl_3$ on α(6H)-SiC [11], sapphire [1,9,12], and Si [13-15]. Chu et al. [11] obtained smooth monocrystalline AlN layers to a thickness of 25 μm on α(6H)-SiC{0001} substrates by chemical vapor deposition (CVD) from 1200-1250°C. A high density of defects in these AlN films was revealed by chemical etching. In general, films grown on sapphire and Si substrates possessed a rougher morphology than those grown on α(6H)-SiC. This occurred very likely because the difference in lattice parameters between AlN and SiC is substantially less than between AlN and sapphire or AlN and Si.

Gas source MBE using electron beam evaporated Al and NH_3 [16] or thermally evaporated Al and plasma-derived activated nitrogen species [17] has also been used for single crystal AlN growth. Yoshida et al. [16] obtained single crystal AlN using an Al effusion cell and NH_3 at 1000-1200°C on Si(111) and Al_2O_3(0001) and $(01\bar{1}2)$ and obtained growth rates of up to 1 μm/hr. They contended that their films were much smoother than CVD-grown material and rivaled bulk single crystal AlN. Sitar et al. [17] used an electron cyclotron resonance (ECR) plasma for decomposition of N_2 and Al and Ga effusion cells for growth of AlN/GaN superlattices by plasma-assisted, gas source (PAGSMBE) on α(6H)-SiC (0001) and Al_2O_3 (0001) at 600°C. The thickness range of the AlN layers was 0.5–20nm, as determined by cross-sectional transmission electron microscopy (TEM). However, the properties of the individual AlN layers were not examined.

The approach taken in the present research has also been to use PAGSMBE to achieve surface reactions involving only Al and N in order to minimize the potential for unintentional impurity contamination from the p- and n-type dopants of C and O, respectively. The AlN films were grown on vicinal Si(100) wafers oriented 3.5 ± 0.5° towards [011] at 900-1050°C and vicinal α(6H)-SiC (0001) oriented 3-4° towards [11$\bar{2}$0] at 1050-1200°C in a PAGSMBE system described previously [18]. These temperatures are higher than necessary for the formation of single crystal AlN. However, they were employed to match the growth temperatures previously determined to be necessary to achieve single crystal films of SiC on Si(100) [18-20] and α(6H)-SiC(0001) substrates [21,22].

Silicon(100) substrates were chemically cleaned using the following steps: (1) H_2SO_4 at 70°C for 5 min, (2) deionized water for 1 min, (3) 1:1 solution (by volume) of NH_4OH and 50% H_2O_2 at 70°C for 5 min, (4) deionized water for 1 min, (5) dip in 10% HF at room temperature, and (6) 2 min rinse in deionized water. Silicon carbide substrates were only subjected to cleaning steps (5) and (6) prior to introduction to the growth system. Thermal desorption of all substrates was also conducted at the growth temperature for 5 min prior to deposition to remove any remaining hydrocarbon and/or oxide contamination. An effusion cell was used for the evaporation of Al (99.999% pure). Reactive nitrogen species were produced via decomposition of N_2 (99.999% pure) in a compact electron cyclotron resonance (ECR) plasma source (Applied Science and Technology, Inc.). The pressure of the introduced N_2 was 1.2-1.5 x 10^{-4} torr. The microwave power supplied to the ECR was 100 W for all depositions.

The crystallography and surface character on the films were initially studied *in situ* using reflection high-energy electron diffraction (RHEED). The microstructure of the final growth surface was investigated using field-emission scanning electron microscopy (SEM). The orientation of the films grown on Si was determined via x-ray diffraction. A more in-depth examination of the crystallinity and the nature and distribution of the line and planar defects in the films deposited on 6H-SiC was conducted using high-resolution transmission electron microscopy (HRTEM). The composition of the films, including any significant impurities, was determined using an Auger electron microprobe.

Figure 1 shows the RHEED patterns ([11$\bar{2}$0] azimuth) of AlN films grown on the 6H-SiC (0001) substrates at (a) 1200°C, (b) 1100°C and (c) 1050°C. These patterns indicate that all the films possess the wurtzite structure and are monocrystalline.

The growth rate versus temperature was essentially constant for a given Al flux. Conversely, changes in the AlN growth rate corresponded directly to changes in the Al flux. A constant Al source temperature and, consequently, a constant Al flux were used at the the three temperatures of growth. An excess of activated nitrogen was present under all conditions. A constant growth rate of ≈0.40 nm/min was obtained at these temperatures.

Scanning Auger analysis of these films detected only Al and N except in a 2 nm surface region where the native oxide (and very likely the hydroxide) had formed during exposure to air. The stoichiometry of these films was very close to that obtained from analysis of high-purity, hot-pressed polycrystalline AlN. Figure 2 shows a HRTEM image of a thin AlN layer

(a)

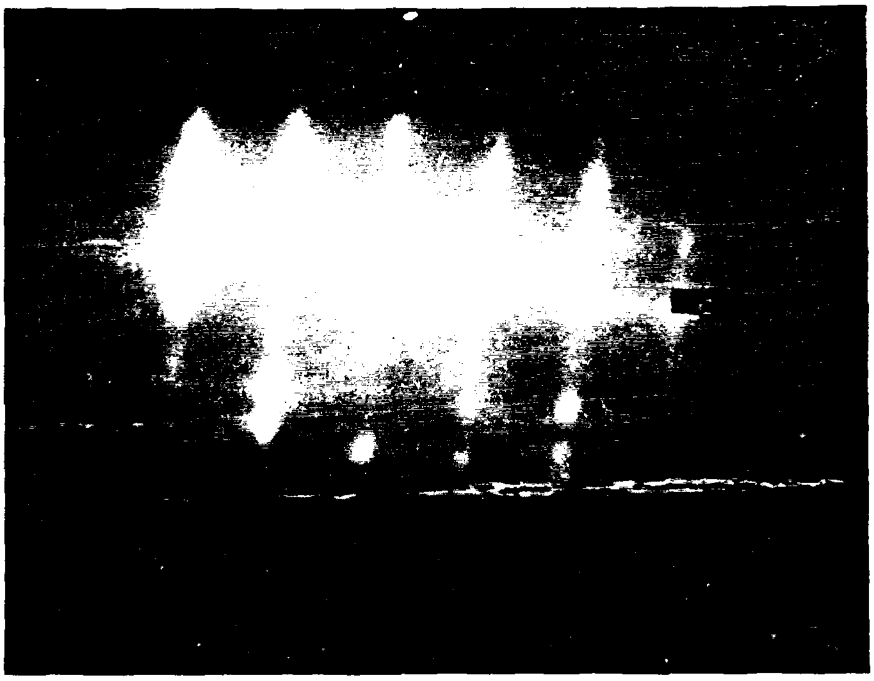

(b)

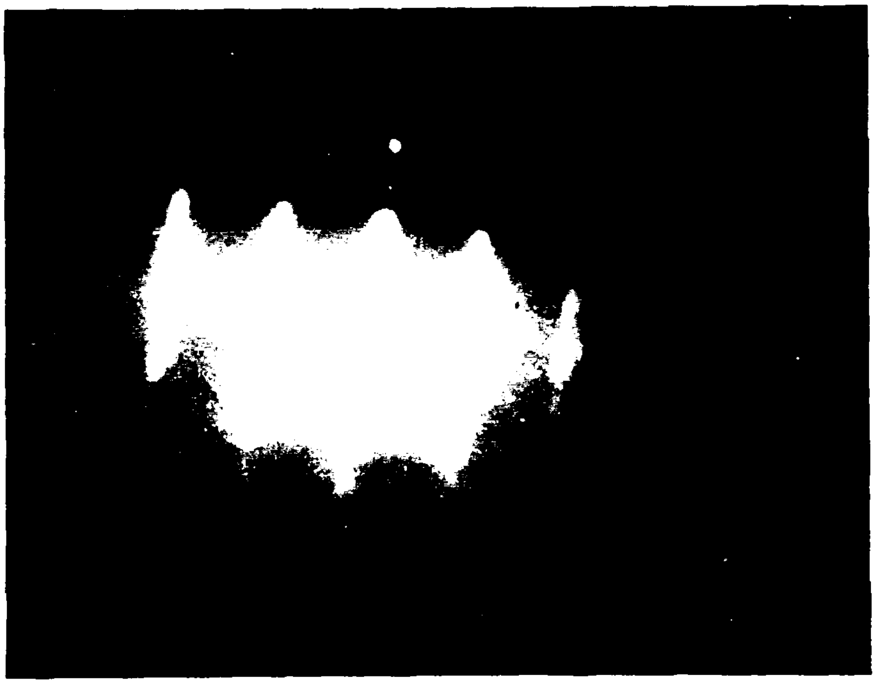

Figure 1. RHEED patterns ([11$\bar{2}$0] azimuth) of AlN grown on vicinal 6H-SiC(0001) at (a) 1200°C, (b) 1100°C, and (c) 1050°C.

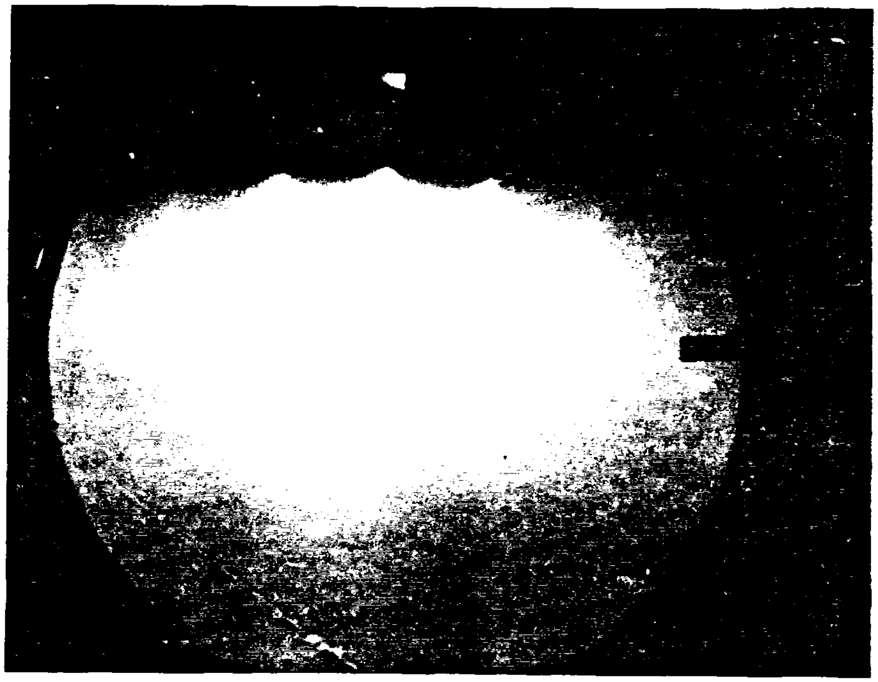

Fig. 1. (c) 1050°C.

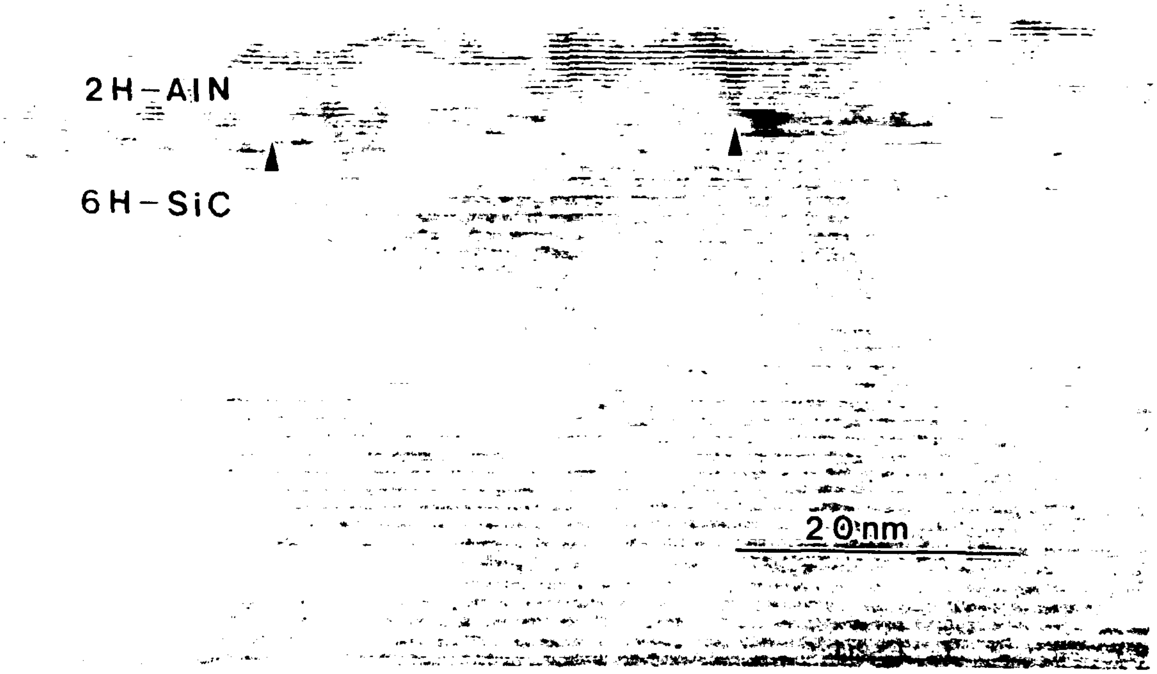

Figure 2. HRTEM micrograph of AlN film grown at 1200°C on vicinal 6H-SiC (0001). Arrows point to areas of lattice distortion in the lattice fringes of the AlN.

deposited on the 6H-SiC at 1200°C. The top surface of the AlN is rough. Few defects are visible away from the interface. At the 2H-AlN/6H-SiC interface, however, strain contrast as evidenced by distortion in the lattice fringes can be seen (denoted by arrows in Figure 2).

A further reduction in temperature to 1050°C also resulted in the deposition of single crystal AlN films (as indicated in Figure 1(c)) having an abrupt interface with the SiC substrates, but with a much smoother final surface, as shown in the SEM micrograph of Figure 3. This essentially featureless microstructure supports the RHEED results. The surface morphology was difficult to observe at much higher magnifications in the SEM due to the insulating nature of both AlN and the SiC substrate. Figure 4 shows a HRTEM image of a film grown at 1050°C capped by a monocrystalline, cubic (zincblende structure) β-SiC(111) film grown in the same experiment. The smooth AlN surface and the abrupt junction with the β-SiC are apparent. Dislocations in the AlN films occurred at surface steps in the 6H-SiC substrate and may be observed in Figure 4 (see arrow). No other defects were observed in this material. The use of nominally on-axis 6H-SiC substrates with widely spaced steps will be studied in the near future to reduce the defects present in these films.

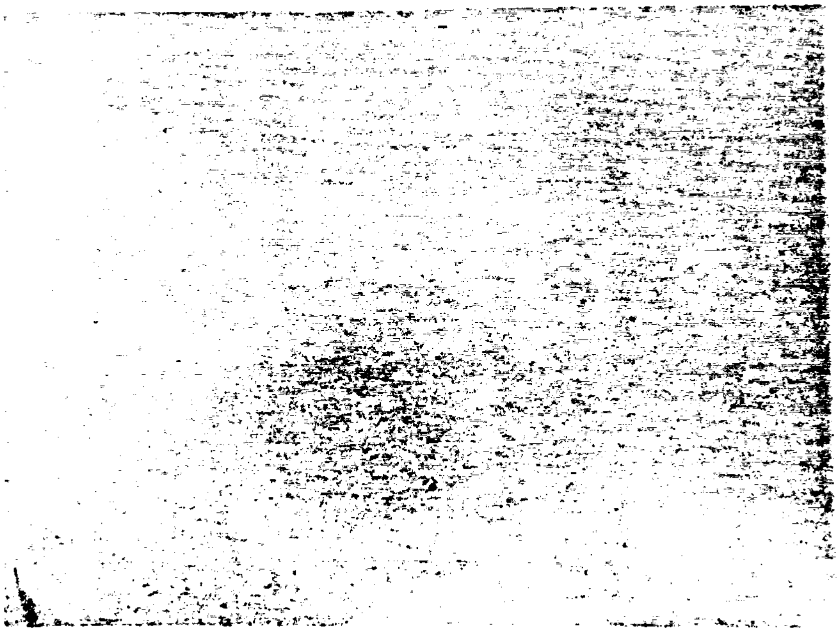

Figure 3. SEM micrograph of the surface morphology of an AlN film grown on vicinal 6H-SiC(0001) at 1050°C.

Figure 5 shows RHEED patterns of AlN layers deposited at 900 and 1050°C on Si(100) substrates. These films have the wurtzite structure and are very well-oriented. There is only a small amount of angular spread in the spots which implies that the films have a small non-epitaxial component. An X-ray diffraction scan of the film grown at 1050°C is shown in

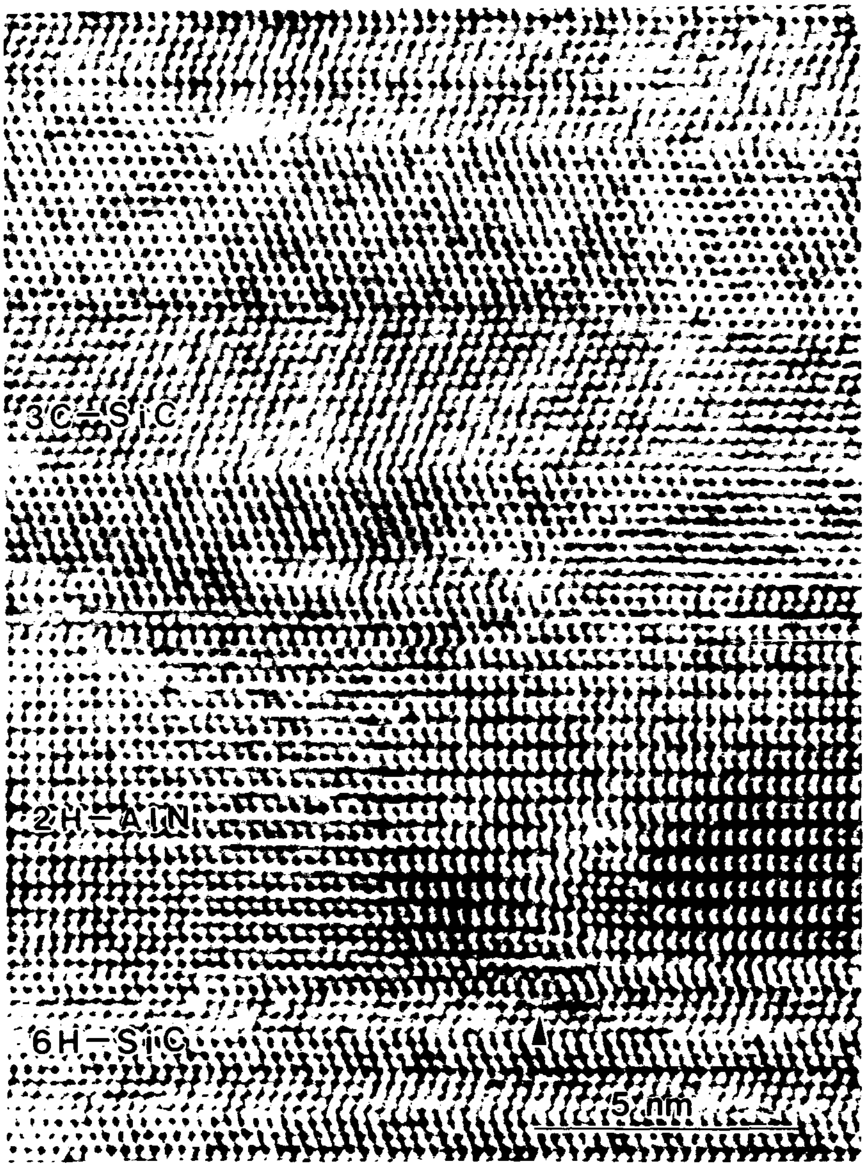

Figure 4. HRTEM micrograph of AlN film grown at 1050°C on vicinal 6H-SiC (0001). Layer above AlN layer is 3C-SiC also grown at 1050°C using gas-source MBE. Arrow points to dislocation in the AlN film at a step on the 6H–SiC surface.

Figure 6. The single (0002) AlN peak supports the RHEED results regarding orientation. The AlN therefore grows with the closest packed plane parallel to the non-closest packed (100) plane in the Si substrate. Figure 7 shows a SEM micrograph of the grown surface at 1050°C. The film is smooth except for occasional small elongated depressions in the surface. The reason for these features has not been determined; however, they may be due to pitting of the Si surface before AlN growth. These films were extremely smooth when compared to those grown by CVD [13-15].

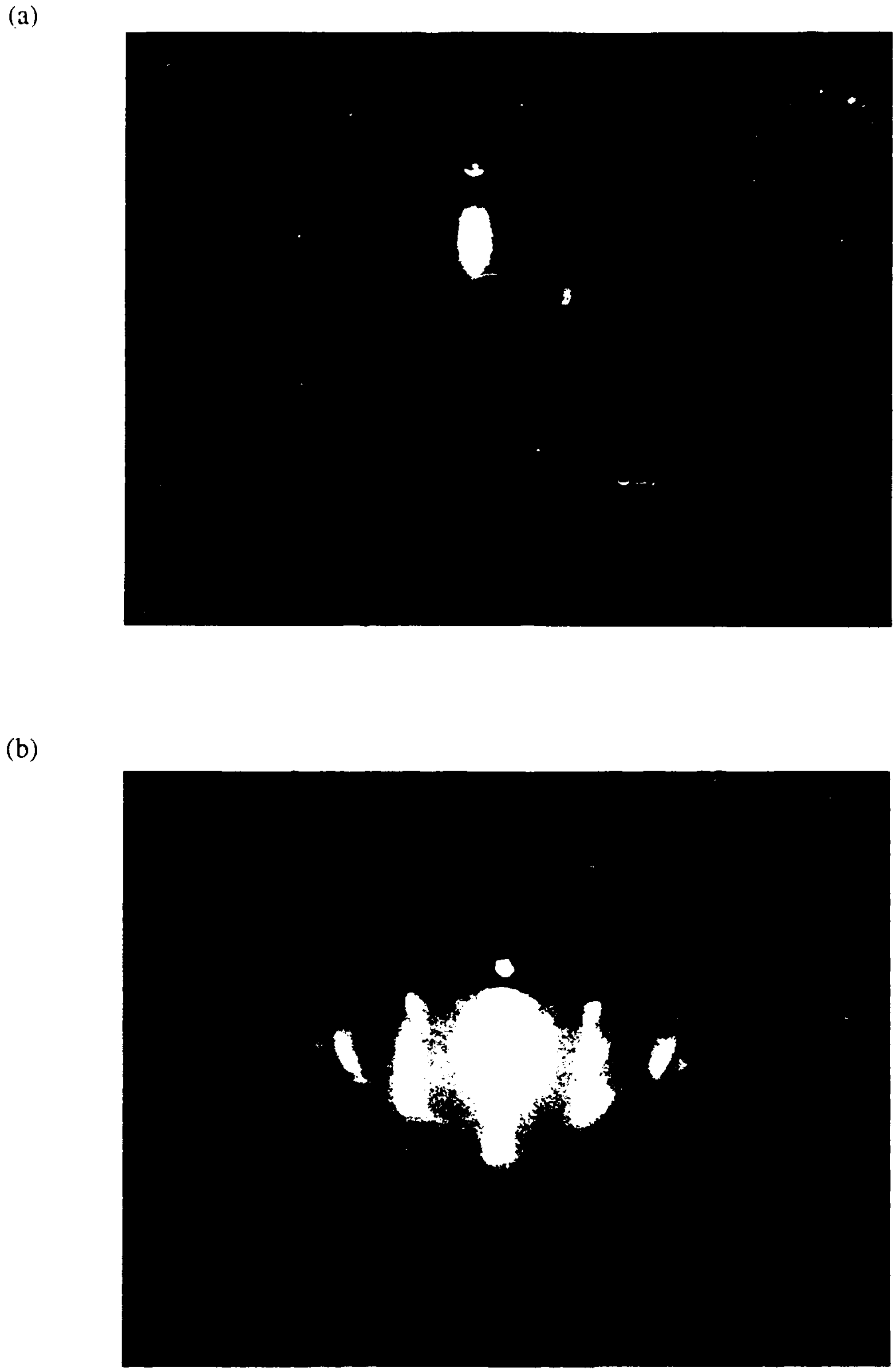

Figure 5. RHEED patterns ([11$\bar{2}$0] azimuth) of AlN films grown on vicinal Si(100) at (a) 900°C and (b) 1050°C.

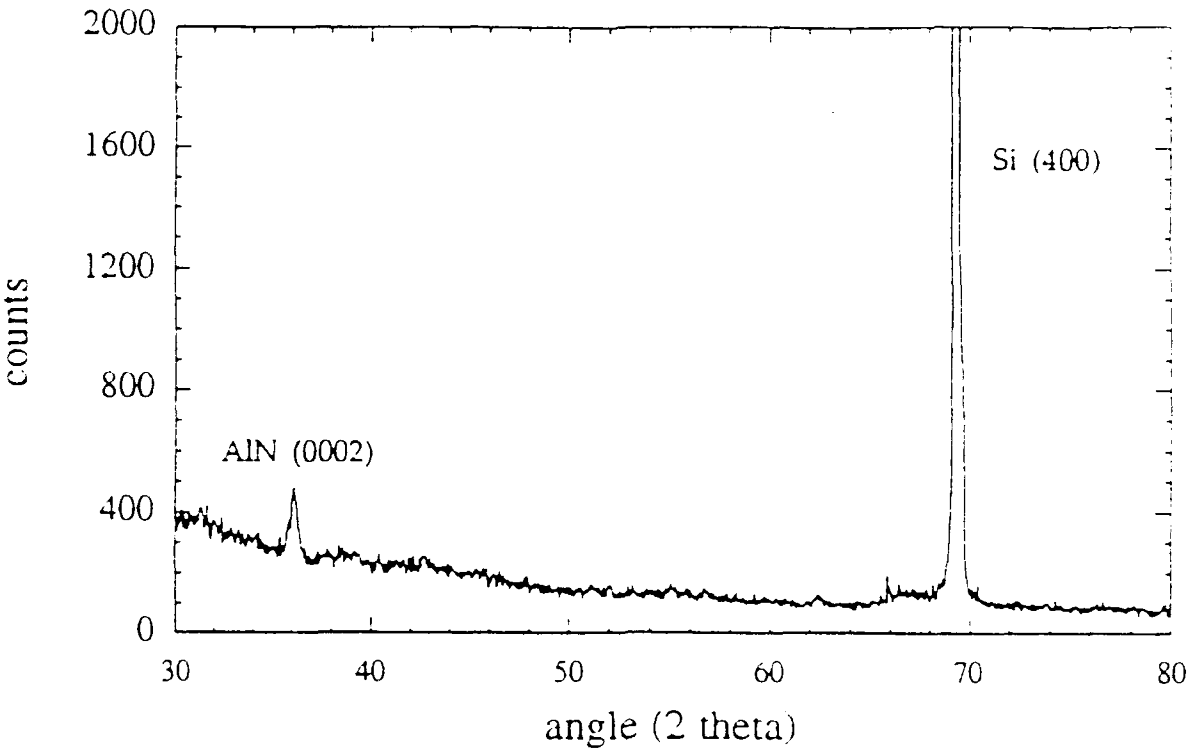

Figure 6. X-ray diffraction spectrum (CuKα) of AlN film on vicinal Si(100) at 1050°C.

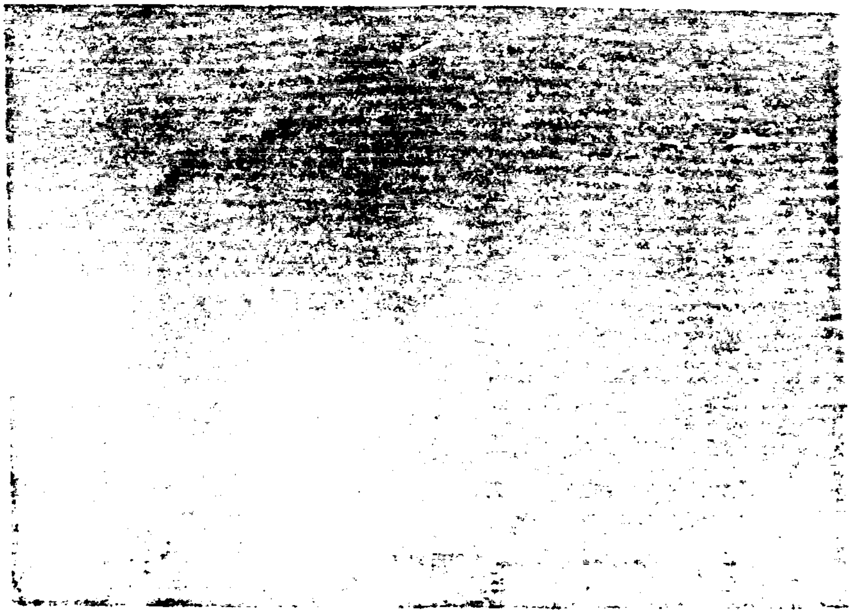

Figure 7. Scanning electron micrograph of surface morphology of AlN grown on vicinal Si(100) at 1050°C.

An orientation of AlN such as (10$\bar{1}$0) is more likely than (0001) on Si(100), based on crystallographic considerations. The latter orientation of AlN would be expected on Si (111), as the closest-packed (0001) planes of AlN contain the same general atomic arrangement. Previous reports of AlN on Si(100) are inconsistent with regard to orientational relationships. Several researchers have used trimethyaluminum and NH_3 in CVD growth on on-axis Si(100) substrates. Morita et al. [13] deposited single-crystal AlN(0001) on Si(100) at 1260°C. Yu et al. [14] grew epitaxial AlN(10$\bar{1}$0) on Si(100) at temperatures as low as 400°C. Roughening and pitting of the Si surface has been observed at temperatures as low as 800°C [24]. Thus, the roughness of the Si surface is likely to be more severe at 1260°C than at 400°C due to the evaporation of the oxide and the greater surface mobility at the higher temperature. This degradation of the surface may also explain why the films grown as a part of this study were AlN(0001) rather than AlN(10$\bar{1}$0).

In summary, monocrystalline AlN films were grown on vicinal α(6H)-SiC(0001) at 1050-1200°C using thermally evaporated Al and ECR plasma decomposition of N_2. The surfaces of the films formed at 1200°C were rough. Films grown at 1050°C were much smoother and formed an abrupt interface with the substrate. These latter films were of excellent microstructural quality when compared to those grown by CVD and reported in the literature. Highly oriented AlN(0001) films with a very smooth surface morphology were also formed on vicinal Si(100) at 1050°C. This c-axis alignment is believed to be caused by the roughness and pitting in the Si surface at the elevated growth temperatures. Doping with candidate n- and p-type impurities and the determination of the resultant properties of the AlN films will be investigated in the near future.

ACKNOWLEDGEMENTS

The authors acknowledge the support of this research by the Office of Naval Research under Grant #N00014-90-J-1427. We also express our appreciation to Applied Science and Technology (ASTeX), Inc., Woburn, MA for the ECR source, to Cree Research, Inc., Durham, NC for the vicinal α(6H)-SiC substrates, and to Ms. S. Rogers for the Auger analysis.

REFERENCES

1. W. M. Yim, E. J. Stofko, P. J. Zanzucchi, J. I. Pankove, M. Ettenberg, and S. L. Gilbert, J. Appl. Phys. **44**, 292 (1973).
2. M. G. Norton, B. C. H. Steele, and C. A. Leach, *Science of Ceramics*, **14**, 545 (1988).
3. G. A. Slack, J. Phys. Chem. Solids **34**, 321 (1973).
4. M. Kitayama, T. Fukui, T. Shiosaki, and A. Kawabata, Japan J. Appl. Phys. **22**, 139 (1982).
5. G. R. Kline and K. M. Lakin, Proc. IEEE Symp. Ultrasonics **14**, 495 (1983).

6. K. Tsubouchi, K. Sugai, and N. Mikoshiba, Proc. IEEE Symp. Ultrasonics **14**, 340 (1983).
7 M. Sano and M. Aoki, Oyo Butsuri, **52**, 374 (1983).
8. J. K. Liu, K. M. Lakin, and K. L. Wang, J. Appl. Phys **46**, 3703 (1975).
9. M. Morita, N. Uesugi, S. Isogai, K. Tsubouchi, and N. Mikoshiba, Jpn. J. Appl. Phys. **20**, 17 (1981).
10. G. D. O'Clock, Jr. and M. T. Duffy, Appl. Phys. Lett. **23**, 55 (1973).
11. T. L. Chu, D. W. Ing, and A. J. Norieka, Solid State Electron. **10**, 1023 (1967).
12. H. M. Manasevit, F. M. Erdmann, and W. I. Simpson, J. Electrochem. Soc. **118**, 1864 (1971).
13. M. Morita, S. Isogai, N. Shimizu, K. Tsubouchi, and N. Mikoshiba, Japan. J. Appl. Phys. **20**, L173 (1981).
14. Z. J. Yu, J. H. Edgar, A. U. Ahmed, and A. Rys, J. Electrochem. Soc. **138**, 196 (1991).
15. A. J. Noreika and D. W. Ing, J. Appl. Phys. **19**, 5578 (1968).
16. S. Yoshida, S. Mizawa, Y. Fujii, S. Takada, H. Hayakawa, S. Gonda, and A. Itoh, J. Vac. Sci. Technol. **16**, 990 (1979).
17. Z. Sitar, M. J. Paisley, B. Yan, R. F. Davis, J. Ruan, and J. W. Choyke, Thin Solid Films **200**, 311 (1991).
18. L. B. Rowland, R. S. Kern, S. Tanaka, and R. F. Davis, in *Proceedings of the Fourth International Conference on Amorphous and Crystalline Silicon Carbide* (Springer-Verlag, Berlin), to be published.
19. S. Kaneda, Y. Sakamoto, C. Nishi, M. Kanaya, and S. Hannai, Japan. J. Appl. Phys. **25**, 1307 (1986).
20. T. Sugii, T. Aoyama, and T. Ito, J. Electrochem. Soc. **137**, 989 (1990).
21. L. B. Rowland, R. S. Kern, S. Tanaka, and R. F. Davis, submitted for publication.
22. T. Yoshinobu, H. Mitsui, I. Izumikawa, T. Fuyuki, and H. Matusnami, Appl. Phys. Lett. **60**, 824 (1992).
23. D. J. Robbins, A. J. Pidduck, A. G. Cullis, N. G. Chew, R. W. Hardeman, D. B. Gasson, C. Pickering, A. C. Daw, M. Johnson, and R. Jones, J. Cryst. Growth **81**, 421 (1987).

IX. Low Temperature Growth of GaP by Gas-source Molecular Beam Epitaxy

A. Introduction

Low temperature GaAs grown by molecular beam epitaxy have received a great deal of attention as an alternative buffer layers to eliminate side gating effects in GaAs FET based integrated circuits [1], and as insulators for high power GaAs MISFETs [2]. However, little work has been reported on LT phosphorous based compounds, and the question was raised whether excess phosphorous and phosphorous precipitates can exist and exhibit similar properties as their arsenic counterpart. Previous efforts for LT InP did not yield semi-insulating films [3]. In this report, we will discuss the structural and electrical properties of LT GaP.

B. Experimental Procedure

The layers were grown using a Riber 32RD system. The GaP substrate (100) semi-insulating were degreased, then etched in $HCl:HNO_3:H_2O$, and were mounted on the Mo blocks with In-solder. Elemental Ga source and 100% PH_3 cracked at 900 °C were used to grow these films. The Growth rate was 1µm/h with an equivalent V/III beam ratio of 40 as estimated from a quadrupole mass analyzer. The growth chamber pressure was maintained in the 10^{-5} Torr range using a turbo-molecular pump.

Reflection high energy electron diffraction (RHEED), cross-sectional transmission electron microscopy (TEM), double crystal x-ray diffraction (DCXRD), and Raman spectroscopy were used to assess the crystal quality of the LT GaP films. The resistivity of these films were obtained from the van der Pauw technique.

The GaP substrate was heated at 630°C for few minutes under PH_3 over -pressure for oxide removal. Several approaches were then applied to the growth of these LT films. When films were grown for electrical characterizations, the substrate temperature was lowered directly to the desired low temperature followed by the growth of a LT GaP (~2µm). For structural evaluations, a GaP buffer Layer was grown first at 560 °C followed by LT film. GaP films were also grown at high temperature 560 °C as a reference for both the electrical and the structural characterizations. The annealing process of these LT GaP samples was carried out in a MOCVD reactor with PH_3 over-pressure at 650°C and 700°C for 30-60 minutes.

C. Results

LT GaP films grown at temperature lower than 160°C were polycrystalline as demonstrated by both the RHEED pattern and the TEM diffraction pattern. Increasing the growth temperature by ~30°C resulted in a streaky RHEED pattern and single crystal films, as confirmed by TEM.

Figure 1 shows a cross-sectionnal TEM dark field micrograph of multi-layers of GaP epitaxial films. This structure has a 0.4 µm GaP buffer layer grown at 560°C, followed by a LT GaP layer grown at about 210°C (1µm). The growth temperature was then decreased further by 20 °C without interrupting the growth to grow a second LT layer of the same thickness. All layers are single crystalline as indicated from the electron diffraction pattern. The LT films show a contrast from the one grown at high temperature which can be attributed to excess phosphorous in the lattice resulting from a deviation from stoichiometry.

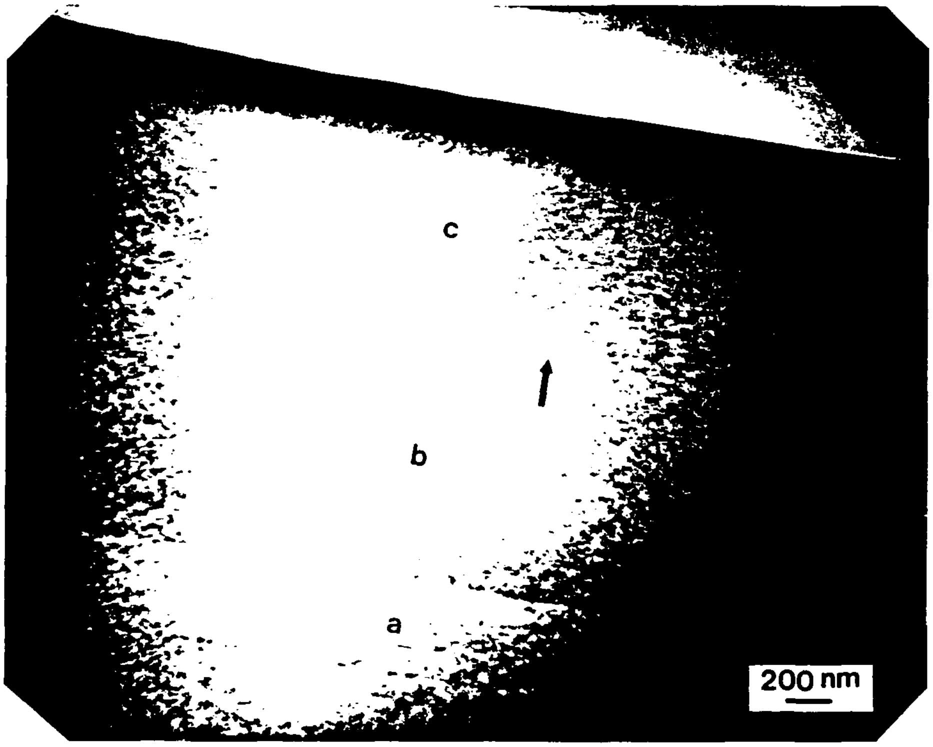

Figure 1. Cross-sectional TEM micrograph of a multi-layered structure containing: (a) GaP buffer layer grown at 560°C (HT), (b) LT GaP film (1µm) grown at 210°C, and (c) LT GaP (1µm) grown at 190°C. The arrow indicates the transition region between the two LT GaP films.

Using conventional imaging techniques, TEM studies on annealed samples did not show any incoherent phosphorous precipitation with defined boundaries. However, high-resolution TEM on the annealed films revealed the presence of of regions having different phase contrast which suggests coherent precipitation (Figure 2).

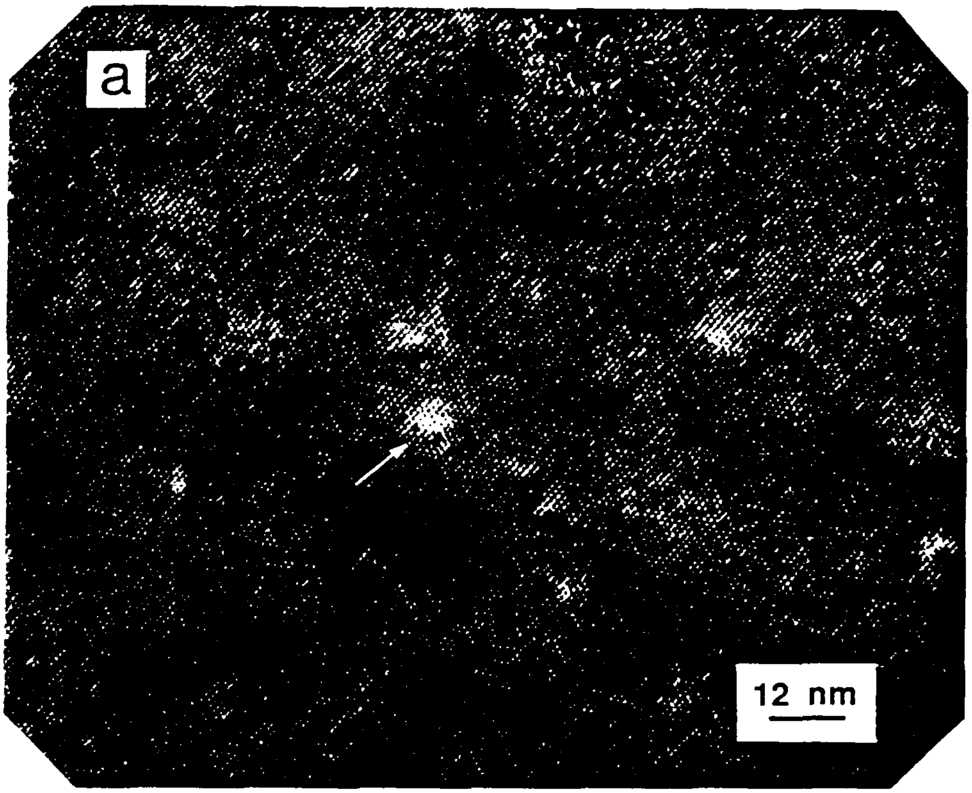

Figure 2. Cross-sectional TEM of annealed (650°C for 1 hour) LT GaP grown at 190°C (the arrow indicates one of the coherent precipitates as bright dots).

High-resolution x-ray diffraction results were obtained with a Bede 200 double crystal diffractometer. Films grown at high temperatures show only one diffraction peak from (113) reflection planes (Figure 3.a). For the LT growth, two (113) reflections were observed: a substrate reflection and an epilayer reflection with a lower intensity at a lower Bragg angle as indicated in figure 3.b. The angular separation ($\Delta\phi$) is about 220 arc seconds. Splitting as low as 40 arc seconds were also observed depending on the growth temperature. The splitting can be attributed to the strain in the epilayer resulting from excess phosphorous, possibly in the interstitial sites of the crystal lattice causing lattice dilatation. Annealing of these LT GaP films did not result in a complete disappearance of the lattice expansion; however, a slight reduction in the splitting of about 30 arc seconds was observed due to the high annealing temperature (Figure 3.c).

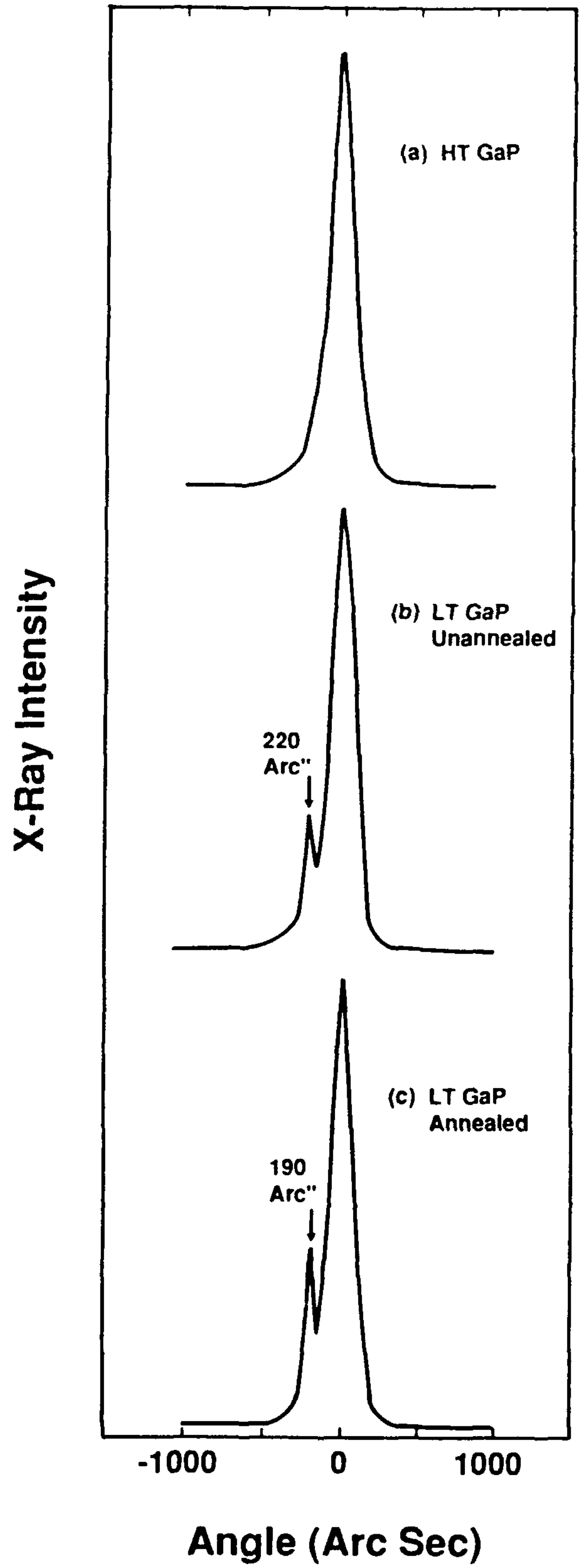

Figure 3. Double crystal x-ray diffraction from the (113) planes of: (a) HT GaP, (b) LT GaP, and (c) LT GaP annealed at 700°C for 60 minutes.

The Raman spectra were carried out in backscatter configuration at room temperature using the 457.9 nm line of an Ar^+ laser which was done in professor R. Nemanich's research laboratory. The Laser power was 250 mW, and the spot size was about 2mm x 100µm using a cylindrical lens. The signal was detected with a photomultiplier tube operated in photon counting mode. The spectrometer slit was set to 100µm corresponding to a resolution of $1.5cm^{-1}$. Both laser power and laser spot size were kept constant from run to run, and the Ar^+ plasma line was used for alignment.

Raman spectra are shown in Figure 4 for as-grown LT GaP, annealed LT GaP, and HT GaP. Only the LO phonon lines are plotted, the TO lines, with much weaker intensity, since they are not allowed in the (100) orientation , did not show any substantial frequency shift nor intensity variation which is an additional indication of good quality materials. On the other hand the LO phonons show a notable frequency shift. Table I lists the peak frequencies for the spectra in figure 4. For the as-grown LT GaP, the LO phonon peak downshifted by 0.7 cm^{-1} with respect to the HT GaP. After annealing the LO peak moved closer to the HT GaP peak. The reduction of LO-TO splitting of the as-grown LT GaP with respect to the LO-TO splitting for HT GaP is a result of a reduction of effective charge due to P_{Ga} antisite defect. After annealing the LO-TO splitting tends to match the LO-TO splitting of HT GaP which indicates a slight redistribution of excess phosphorous and formation of precipitates. These results are in agreement with DCXRD and TEM results.

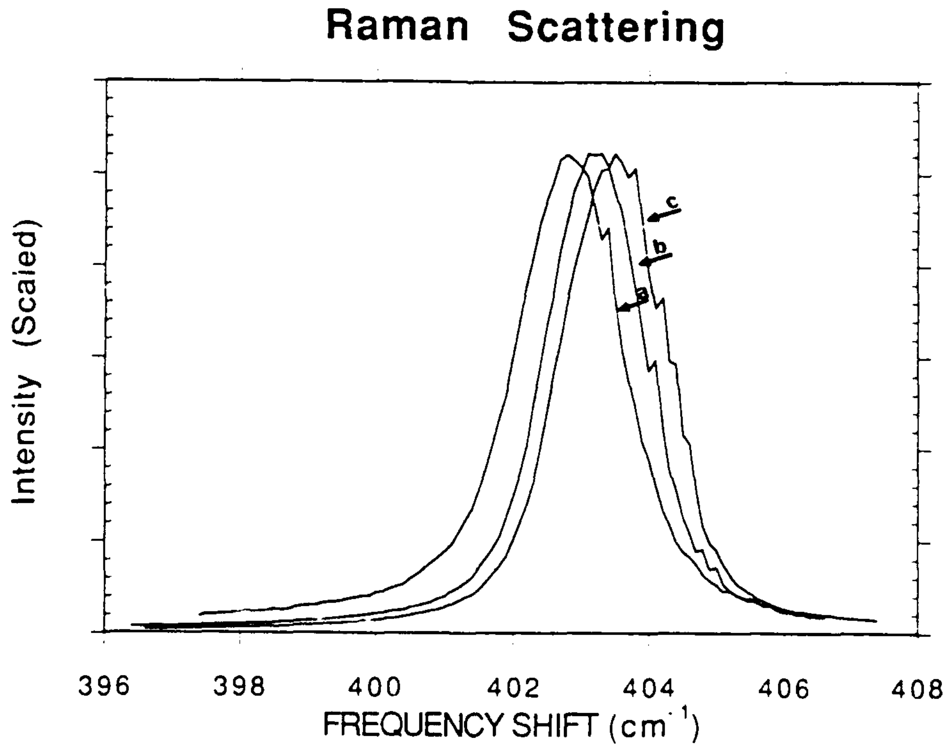

Figure 4. Raman spectra of: a) as-grown LT GaP, b) annealed LT GaP, and c) HT GaP.

Table I. LO Frequency Peak of the Raman Spectra in Figure 4.

Sample	LO frequency (cm^{-1})
as-grown LT GaP	402.8
Annealed LT GaP	403.2
HT GaP	403.5

Resistivity measurements were carried out using a high-impedance van der Pauw apparatus by professor D. Look, Wright State University. In-dots alloyed at 300°C were used as ohmic contacts to the epilayers.

The as-grown LT GaP (190°C) showed a resistivity of 10^8 Ω.cm. The resistivity of the sample after annealing at 700°C could not be measured in darkness, however, with intense light a resistivity of 10^6 Ω.cm was obtained. Other samples have shown resistivity in 10^6-10^8 Ω.cm range depending on the growth temperature.

D. Discussion

The structural results obtained on as-grown and annealed LT GaP show clearly a deviation from stoichiometry as a result of excess phosphorous present in these films. After annealing a slight redistribution of the excess phosphorous occurs along with a formation of coherent precipitates. Unlike LT GaAs, where a complete redistribution of excess arsenic to form incoherent precipitates at relatively lower annealing temperatures. These arsenic precipitates are mostly responsible for the semi-insulting properties of LT GaAs. On the other hand we believe that the resistivities obtained in LT GaP are mainly due to excess phosphorous related deep levels in present in these films.

E. Conclusion

The above preliminary studies show that LT GaP do not exactly follow the observed trends for LT GaAs films. Annealing the LT GaAs films caused lattice strain to disappear and arsenic precipitation, accompanied by high resistivity films. However, in LT GaP, annealing is not necessary to achieve high resistivity. the current GaP results imply that the high resistivity is not a result of the presence of precipitates and the accompanying carriers depletion near the metal phosphorous semiconductor interfaces as in the case of LT GaAs; but, rather is a result of deep levels associated with the excess phosphorous present in these LT GaP films.

F. Future Research Plans/Goals

The immediate plan is to use thin LT GaP films as passivation layers in GaAs based FETs in order to increase the breakdown voltage for power applications. This work could be extended to InP based FETs structures, where a thin LT GaP or LT GaInP could be used to enhance the Schottky barrier without using the conventional aluminum based ternary alloy.

G. References

1. F. W. Smith, A. R. Calawa, Chang-Lee. Chen, M. J. Manfra, and L. J. Mahoney, IEEE Electron Device Lett. **9** 77 (1988).
2. L. W. Yin, Y. Hwang, J. H. Lee, R. M. Kolbas, R. J. Trew, and U. K. Mishra, IEEE Electron Device Lett. **11** 12 (1990).
3. G. N. Maracas, K. T. Shiralagi, R. A. Puechner, F.Yu, K. T. Coi, J. S. Bow, R. Ramamurty, M.J. Kim, and R.W. Carpenter, Materials Research Society (MRS) Fall Meeting. Boston. December 1991.
4. A. C. Warren, J. M. Woodall, J .L. Freeouf, D. Grischjkowsky, D. T. McInturff, M. R. Melloch, and N. Otsuka, Appl. Phys. Lett. **57** 13 (1990).

X. Deposition of GaN by Atomic Layer Epitaxy—Davis Group

A. Introduction

Atomic layer epitaxy (ALE) is the sequential chemisorption of one or more elemental species or complexes within a time period or chemical environment in which only one monolayer of each species is chemisorbed on the surface of the growing film in each period of the sequence. The excess of a given reactant which is in the gas phase or only physisorbed is purged from the substrate surface region before this surface is exposed to a subsequent reaction. This latter reactant chemisorbs and undergoes reaction with the first reactant on the substrate surface resulting in the formation of a solid film. There are essentially two types of ALE which, for convenience, shall be called Type I and Type II.

In its early development in Finland, the Type I growth scenario frequently involved the deposition of more than one monolayer of a given species. However, at that time, ALE was consided possible only in those materials wherein the bond energies between like metal species and like nonmetal species were each less than that of the metal-nonmetal combination. Thus, even if multiple monolayers of a given element were produced, the material in excess of one monolayer could be sublimed by increasing the temperature and/or waiting for a sufficient period of time under vacuum. Under these chemical constraints, materials such as GaAs were initially thought to be improbable since the Ga-Ga bond strength exceeds that of the GaAs bond strength. However, the self-limiting layer-by-layer deposition of this material proved to be an early example of Type II ALE wherein the trimethylgallium (TMG) chemisorbed to the growing surface and effectively prevented additional adsorption of the incoming metalorganic molecules. The introduction of As, however caused an exchange with the chemisorbed TMG such that a gaseous side product was removed from the growing surface. Two alternating molecular species are also frequently used such that chemisorption of each species occurs sequentially and is accompanied by extraction, adstraction and exchange reactions to produce self-limiting layer-by-layer growth of an element , solid solution or a compound.

The Type II approach has been used primarily for growth of II-VI compounds [1-13]; however, recent studies have shown that it is also applicable for oxides [14-18], nitrides [19], III-V GaAs-based semiconductors [20-33] and silicon [34-36]. The advantages of ALE include monolayer deposition control, growth of abrupt p-n junction interfaces, growth of uniform and graded solid solutions with controlled compositions, reduction in macroscopic defects and uniform coverage over large areas. A commercial application which makes use of the last attribute is large area electroluminescent displays produced from II-VI materials. Two comprehensive reviews [37,6], one limited overview [38] and a book [39] devoted entirely to the subject of ALE have recently been published.

The potential semiconductor and optoelectronic applications of III-V nitrides has prompted significant research in thin film growth and development. The materials of concern in this section are GaN, currently, and other III-V nitrides, for future studies. Because GaN in the wurtzite structure with a bandgap of 3.4 eV [40] forms continuous solid solutions with both AlN and InN, for example, which have bandgaps of 6.2 eV [41] and 1.9 eV [42], respectively, engineered bandgap materials could result in optoelectronic devices active from the visible to deep UV frequencies [43].

To produce the desired nitride films, the ALE deposition technique has been implemented. The equipment and procedures used in the current ALE deposition of GaN will be discussed here. The results to date, conclusions and plans for future work are also included.

B. Experimental Procedure

Substrate Cleaning. The appropriate substrate cleaning technique is obviously dependent on the type of substrate being used for ALE deposition. Table I lists some substrate types and their compatible cleaning requirements used during this research. The exact crystal orientation of the substrates used can be found in Table II.

Table I. Substrate Cleaning Techniques

Substrate	Cleaning Technique
Si wafer	Modified RCA procedure
Oxidized SiC wafer	20% HF (10min), then 10% HF (5min)
Other SiC wafer	Modified RCA procedure

Modified RCA procedure: 10min @ 70°C NH_4OH: H_2O_2: DI H_2O (1:1:5 ratios); then DI H_2O rinse; then 10min @ 70°C HCl: H_2O_2: DI H_2O (1:1:5 ratios); then DI H_2O rinse; then 5min 10%HF

Deposition Procedure. Initially, the substrate is loaded onto the SiC-coated, graphite susceptor with variable speed adjustment. The susceptor should be raised to its deposition height in the reactor chamber, approximately one inch below the gas inlet lines. High vacuum conditions of ~ 5×10^{-6} Torr are reached in the chamber before starting depostion.

The ALE reactor design utilizes a continuously rotating susceptor arrangement (Figure 1). Thus, from the diagram, as the susceptor rotates, the substrate is alternately exposed to the metalorganic (MO) gas, the H_2 curtain gas, and the nitrogen source gas (ammonia - NH_3) in a constant cycle. The preference of an organometallic Ga source over a chloride source resulted from higher purity material being available and the fact that transport of the Ga species is easier with metalorganics [43]. For the GaN growth, triethylgallium (TEG) was chosen over trimethylgallium (TMG) because of its lower decomposition temperature range [44].

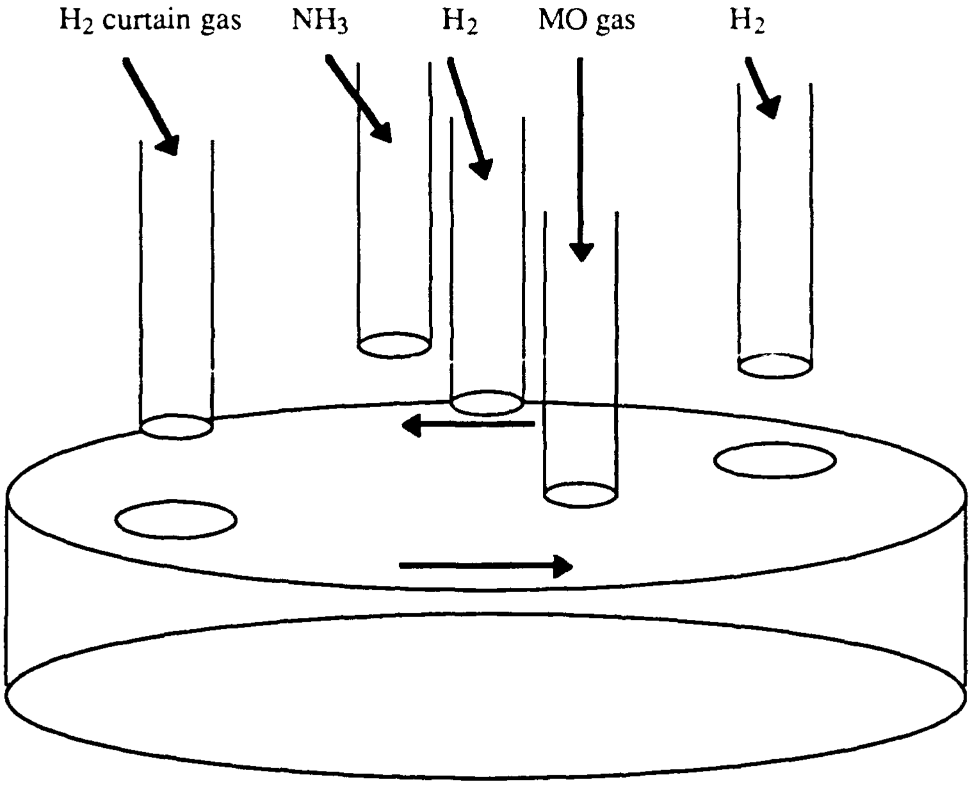

Figure 1. Susceptor design.

Mass Flow Meters and compatible Mass Flow Controllers are utilized to regulate the flow of all gases into the reactor chamber. Once these devices are flowing the setpoint levels of gases and the RF induction heating coils have stabilized the susceptor at the prescribed deposition temperature, rotation of the susceptor can begin. This rotation should begin from under the H_2 inlet line before the MO inlet line. Before the substrate sweeps under the H_2 line after the MO line, the W-filament used in cracking the ammonia into elemental hydrogen and nitrogen should be stabilized at the desired "cracking" temperature.

Once rotation and thus deposition begins, several system variables must be monitored. They include cooling water flow, all gas flow rates, system and MO bubbler pressures, susceptor and W-filament temperatures, and rotation. Under normal operating procedures, these variables remain nearly constant, but because of their obvious importance, they must be monitored to maintain deposition uniformity. Table II below lists the various system variables for each ALE run attempted.

Table II. Deposition Variables

System Variables	Run # #1	#2	#3	#4	#5
Substrate	Si *	Si *	Si *	SiC **	SiC **
Initial Press.	1×10^{-5} Torr	1×10^{-5}	6×10^{-6}	6×10^{-6}	5×10^{-6}
Run Pressure	3.8-4.1 Torr	3.8-3.9	4.0-4.3	4.1-4.3	4.0-4.3
Bubbler Temp.	74.0°F	69.6	69.6	69.6	61.0
Bubbler Press.	~ 530 Torr	~ 750	~ 750	~ 750	~750
TEG Part. Press.***	5.36 Torr	4.65	4.65	4.65	3.49
H_2 flow	~ 325 sccm	~ 325	~ 325	~ 325	~ 325
NH_3 flow	100 sccm	100	100	100	100
H_2 carrier gas flow	30 sccm	28	28	28	28
TEG flow ***	0.306 sccm	0.175	0.175	0.175	0.131
W-filament Temp.	1410°C	1420	1460	1475	1475
Susceptor Temp.	658°C	636	637	637	637
rpm's	0.4 *rpm*	0.44	1.0	1.0	1.0
Run Time	90 minutes	130	180	150	150

* Si (100) 3° off-axis toward [011]

** α(6H)-SiC (0001) 3° off-axis toward $[11\bar{2}0]$

*** See equations below for calculation of these values

C. Results

Initially, in Run #1 only a predominantly gallium metal film was deposited with a visibly rough surface texture. For Run #2, the parameters were adjusted (see Table II) to reduce the flow of TEG into the reactor chamber. The resulting film when analyzed using reflected high energy electron diffraction (RHEED) appeared to be highly non-oriented polycrystalline GaN with , once again, a rough surface area. In Run #3 the rotation speed was increased to reduce the exposure time of the substrate to the gallium source gas. Visible surface roughness decreased only slightly. Also, RHEED only revealed ring patterns but no spots, indicating growth of polycrystalline material. For Run #4, a SiC substrate was used keeping all other variables constant. Using RHEED, spot patterns (an indication of a monocrystalline structure) resulted, but no Kikuchi lines were present. In Run #5 a SiC substrate was used, but the partial pressure of TEG in the bubbler was reduced by 25% to lessen the amount of TEG entering the reactor from 0.175 sccm to 0.131 sccm. The deposited film, using RHEED, showed sharp diffraction spots but still no Kikuchi lines (Figure 2). But ultimately, layer-by-layer deposition of monocrystalline GaN on SiC has been achieved.

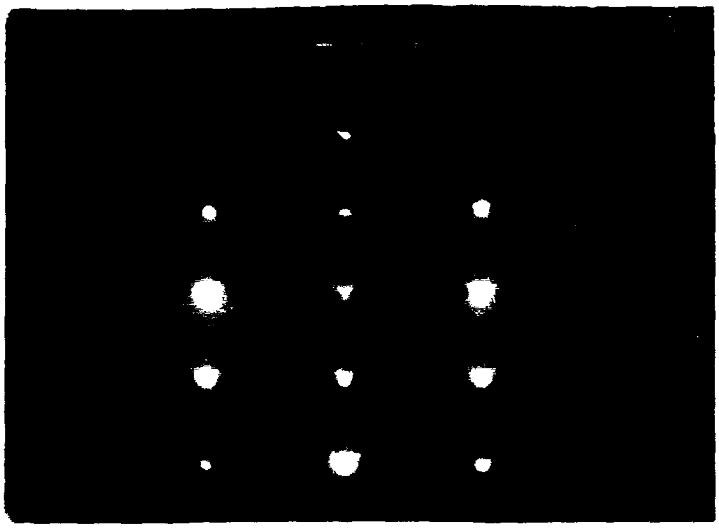

$(2\bar{1}\bar{1}0)$ Reflection

Figure 2. RHEED pattern for GaN deposited on α(6H)-SiC at 637°C.

D. Discussion

The gallium metal deposited during Run #1 was the resultant of excessive TEG entering the reactor. Note from Table II the higher bubbler temperature, higher TEG partial pressure and lower total bubbler pressure yielding this result. TEG levels were subsequently reduced in Run #2 by decreasing the bubbler temperature (i.e. reducing TEG partial pressure) and increasing bubbler pressure. The following equations were used to predict the partial pressure of TEG and its actual flow rate into the reactor chamber.

$\log P(TEG) = 8.224 - 2222/T(Bubbler)$

$F(TEG) = \{F(H_2) \times P(TEG)\}/\{P(Bubbler)-P(TEG)\}$

where: P(TEG) = partial pressure of TEG in Torr
T(Bubbler) = Bubbler temperature in Kelvin
F(TEG) = TEG flow rate in sccm
$F(H_2)$ = H_2 carrier gas flow rate in sccm
P(Bubbler) = Bubbler pressure in Torr

TEG concentrations were further reduced in Run #3 by increasing the rotation speed. It was concluded that reducing the TEG levels aided in producing polycrystalline GaN, but a rough surface texture continued. The lattice and coefficient of thermal expansion mismatches between the substrate, Si (100), and the GaN film contributed to the polycrystalline growth in Runs #2 and #3. These differences are shown in Table III. For Runs #4 and #5 the substrate used was SiC. The more compatible lattice and coefficient of thermal expansion values aided in the monocrystalline growth of GaN as revealed by RHEED. However, it is apparent that the Ga is not being deposited in a self-limiting manner, but rather by a layer-by-layer mechanism. It is believed that the rough surface on the deposited films may be "pools" of excess Ga or small island nucleations of GaN on the surface. Scanning electron microscopy (SEM) will be utilizes to determine the exact nature of the surface roughness. Slightly excessive concentrations of Ga are still thought to be entering the reactor.

Table III. Physical properties of GaN and potential substrate material [45]

Material	Lattice parameter a (Å)	c (Å)	Coefficient of thermal expansion (K^{-1})
GaN	3.189	5.185	5.59×10^{-6} 3.17×10^{-6}
Si	5.43		3.59×10^{-6}
α(6H)-SiC	3.08	15.12	4.2×10^{-6} 4.7×10^{-6}

E. Conclusions

The effects of reducing the concentration of TEG entering the reactor chamber reveal that deposition does not occur in a self-limiting manner, but rather in a layer-by-layer mechanism.

Thus, it is believed that layer-by-layer deposition resulting in monocrystalline GaN has been achieved using the described deposition procedure. Further analysis will determine the quality of the films deposited.

F. Future Research Plans/Goals

Existing films will be further analyzed to determine the nature of the surface roughness. Also, determination of the defect density using Transmission electron microscopy (TEM) has not yet been achieved. The stoichiometry of the GaN needs to be investigated to reveal the compositions of the deposited films. Thus, the input levels of the reactant species can be properly controlled to create the best stoichiometric films. Also, because there is growth per cycle instead of a traditional growth rate, the rotation speed of the susceptor should be increase to quicken the layer-by-layer deposition process. Film depth versus rotational time correlations must be obtained to verify a true layer-by-layer process. Once monocrystalline GaN can be grown repetitively, attempts will be made to deposit different III-V nitride films in layers and finally in continuous solid solutions.

G. References

1. T. Suntola and J. Antson, U.S. Patent 4,058,430 (1977).
2. M. Ahonen, M. Pessa and T. Suntola, *Thin Solid Films,* **65**, 301 (1980).
3. M. Pessa, R. Makela and T. Suntola, *Appl. Phys. Lett.,* **38**, 131 (1981).
4. T. Yao and T. Takeda, *Appl. Phys. Lett.,* **48**, 160 (1986).
5. T. Yao, T. Takeda and T. Watanuki, *Appl. Phys. Lett.,* **48**, 1615 (1986).
6. T. Yao, *Jpn. J. Appl. Phys.,* **25,** L544 (1986).
7. T. Yao and T. Takeda, *J. Cryst. Growth,* **81**, 43, (1987).
8. M. Pessa, P. Huttunen and M.A. Herman, *J. Appl. Phys.,* **54**, 6047 (1983).
9. C.H.L. Goodman and M.V. Pessa, *J. Appl. Phys.,* **60**, R65 (1986).
10. M.A. Herman, M. Valli and M. Pessa, *J. Cryst. Growth,* **73**, 403 (1985).
11. V.P. Tanninen, M. Oikkonen and T. Tuomi, *Phys. Status Solidi,* **A67**, 573 (1981).
12. V.P. Tanninen, M. Oikkonen and T. Tuomi, *Thin Solid Films,* **90**, 283 (1983).
13. D. Theis, H. Oppolzer, G. Etchinghaus and S. Schild, *J. Cryst. Growth,* **63**, 47 (1983).
14. S. Lin, *J. Electrochm. Soc.,* **122,** 1405 (1975).
15. H. Antson, M. Leskela, L. Niinisto, E. Nykanen and M. Tammenmaa, Kem.-Kemi, **12**, 11 (1985).
16. R. Tornqvist, Ref. 57 in the bibliography of Chapt. 1 of Ref. 39 of this section.
17. M. Ylilammi, M. Sc. Thesis, *Helsinki Univ. of Technology,* Espoo (1979).
18. L. Hiltunen, M. Leaskela, M. Makela, L. Niinisto, E. Nykanen and P. Soininen, *Surface Coating and Technology,* in press.
19. I. Suni, Ref. 66 in the bibliography of Chapt. 1 of Ref. 39 in this section.
20. S.M. Bedair, M.A. Tischler, T. Katsuyama and N.A. El-Masry, *Appl. Phys. Lett.,* **47**, 51 (1985).
21. M.A. Tischler and S M. Bedair, **48**, 1681 (1986).
22. M.A. Tischler and S.M. Bedair, *J. Cryst. Growth,* **77**, 89 (1986).
23. M.A. Tischler, N.G. Anderson and S.M. Bedair, *Appl. Phys. Lett.,* **49**, 1199 (1986).
24. M.A. Tischler, N.G. Anderson, R.M.Kolbas and S.M. Bedair, *Appl. Phys. Lett.,* **50**, 1266 (1987).

25. B.T. McDermott, N.A. El-Masry, M.A. Tischler and S.M. Bedair, *Appl. Phys. Lett.*, **51**, 1830 (1987).
26. M.A. Tischler, N.G. Anderson, R.M. Kolbas and S.M. Bedair, *SPIE Growth Comp. Semicond.*, **796**, 170 (1987).
27. S.M. Bedair in *Compound Semiconductor Growth Processing and Devices for the 1990's,* Gainesville, FL, 137 (1987).
28. J. Nishizawa, H. Abe and T. Kurabayashi, *J. Electrochem. Soc.*, **132**, 1197 (1985).
29. M. Nishizawa, T. Kurabayashi, H. Abe, and N. Sakurai, *J. Electrochem. Soc.*, **134**, 945 (1987).
30. P. D. Dapkus in Ref. 27, p. 95.
31. S.P. Denbaars, C.A. Beyler, A. Hariz and P.D. Dapkus, *Appl. Phys. Lett.*, **51**, 1530 (1987).
32. M. Razeghi, Ph. Maurel, F. Omnes and J. Nagle, *Appl. Phys. Lett.*, **51**, 2216 (1987).
33. M. Ozeki, K. Mochizuki, N. Ohtsuka and K. Kodama, *J. Vac. Sci. Technol.*, **B5**, 1184 (1987).
34. Y. Suda, D. Lubben, T. Motooka and J. Greene, *J. Vac. Sci. Technol.*, **B7**, 1171 (1989).
35. J. Nishizawa, K. Aoki, S. Suzuki and K. Kikuchi, *J. Cryst. Growth*, **99**, 502 (1990).
36. T. Tanaka, T. Fukuda, Y. Nagasawa, S. Miyazaki and M. Hirose, *Appl. Phys. Lett.*, **56**, 1445 (1990).
37. T. Suntola and J. Hyvarinen, *Ann. Rev. Mater. Sci.*, **25**, 177 (1985).
38. M. Simpson and P. Smith, *Chem. Brit.*, **23**, 37 (1987).
39. T. Suntola and M. Simpson, *Atomic Layer Epitaxy*, Chapman and Hall, New York, 1990.
40. H.P. Maruska and J.J. Tietjen, *Appl. Phys. Lett.*, **15**, 327 (1969).
41. W.M. Yim, E.J. Stofko, P.J. Zanzucchi, J.I. Pankove, M. Ettenberg and S.L. Gilbert, *J. Appl. Phys.*, **44**, 292 (1973).
42. J.A. Sajurjo, E. Lopez-Cruz, P.Vogh and M.Cardona, *Phys. Rev.*, **B28**, 4579 (1983).
43. J. Sumakeris, Z. Sitar, K.S. Ailey-Trent, K.L. More and R.F. Davis, *Thin Solid Films*, in press.
44. N. Kobayashi, T. Makimoto, and Y. Horikoshi, *Jpn. J. Appl. Phys.*, **24**, L962 (1985).
45. *Landolt-Bornsteinn*, Vol. 17, Springer, New York, 1982.

XI. Atomic Layer Epitaxy of GaN—Bedair Group

A. Introduction

GaN is a very important and promising material for high efficiency optoelectronic devices due to its direct band gap corresponding to radiation in the near UV range. Possible applications include UV and blue semiconductor lasers, LED's, and detectors [1]. Atomic layer epitaxy of GaN will be useful in reducing the single crystal epitaxy temperature, which will improve the heteroepitaxy quality [2].

B. Experimental Procedure

Epitaxial single crystal GaN has been grown recently by numerous methods. Sapphire (0001) has been the substrate of choice due to its thermal stability and commercial availability. To reduce the effect of the large lattice mismatch between GaN and sapphire, AlN has been effectively used as a buffer layer by several researchers [3].

The growth system which will be employed for ALE of GaN has been used successfully for the growth of many III-V semiconductors. This atmospheric pressure MOCVD system uses a rotating susceptor design to produce ALE growth. The precursers for this study will be trimethylgallium (TMGa), ammonia (NH_3), and triethlyaluminum (TEAl) for the buffer layer growth. Growth temperatures are expected to be greater than 700°C, and an additional source may be added for cracking the NH_3 such as a heated tungsten filament or an excimer laser to lower the process temperature. Fast susceptor rotating speeds will be used to obtain high growth rates with the benefits of controlled growth that ALE provides.

C. Results

Present work for the project has been centered on modifying the system that will be used for this investigation. Modifications will include the introduction of purified ammonia into the growth system, which requires the installation of an ammonia purifier and a mass flow controller as well as replacing many of the seals throughout the system's components to make them compatible with ammonia. In addition, the susceptor design that has been previously used has been modified. The susceptor and gas manifold have been designed to allow either ALE or MOCVD growth to compare these two processes.

D. Conclusion

The system for ALE growth of GaN is currently undergoing modifications and will be functional at the beginning of 1993.

E. Plans for Future Work

Immediate plans include finishing the system modifications and starting initial experiments with MOCVD and ALE deposition of GaN with AlN buffer layers.

F. References

1. J. H. Edgar, J. Mater. Res., **7**, 235 (1992).
2. M. Asif Khan, R. A. Skogman, J. M. Van Hove, D. T. Olson, and J. N. Kuznia, Appl. Phys. Lett., **60**, 1366 (1992).
3. S. Strite and H. Morkoc, J. Vac. Sci Technol. B, **10**, 1237 (1992).

XII. Growth and Characterization of SiGe Contacts on Semiconducting Diamond Substrates

T. P. Humphreys, P. K. Baumann, K. F. Turner and R. J. Nemanich
Department of Physics, North Carolina State University, Raleigh, North Carolina 27695-8202 USA.

K. Das
Kobe Steel Inc., Electronic Materials Center, P. O. Box 13608, Research Triangle Park, North Carolina 27709 USA.

R. G. Alley, D. P. Malta and J. B. Posthill
Research Triangle Institute, Research Triangle Park, North Carolina 27709-2194 USA.

Abstract

SiGe films have been grown by electron-beam deposition on semiconducting diamond C(001) substrates in UHV. As evidenced by STM the surface morphology is highly textured corresponding to the presence of small polycrystalline grains. Current-voltage (I-V) measurements conducted at room temperature have demonstrated rectifying characteristics. Moreover, it has been shown that the SiGe contacts are thermally unstable and exhibit an ohmic-like behavior on heating to a temperature of 400°C.

A. Introduction

At present, there is a significant scientific and technological interest in the fabrication of stable ohmic and high-temperature rectifying contacts on diamond[1, 2]. To date, several metals,[3,4] refractory metal silicides[5] and semiconductors[6] have been investigated as appropriate contact materials to semiconducting diamond substrates. In particular, it has been recently demonstrated by Venkatesan et al.[6] that highly doped polycrystalline p-Si (B doped) and n-Si (As or P doped) contacts fabricated on semiconducting diamond substrates are rectifying at room temperature and at 400 °C. Furthermore, the Si / diamond heterostructure also affords the potential of fabricating novel heterojunction devices which can be integrated with existing Si-based processing technologies.

In this study we report the first results pertaining to the growth and characterization of SiGe contacts deposited on semiconducting natural diamond substrates.

B. Experimental Results

Commercially supplied (D. Drucker & ZN.N.V) low-resitivity (~ 10^4 $\Omega \cdot$cm, p-type) semiconducting natural diamond (surface orientation (001)) substrates were chemically cleaned. The cleaning procedure included boiling CrO_3+H_2SO_4 (heated to 200°C) for 10 min followed by immersion in aqua regia ($3HCl + 1HNO_3$) and standard RCA cleaning solutions. Following cleaning, the samples were mounted on a Mo sample holder and transferred into the electron-beam evaporation chamber. The base pressure in the system was typically 2×10^{-10} Torr. Prior to deposition, the substrates were heated to 550°C for 5 minutes to thermally desorb both water vapor and possibly physi-adsorbed gas contaminants. On cooling to room temperature an unreconstructed (1×1) low energy electron diffraction (LEED) pattern was observed from the C(001) surface. By employing a stainless steel shadow mask several SiGe dots of ~200 nm in thickness and 3×10^{-3} cm^2 in area were fabricated. The substrate temperature was maintained at 550 °C during deposition. Corresponding Si and Ge fluxes were calibrated to obtain SiGe layers with a 5% Ge composition.

C. Results and Discussion

Examination of the as-grown films by LEED failed to obtain an ordered surface structure. Indeed, an inspection of the SiGe films by *ex-situ* scanning tunneling microscopy (STM) showed a highly textured surface morphology which indicated that the deposited layers were polycrystalline as shown in Figure 1. The STM image was obtained in the constant current mode with a tip bias of 2 V. The presence of small polycrystalline grains of ~100 nm is clearly evident. The corresponding rms surface roughness of the deposited layer has been determined to be ~ 5 nm.

Raman spectroscopy measurements of the SiGe films obtained at room temperature showed two distinct phonon peaks pertaining to Si and Ge at 518 cm^{-1} and 300 cm^{-1}, respectively. It is interesting to note that the corresponding SiGe phonon mode, indicative of alloy formation (near 400 cm^{-1}) was not observed. The absence of the SiGe phonon mode would tend to suggest an apparent segregation and clustering of Si and Ge during growth. Differences in the Si and Ge surface mobilities and/or surface energies on the chemically cleaned diamond C(001) surface during the initial stages of growth may account for this behavior. Further studies are currently in progress to study this growth phenomena.

Current-voltage (I-V) measurements were obtained by mounting the diamond substrates on a Cu plate using Ag paint to form a large area back contact and applying a bias to the SiGe contact using a W probe. The room temperature I-V characteristics obtained for the SiGe contacts on semiconducting diamond are shown in Figure 2. The rectifying character of the SiGe film is clearly evident. From the I-V measurements a small forward bias turn-on voltage of ~ 0.6 V was estimated. The corresponding reverse bias leakage current density was measured to be ~1.56×10^{-6} A / cm^2 at 20 V. Moreover, from the apparently linear region of the semilogarithmic plot of the forward characteristics an ideality factor n of 2.5 was calculated. This high n value may be an indication that the current conduction at the SiGe/diamond interface is not governed by a thermionic emission mechanism. It is interesting

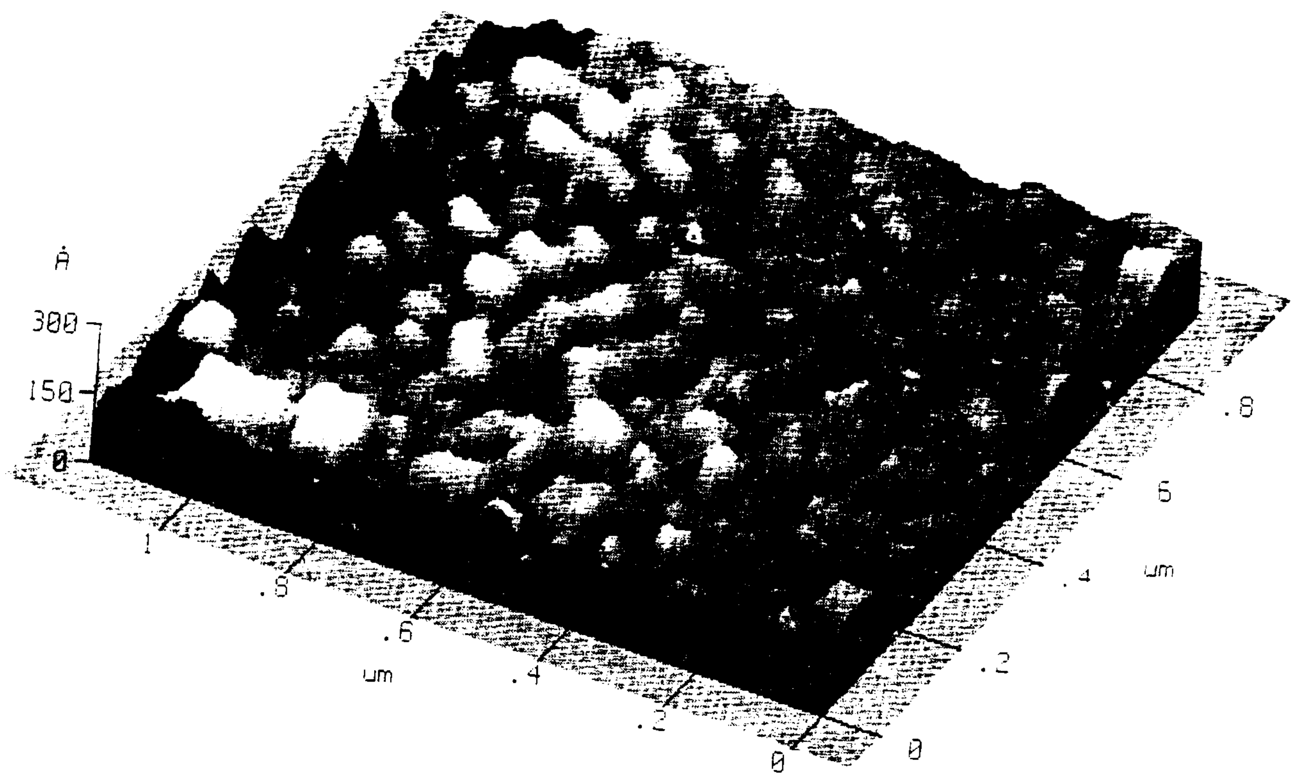

Figure 1. Topographic (constant current) STM micrograph of the surface morphology of the SiGe film deposited on natural C(001) substrates.

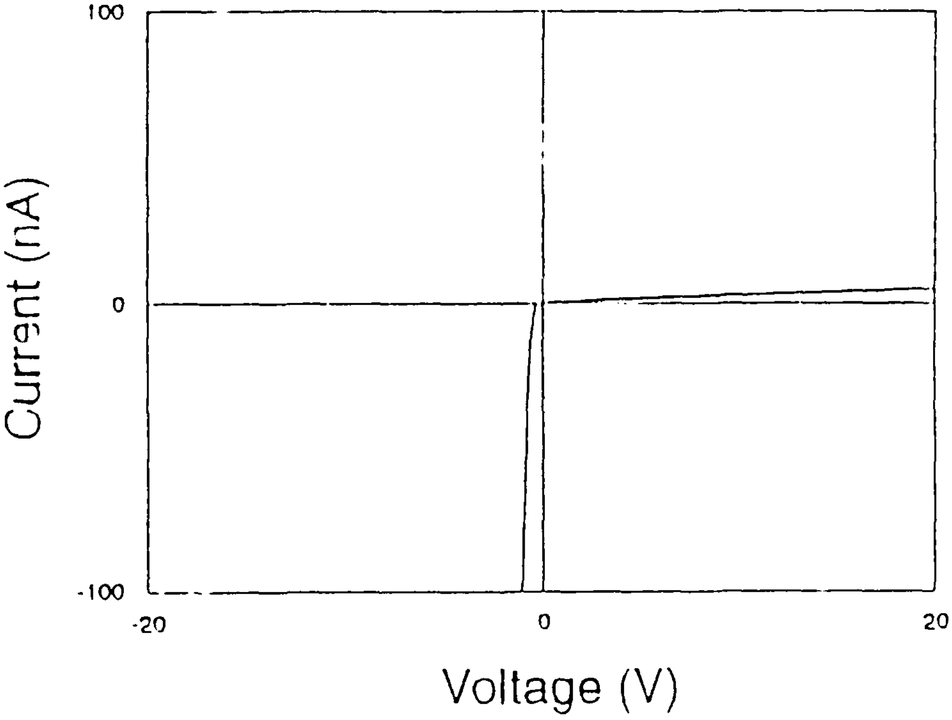

Figure 2. Linear plot of the current-voltage (I-V) characteristics of the SiGe contacts on semiconducting C(001) substrates. Measurements were conducted at 25°C.

to note that similar observations have also been reported for Ni, $TiSi_2$ and Si contacts on semiconducting diamond C(001) substrates [5,6]. In each of these studies current conduction appeared to be dominated by a space charge limited current (SCLC) mechanism. Consistent with the small turn-on voltage and the relatively high reverse leakage current, the corresponding I-V measurements recorded at 400 °C exhibit ohmic-like behavior.

D. Conclusions

In summary SiGe films have been grown by the co-deposition of Si and Ge on natural single crystal diamond C(001) substrates. As evidenced by LEED and STM analysis, the as-deposited films are polycrystalline. The I-V measurements of the SiGe contacts on semiconducting diamond have demonstrated rectifying characteristics at room temperature. However, for measurements conducted at 400oC the I-V characteristics exhibit ohmic-like behavior.

E. Future Resarch Plans

Investigate the thermal stability of the SiGe contacts and explore the interface chemistry. Optimize the growth conditions to achieve epitaxial film growth. Measurement of the bandgap offset between the SiGe contacts and the single crystal diamond substrate utilizing UPS.

Acknowledgements

TPH and RJN gratefully acknowledge partial support from the Office of Naval Research (Contract No. N00014-92-J-1477) and Kobe Research Laboratories, USA. TPH, RJN, RGA, DPM and JBP acknowledges support from the Strategic Defense Initiative Organization / Innovative Science and Technology through the office of Naval Research (Contract No. N00014-92-C-0081).

E. References

1. M. W. Geis, N. N. Efremow and D. D. Rathman, J.Vac. Sci. Technolol. **6**, 1953 (1988).
2. For a review see K.Das, V. Venkatesan, K Miyata and D. L. Dreifus, Thin Solid Films. **212**, 19 (1992).
3. T. P. Humphreys, J. V. LaBrasca, R. J. Nemanich, K.Das and J. B. Posthill, Jpn. J. Appl. Phys. **30**, L1409 (1991).
4. K. L. Moazed, J. R. Zeidler and M. J. Taylor, J. Appl. Phys. **68**, 2246 (1990).
5. T. P. Humphreys, J. V. LaBrasca, R. J. Nemanich, K.Das and J. B. Posthill, Electron. Lett. **27**, 1515 (1991).
6. V. Venkatesan, D. G.Thompson and K. Das, proceedings of Symp. Mater. Res. Soc. **270**, 419 (1992).

METAL CONTACTS

XIII. Chemical and Electrical Mechanisms in Titanium, Platinum, and Hafnium Contacts to Alpha(6H) Silicon Carbide

A. Introduction

In metal-semiconductor contacts a critical quantity which describes the relationship between the two materials is the Schottky barrier height (SBH), Φ_B. In general it is this property which best indicates the electrical characteristics of the contact. For an ohmic contact, in which the current is both linear and symmetric for positive and negative voltages, one would expect a small or negative SBH. On the other hand, for a good rectifying contact, in which current flows only under forward bias, one would expect a relatively large SBH.

Because the SBH is such an important parameter in terms of defining the ohmic or rectifying characteristics of a particular contact, it is very important to understand how it is determined. In the ideal case the SBH is defined by the Schottky-Mott limit, or (for an n-type semiconductor) the difference between the metal workfunction and the electron affinity of the semiconductor. However, there are many factors which can cause non-ideal relationships, and hence deviations from this rule. J. Pelletier et al. [1] have reported Fermi level pinning in 6H-SiC attributed to intrinsic surface states, suggesting little dependence of barrier height on the workfunction of the metal. In addition, L.J. Brillson [2,3] predicts the pinning rate to be higher for more covalently bonded materials.

Alpha (6H)-SiC is a particular polytype of silicon carbide, a wide bandgap semiconductor, being used in many high-power, -temperature, -frequency, and radiation hard electronic and opto-electronic devices. The future development of SiC device technology depends on, and may in fact be limited by, the ability to form good ohmic and Schottky contacts. In this study a multi-aspect approach is used in order to try to understand what determines the SBH of metal/6H-SiC contacts. Electrical characteristics of Ti, Pt, and Hf contacts before and after annealing will be discussed along with some of the interface phase chemistry and structure.

B. Experimental Procedures

Vicinal single crystal, nitrogen-doped, n-type (10^{16} - 10^{18} cm^{-3}) substrates of 6H-SiC (0001) containing 0.5-0.8 μm thick, nitrogen-doped (10^{16} cm^{-3}) homoepitaxial films were provided by Cree Research, Inc. The Si-terminated (0001) surface, tilted 3°-4° towards $[11\bar{2}0]$ was used for all depositions and analyses.

For processing Ti contacts substrates were cleaned in sequence using a 10 min. dip in an ethanol / hydrofluoric acid / water (10:1:1) solution and a thermal desorption in ultra-high vacuum (UHV) (1 - 5×10^{-10} Torr). All processing steps were the same for Pt and Hf contacts, except 10% HF in deionized water was substituted for the wet chemical clean. A resistive graphite heater was used to heat the substrates at 700°C for 15 min.

A Riber x-ray photoelectron spectroscopy (XPS) system, consisting of a Mac2 semi-dispersive electron energy analyzer and accessible by UHV transfer from the heating station and deposition chamber, was used to monitor surface chemistry and band bending. A Mg anode was used at 1.2 eV resolution for obtaining valence structure and 0.8 eV resolution for core level data.

The metals were deposited onto unheated substrates by electron beam evaporation (base pressure < 2×10^{-10} Torr). For films less than or equal to ~10 nm, a deposition rate of ~1 nm/min was used. For thicker films the rate was increased to 2 - 3 nm/min after deposition of the first 10 nm.

For electrical characterization vertical contact structures consisting of 500 μm and 750 μm diameter circular contacts of 100 nm thickness were created by depositing the metal through a Mo mask in contact with the SiC epitaxial layer, leaving a patterned metal film. Conductive liquid Ag served as the large area back contact. All subsequent annealing was done in UHV. Current-voltage (I-V) measurements were taken with a Rucker & Kolls Model 260 probe station in conjunction with an HP 4145A Semiconductor Parameter Analyzer. Capacitance-voltage (C-V) measurements were taken with a Keithley Model 5956 Package 82 Simultaneous CV System in conjunction with an HP vector PC-308. The contact structures were the same as above. Measurements were taken at a frequency of 1 MHz.

All metal/SiC samples were prepared in cross-section for TEM analysis. High resolution images were obtained with an ISI EM 002B operating at 200 kV. Analytical electron microscopy was performed with a Philips 400 FEG, installed with Gatan 607 parallel electron energy loss spectrometer, operated at 100 kV.

C. Results

Ti Contacts. In this section electrical characteristics, particularly the Schottky barrier height (SBH) measured by I-V, C-V, and XPS techniques, of unannealed and annealed Ti films deposited on 6H-SiC will be presented along with the identification of phases formed in the reaction zone. The room temperature deposition of Ti on (0001) SiC resulted in epitaxial films [4]. Both Ti (a = 2.95 Å, c = 4.68 Å) and 6H-SiC (a = 3.08 Å, c = 15.11 Å) have hexagonal crystal structures, corresponding to a 4% lattice mismatch in the (0001) basal plane.

Current-voltage measurements of as-deposited Ti contacts were found to be rectifying with low ideality factors and with typical leakage currents of 5×10^{-7} A/cm^2 at -10 V [4]. After annealing at 700°C for 20 minutes, the leakage increased; however, after further annealing up to 60 minutes the characteristics in terms of leakage and ideality factors again improved.

The low ideality factors were taken as evidence that thermionic emission theory may be applied for calculating the SBH [5]. For values of applied voltage greater than 3kT/q, the current density can be expressed as

$$J = J_0 \exp\left(\frac{qV}{nkT}\right),$$

where J_o is the extrapolated current at zero voltage, and n is the ideality factor. The SBH can then be determined from the equation

$$\Phi_B = \frac{kT}{q} \ln\left(\frac{A^{**}T^2}{J_0}\right),$$

where A** is the effective Richardson constant. An SBH of 0.85 eV was calculated for unannealed Ti contacts. This barrier was found to increase to 0.95 eV after annealing at 700°C for 60 minutes.

Barrier heights were also determined from capacitance-voltage measurements. By plotting $1/C^2$ vs. V the barrier height can be determined from the equation

$$\Phi_B = V_i + V_n + \frac{kT}{q},$$

where V_i is the voltage intercept ,and V_n is the difference between the conduction band and the Fermi level. Figure 1 shows $1/C^2$ vs. V of an as-deposited Ti/SiC contact biased from 0 to -2 V. Extrapolating the linear region gives an intercept of 0.67 V, indicating a SBH of 0.88 V. Similarly, a SBH of 1.04 V was calculated for annealed contacts.

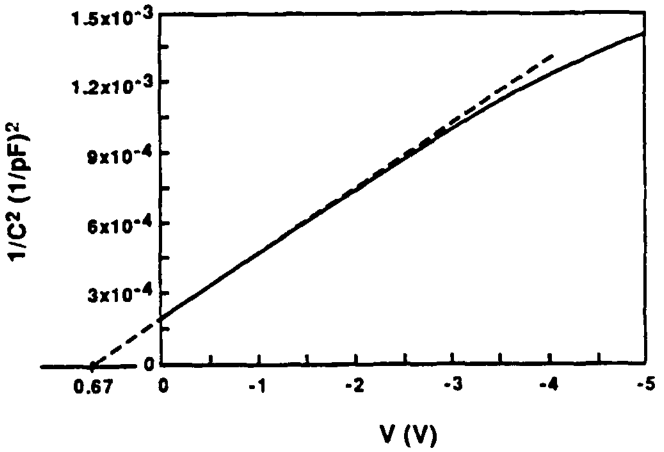

Figure 1. $1/C^2$ vs. V of as-deposited Ti/SiC (contact area = 2.0×10^{-3} cm^2) $\Phi_B \equiv 0.88$ V.

X-ray photoelectron spectroscopy, typically used for chemical analysis of surfaces, was a third technique used for calculating the SBH of Ti on SiC. In this technique photoelectrons are ejected from the near surface (~20 Å) region on which Mg Kα (1253.6 eV) or Al Kα

(1486.6 eV) x-rays are focused. The binding energy is determined from the kinetic energy of the ejected photoelectrons. Prior to depositing any metal atoms the valence levels of the SiC surface were examined by measuring the high kinetic energy electrons (Fig. 2(a)). The top of the valence band was estimated by extrapolating the leading edge of the lowest binding energy peak. With reference to the 3.9 eV Fermi level (determined with a Au standard), the top of the valence band sits at approximately 1.8 eV. Since the SiC epitaxial layer (bandgap = 2.86 eV) is doped n-type (10^{16} cm^{-3}), these results indicate that the bands bend upward at the semiconductor surface (E_C–E_F ≈ 1.1 eV).

Core level peaks were also obtained from the SiC surface and the Ti/SiC interface after depositing Ti in 2 Å to 4 Å increments. The Si 2p, C 1s, and Ti $2p_{3/2}$ and $2p_{1/2}$ doublet peaks at various stages in the series are shown in Figure 2 (b), (c), and (d), respectively. Subtracting the 3.9 eV workfunction of the analyzer, the silicon and carbon peaks prior to deposition of Ti are located at 100.5 and 282.7 eV, respectively, the expected binding energies for Si-to-C bonding [6]. After depositing approx. 4 Å Ti a shoulder on the low binding energy side of the C peak begins to form and is attributed to TiC bonding [7,8]. The fact that no shifts were detected in the Si peak or the portion of the C peak due to C-Si bonding indicates that there is no change in band bending; therefore, the barrier height is estimated to be equal to 1.1 eV.

The Ti/SiC interface was also studied with high resolution transmission electron microscopy (HRTEM) and is reported in more detail elsewhere [9]. After annealing at 700°C for 20 minutes, the reaction zone was found to consist of a very thin layer of cubic TiC_{1-x} in contact with the SiC and a layer of orthorhombic Ti_5Si_3 with TiC_{1-x} particles at the Ti side of the interface. After annealing for 60 minutes, the width of the reaction zone did not increase, but the TiC_{1-x} particles disappeared. The position of layers comprising the interface is SiC / TiC_{1-x} / Ti_5Si_3 / Ti. The lattice parameter of TiC_{1-x} varied by approximately 2% along the SiC interface.

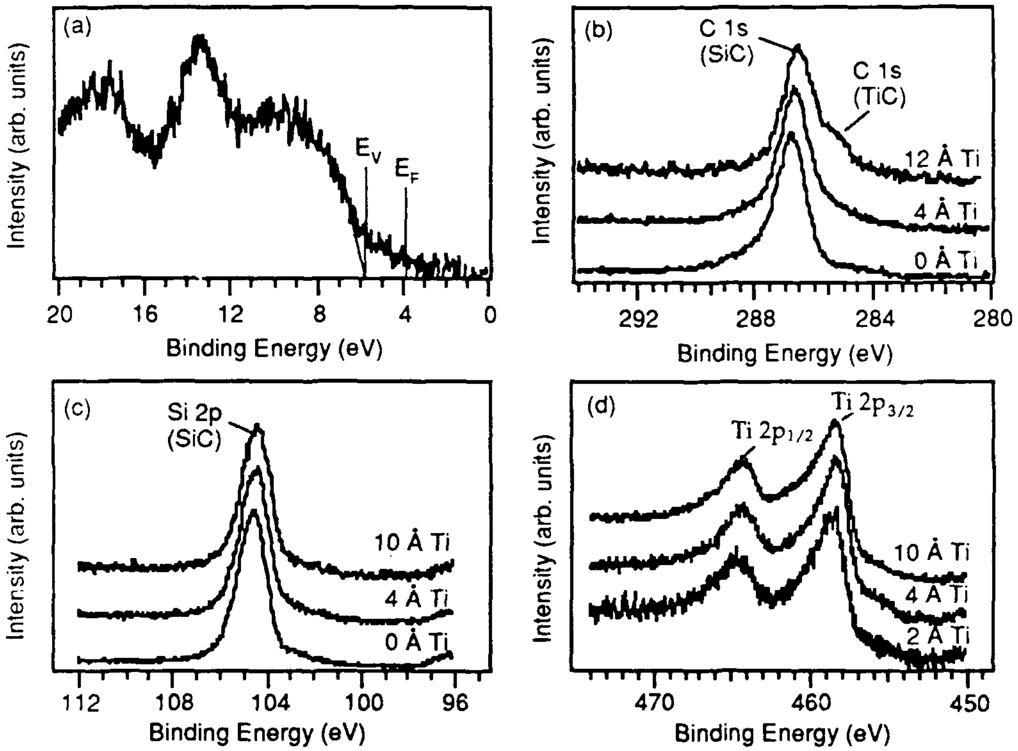

Figure 2. XPS spectra of (a) valence levels of chemically-cleaned SiC surface and (b) C 1s, (c) Si 2p, and (d) Ti 2p peaks after depositing various thin layers of Ti.

Pt Contacts. Platinum contacts deposited at room temperature formed Schottky contacts to SiC with low leakage currents and low ideality factors (Fig 3). The leakage at -10 V was typically 5 x 10^{-8} A/cm^2, and the ideality factors were consistently between 1.02 and 1.06. Using the procedure outlined above, a barrier height of 1.06 eV was calculated from I-V measurements.

These contacts were annealed from 450°C to 750°C in 100 °C increments for 20 minutes at each temperature. Figure 4 shows an interesting trend through this annealing series, throughout which the ideality factors and leakage currents remained low; the SBH increased with anneal temperature to 1.26 eV. These results are similar to those reported by Papanicolaou et al. [10] in which the SBH of Pt on β-SiC increased from 0.95 eV for as-deposited contacts to 1.35 eV after annealing at 800°C.

Initial investigation of the Pt/SiC interface with HRTEM has been performed. The unannealed films are polycrystalline with a grain size of 10 nm. Observation of the 650°C annealed interface revealed an increase of the average grain size to 80 nm. After annealing at 750°C, the reaction zone consisted of a 12 nm amorphous region with some crystalline regions apparently nucleating at ledges in the SiC surface.

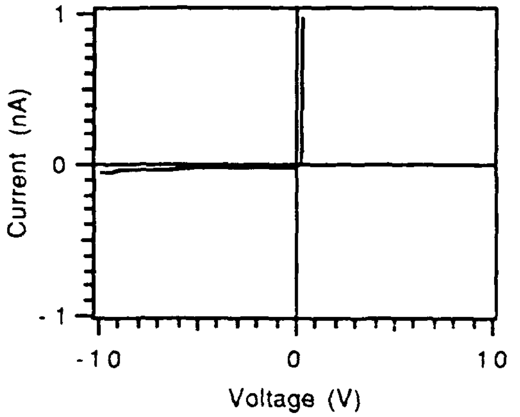

Figure 3. I vs. V of Pt/SiC
(contact area = 2.0 x 10^{-3} A/cm^2).

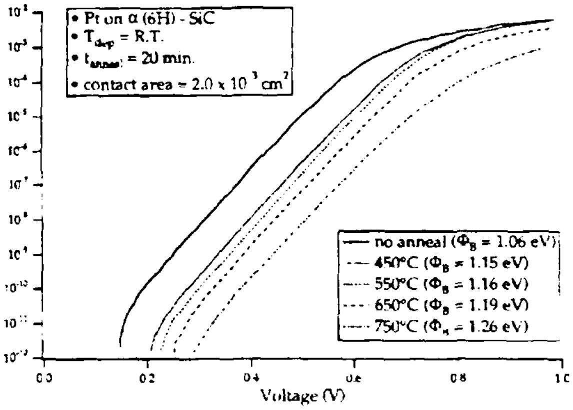

Figure 4. Log I vs. V of Pt/SiC.

Hf Contacts. Current-voltage measurements of as-deposited and annealed hafnium contacts also displayed rectifying characteristics and low ideality factors. The as-deposited contacts produced typical leakage currents of 2.5 x 10^{-7} A/cm^2 at -10 V, while annealing at 700°C for 20 minutes resulted in a reduction of the leakage to 4.0 x 10^{-8} A/cm^2. Upon further annealing, the leakage currents increased.

Concomitant with the observable variation in the reverse characteristics with annealing time, the calculated SBH was found to vary. The 0.97 eV SBH for the unannealed contacts increased to 1.01 eV after the 20 min. anneal and then successively decreased to 0.93 eV and 0.86 eV for the 40 min. and 60 min. anneals, respectively. Qualitatively, the leakage current appears to vary inversely with the height of the barrier, as would be expected.

Initial investigation of these interfaces with HRTEM was performed. Although Hf (a = 3.19 Å, c = 5.05 Å) also has a hexagonal crystal structure with a <4% lattice mismatch with the (0001) basal plane of SiC, epitaxial growth did not occur. Preliminary investigation of Hf/SiC interfaces after annealing at 700°C has not revealed the formation of any new phases.

D. Discussion

The measured and predicted SBH's have been compared for the three metals studied here with n-type SiC (Table 1). The measured values were taken from I-V measurements as reported above, while the predicted values were calculated from the workfunctions of the respective metals. Although the theoretical values vary from 0.52 eV to 2.27 eV, a 1.75 eV range, the measured values vary by less than 0.2 eV.

Table 1. Measured and theoretical Schottky barrier heights for as-deposited Ti, Pt, and Hf on n-type 6H-SiC.

Metal	$\Phi_B^{I\text{-}V}$ (eV)	Φ_B^{th} (eV)
Ti	0.85	0.95
Pt	1.02	2.27
Hf	0.97	0.52

The XPS valence spectrum of the SiC surface (Fig. 2(a)) provides additional insight regarding energy band relationships. The fact that the bands bend upward at the surface without a metal overlayer indicates that surface states are present. It is unknown at this time whether these states are intrinsic or extrinsic (i.e. surface impurities). However, the surface states appear to affect charge transfer between the metals and SiC, and hence largely control the SBH.

There are additional changes in the SBH's resulting from annealing the interfaces. These changes might be expected since the original surface has reacted to form new phases. In the Ti/SiC system the phase in contact with SiC after annealing at 700°C is titanium carbide. In fact, Ti-C bonding was detected in the C 1s peak (Fig. 2(b)) after deposition of approximately 4 Å of Ti at room temperature.

The formation of TiC_{1-x} and Ti_5Si_3 in the Ti/SiC system at higher temperatures (1200 - 1500°C) has been reported by others [11-13]. At 700°C the results seem to indicate that the kinetics of forming TiC are faster than that of forming Ti_5Si_3, resulting in the TiC phase being adjacent to the SiC.

Because the TiC phase forms a continuous layer adjacent to the SiC, that phase should determine the contact characteristics after 700°C annealing. However, the low workfunction (~2.6 eV [14]) determined experimentally for single crystal TiC would predict ohmic behavior. The non-ohmic behavior may be due to one or more of the following reasons: (1) unknown increase in the workfunction with the non-stoichiometry, (2) metal-induced gap states, and (3) incomplete removal of surface states.

E. Conclusions

A combination of techniques was used to study the electrical, chemical, and/or structural properties of Ti, Pt, and Hf contacts to n-type 6H-SiC. All of these contacts were rectifying with ideality factors less than 1.1. Although the workfunctions would predict a >1.5 eV range in SBH for the as-deposited contacts, I-V and C-V measurements indicate a <0.2 eV variation between metals. In addition, an XPS valence spectrum of the SiC surface indicates that the Fermi level lies approx. 1.8 eV above the top of the valence band, relatively near the middle of the bandgap. Pinning of the Fermi level in the bandgap would explain the small dependence of the SBH on metal workfunction.

Although the SBH for Pt contacts was found to increase with annealing temperature, there was not much change observed in Ti contacts after annealing at 700°C. The reaction zone was found to consist of Ti_5Si_3 and a TiC_{1-x} layer adjacent to the SiC. Readers are referred to J. S. Bow et al. [9] for more discussion on this subject.

F. Future Research Plans/Goals

Efforts will be continued to gain a cohesive understanding of what determines the SBH's of Ti, Pt, and Hf contacts to 6H-SiC. Because the results of the experiments performed on these metal/SiC systems imply that the Fermi level is pinned at the SiC surface, comparison to other cleaning techniques is planned in the immediate future. Similar XPS experiments will be performed to determine the location of the Fermi level. If the bands at the surface are found to be flat (i.e. Fermi level is unpinned), SBH's will be remeasured and compared previous values.

Two other metal contacts, Co and Sr, chosen for this study will also be analyzed in terms of electrical, chemical, and structural characteristics. Because of its low workfunction, it is proposed that Sr will form an ohmic contact if the Fermi level is unpinned. In addition, with comparison to Ni, Co also may form an ohmic contact after high temperature annealing. These metal / SiC systems will then be compared in terms of their ohmic or rectifying characteristics.

G. References

1. J. Pelletier, D. Gervais, and C. Pomot, J. Appl. **55** (1984) 994.
2. L. J. Brillson, Phys. Rev. B, **18** (1978) 2431.
3. L. J. Brillson, Surf. Sci. Rep., **2** (1982) 123.
4. L. M. Spellman, R.C. Glass, R.F. Davis, T.P. Humphreys, H. Jeon, R.J. Nemanich, S. Chevacharoenkul, and N. R. Parikh, Mat. Res. Soc. Symp. Proc., **221** (1991) 99-104.
5. See for example, E. H. Rhoderick and R. H. Williams, *Metal-Semiconductor Contacts*, 2nd Ed. (Clarendon Press, Oxford, 1988); S. M. Sze, *Physics of Semiconductor Devices*, 2nd Ed.(John Wiley & Sons, New York, 1981); H. K. Henisch, *Semiconductor Contacts* (Clarendon Press, Oxford, 1984).
6. K. L. Smith and K. M. Black, J. Vac. Sci. Technol. A, **2** (1984) 744.
7. L. Ramquist, K. Hamrin, G. Johansson, A. Fahlman, and C. Nordling, J. Phys. Chem. Solids, **30** (1965) 1835.
8. H. Ihara, Y. Kumashiro, A. Itoh, and K. Maeda, Jap. J. Appl. Phys., **12** (1973) 1462.

9. J. S. Bow, M. J. Kim, R. W. Carpenter, L. M. Porter, and R. F. Davis, Mat. Res. Soc. Symp. Proc. (1992), to be published.
10. N. A. Papanicolaou, A. Christou, and M. L. Gipe, J. Appl. Phys. **65** (1989) 3526.
11. M. Backhaus-Ricoult, Acta-Scripta Met. Proc., **4** (1989) 79.
12. S. Sambasivan and W.T. Petusky, J. Mater. Res., **7** (1992) 1473.
13. C. E. Bruckl, AFML Tech. Rep., AFML-TR-65-2, Pt. II, Vol. VII, Air Force Materials Laboratory, Wright Patterson Air Force Base, OH (1966).
14. K. Senzaki and Y. Kumashiro, Bull. Electrotech. Lab. Jpn. **41** (1977) 593.

ATOMIC LAYER ETCHING

XIV. Atomic Layer Etching

A. Introduction

Atomic layer etching promises atomic scale control in removing surface atoms one monolayer at a time. The precise controllability of surface thickness and uniformity by a digital self limiting etching reaction will provide a technique for the fabrication of new device structures [1]. Also, the prospect of contamination and defect free materials obtained by this process is important in the realization of large scale optical device fabrication [2].

Monolayer etching results from a cycle alternating a fluence of etchant that adsorbs onto the surface, followed by an energetic beam of radiation or ions which removes the surface layer [3]. Recently [1], a Cl_2/Ar^+ etchant/energetic beam experiment on GaAs exhibited self limited etching at one molecular layer. One monolayer adsorption of Cl^- on the surface is an essential condition for the self limited etch.

B. Experiment

The etching of GaAs by HCl/electron beam etch cycle has produced favorable results [4]. Also, ArF laser assisted Cl_2 etching of GaAs has resulted in controlled anisotropic etching along different crystallographic directions [5]. In our experiment we will investigate the digital etching behavior of GaAs by using an ArF excimer laser with HCl etchant.

The initial experimental setup will use a recently built ultra high vacuum (UHV) system designed for ArF excimer assisted ablation deposition, equipped with RHEED and mass spectrometer. The etchant fluence into the chamber will be monitored by the pressure inside the chamber and regulated accordingly. The excimer laser will be directed at the GaAs surface to irradiate and break the surface bonds Excess etchant and etchant products will be removed from the chamber by a turbo-molecular pump.

C. Results

The design of the HCl gas manifold and delivery system is being developed in order to achieve the monolayer etchant requirement for self limited etching. The operation of the UHV ablation system will not be hindered by the etching process; however, slight internal modifications will be required to control the excimer beam strength.

D. Conclusions

Attention will be given to the design of the gas delivery system with respect to the literature observations necessary for self limited etching of GaAs.

E. Future Research Plans

Immediate plans include designing the gas delivery system and modifying the UHV ablation system to etch GaAs. If successful, we will apply the etching technique to other high bandgap materials such as GaP.

F. References

1. Y. Aoyagi, K. Shinmura, K. Kawasaki, T.Tanaka, K. Gamo, S. Namba, I. Nakamoto, Appl. Phys. Lett., 60, 968 (1992).
2. L. A. DeLouise, J. Appl. Phys., 70 (3), 1718 (1991).
3. T. Meguro, M. Hamagaki, S. Modaressi, T. Hara, Y. Aoyagi, M. Ishii, Y. Yamamoto, Appl. Phys. Lett., 56 (16), 1552 (1990).
4. K. Akita, Y. Sugimoto, H. Kawanishi, Semicond. Sci. Technol. 6, 934 (1991).
5. P. Tejedor, F. Briones, Mat. Res. Soc. Symp. Proc. Vol. 201. (1991).

XV. Distribution List

Mr. Max Yoder Office of Naval Research Electronics Division, Code: 1114SS 800 N. Quincy Street Arlington, VA 22217-5000	3
Administrative Contracting Officer Office Of Naval Research Resident Representative The Ohio State University Research Center 1960 Kenny Road Columbus, OH 43210-1063	1
Director, Naval Research Laboratory ATTN: Code 2627 Washington, DC 20375	1
Defense Technical Information Center Bldg. 5, Cameron Station Alexandria, VA 22314	2